

DISS. ETH NO. 21378

**GAS BEARING WITH ACTIVE
MAGNETIC DAMPING FOR
ULTRA-HIGH-SPEED ELECTRICAL
DRIVE SYSTEMS**

A dissertation submitted to
ETH ZURICH

for the degree of
Doctor of Sciences

presented by
ANDREAS E. LOOSER
Dipl. El.-Ing. ETH Zürich
born 29. March 1981
citizen of Ebnat-Kappel SG, Switzerland

accepted on the recommendation of
Prof. Dr. Johann W. Kolar, examiner
Prof. ir. Robert H. Munnig Schmidt, co-examiner

2014

Acknowledgements

I would like to thank the people who made this work possible and supported me during my Ph.D. studies at Power Electronic Systems Laboratory (PES).

First, I want to thank Prof. Dr. Johann W. Kolar for giving me the opportunity to work in his motivated and inspiring team. I very much appreciated his inspiring and creativity stimulating support, his confidence in and positive attitude for my research work. The thrust and freedom he gave me to follow own research ideas meant very much to me.

I'm also grateful to Prof. ir. Robert H. Munnig Schmidt for his interest in the present work and for accepting the invitation to be a co-examiner of this thesis.

I wish to thank the entire PES staff including my fellow Ph.D. students, post-doctoral researchers, secretaries, It support team, electronics laboratory, administrators and the staff of the mechanical workshops of D-ITET and D-PHYS for their support and a superb research atmosphere. Especially I would like to thank my office mates Thomas Baumgartner, Arda Tüysüz and Daniel Krähenbühl for the inspiring technical discussions and sharing the ups and downs of the everyday research life.

I also would like to thank Christof Zwyssig from the PES spin-off company Celeroton for his initial support and for motivating the present research project. I was glad to know that project results would finally go into industrial implementation and would not be discarded in an archive drawer.

Last but not least, I would like to thank my girlfriend, my family and my friends for their great support and for helping to maintain a sound balance of recreation and work.

Abstract

Ultra-high-speed electrical drive systems are expected in industrial applications such as turbo-compressors for heat pumps, fuel cells, generators for portable gas or air turbines and cryogenic systems, with rotational speeds ranging from 200'000 revolutions per minute (rpm) to 1 Million rpm at power ratings of a few tens of watts to a few kilowatts. At high rotational speeds, these applications can be realized with high power density, compact size and low weight. While efficient electric machine designs have been developed for highest rotational speeds, their use in industrial applications is currently limited by lacking high speed bearing technologies permitting high reliability and long lifetime.

Promising bearing technologies for high rotational speeds are contactless bearing concepts such as active magnetic bearings or gas bearings. While magnetic bearings usually are major electromechanical systems with substantial complexity, gas bearings allow compact realizations with high load capacity and stiffness; however, stringent manufacturing tolerances and poor dynamic stability has been limiting their use at high rotational speeds.

A hybrid bearing approach is therefore followed in the present work employing a self-acting gas bearing as the main load carrying element and a small sized active magnetic damper for stabilization at high rotational speeds; the hybrid gas-magnetic concept aims to combine the advantages of the two individual bearing technologies while eliminating their drawbacks.

Focusing on high speed operation, the basic properties of gas bearings are reviewed and their limitations and critical design aspects involved with ultra-high-speed operation are identified. For stabilization of the gas bearing at high rotational speeds, existing and novel magnetic damper concepts are evaluated. A new eddy current based self-sensing

active magnetic damper concept is proposed, allowing for a highly compact integration into a permanent magnet machine with minimal additional design constraints. Novel circuit topologies are developed to facilitate the eddy current based displacement measurement by means of a high frequency signal injection self-sensing technique.

A prototype machine employing the hybrid gas-magnetic bearing concept is realized and stabilization of an entirely unstable gas bearing design is demonstrated at 210 krpm. The experimental results verify the feasibility of the hybrid bearing approach and demonstrate the capability of the developed self-sensing active magnetic damper concept to facilitate operation of gas bearings at elevated rotational speeds.

Kurzfassung

Ultrahochdrehende elektrische Antriebssysteme werden in zukünftigen industriellen Anwendungen wie Turbo-Kompressoren für Wärmepumpen, Brennstoffzellen, portable Generatoren von Luft- oder Gasturbinen und kryotechnischen Systemen erwartet, mit Drehzahlen von 200'000 Umdrehungen pro Minute (U/min) bis 1 Million U/min bei Leistungen von einigen zehn Watt bis zu einigen Kilowatt. Dank der hohen Drehzahlen können diese Anwendungen mit hoher Leistungsdichte, kompakter Baugrösse und geringem Gewicht realisiert werden. Obwohl bereits Elektromotoren mit hoher Effizienz bei höchsten Drehzahlen vorgestellt und gebaut worden sind, ist ihr Einsatz in industriellen Anwendungen stark limitiert, vorwiegend bedingt durch die beschränkte Lebensdauer von existierenden Lagertechnologien bei diesen Drehzahlen.

Potentiell geeignete Lagertechnologien für hohe Drehzahlen sind berührungslose Lagerkonzepte wie Magnetlager oder Luftlager. Die Installation von Magnetlagern resultiert meist in einem System mit erhöhtem Bauvolumen und erweiterter Komplexität, wohingegen Luftlager sehr kompakt mit hoher Tragkraft und Steifigkeit realisiert werden können. Der Einsatz von Luftlagern bei hohen Drehzahlen ist jedoch stark eingeschränkt, hauptsächlich wegen der schlechten dynamischen Stabilität und der deshalb geforderten engen Fertigungstoleranzen. In der vorliegenden Arbeit wird deshalb ein hybrides Lagerkonzept verfolgt. Dabei wird ein dynamisches Luftlager als primäres Lagerelement eingesetzt, welches bei hohen Drehzahlen mittels eines aktiven magnetischen Dämpfers mit entsprechend kleiner Baugrösse stabilisiert wird. Das Ziel des hybriden Ansatzes ist die Kombination der Vorteile von beiden Lagertechnologien bei gleichzeitiger Minimierung bzw. Elimination ihrer Nachteile.

Fokussierend auf einen Betrieb bei ultrahohen Drehzahlen, werden die grundlegenden Eigenschaften, Möglichkeiten und Einschränkungen von Luftlagern erläutert und kritische Aspekte bezüglich Auslegung und Fertigung aufgezeigt. Zur Stabilisierung des Luftlagers bei hohen Drehzahlen werden sowohl bekannte wie auch neuartige magnetische Dämpferkonzepte evaluiert. Ein neues, sensorloses Dämpferkonzept gestützt auf eine Wirbelstrom-basierte Distanzmessung wird dargelegt, welches eine hohe Integration in eine hochdrehende Permanentmagnet-Synchronmaschine erlaubt und dabei die zugrundeliegende Maschineauslegung und Konstruktion nur minimal beeinträchtigt. Zu diesem Zweck werden neuartige dedizierte Verschaltungstopologien der Dämpfer-Aktuatorwicklung mit den Leistungsverstärkern untersucht, welche das sensorlose Wirbelstrom-basierte Messprinzip mittels Superposition eines hochfrequenten Testsignals ermöglichen.

Ein Prototypen-Aufbau einer Permanentmagnet-Synchronmaschine unter Anwendung der hybriden Lagerung wird präsentiert, welcher mittels der implementierten aktiv magnetischen Dämpfung den stabilen Betrieb eines stark instabilen Luftlagers bis 210 krpm ermöglicht. Die experimentellen Resultate belegen die Tauglichkeit und Machbarkeit des hybriden Lagerungskonzepts und demonstrieren die Möglichkeit des entwickelten Dämpferkonzepts einen stabilen Betrieb von Luftlagern bei hohen Drehzahlen zu gewährleisten.

Notation

Symbols

b	width
c	journal bearing clearance
c_f	Steinmetz coefficient
$c_j(s)$	journal bearing dynamic stiffness
c_s	static stiffness
$d, d(s)$	damping factor and damper transfer function
e	Euler's number
f	force, load capacity
f_{bend}	rotor bending mode resonant frequency
h	film height
h_0	Rayleigh step bearing step profile
h_1, h_2, h_3	Rayleigh step bearing parameters
i	current or index
i_d, i_q	field oriented damper currents
j	imaginary unit
l	length
m	mass
m_{crit}	critical mass parameter
p	pressure
p_a	ambient pressure
p_r	rotor pole pair number
p_s	stator pole pair number
r_b	bearing bushing outer radius

r_j	journal bearing film radius
s	Laplace variable
t	time
u	voltage
v	velocity
(r, θ^*, z)	rotating cylindrical coordinates in steady whirl
(r, θ, z)	cylindrical coordinates
(x, y, z)	Cartesian coordinates
A	state space description matrix or magnetic vector potential
B	state space description matrix or flux density
C	state space description matrix or capacitor
D	state space description matrix or bearing bore diameter
E	elastic modulus
F_{cu}	copper loss coefficient
F_j	gas bearing dimensionless load capacity
G_{cu}	copper loss coefficient
H	normalized film height or magnetic potential
I	unity matrix
\hat{I}	amplitude of damper current
I_{x0}	rotor moment of inertia in transverse axis
I_{z0}	rotor moment of inertia in principle axis
J	current density
K_B	machine flux density coefficient
K_c	thermal expansion parameter
K_d	controller gain parameter
K_n	notch filter design parameter
L	inductance
M	mutual inductance
M_C	Finite difference parameter matrix
M_j	dimensionless stability parameter
$M_P,$	Finite difference parameter matrix
N	rotational speed or number of turns
$N_{bend}(s)$	rotor bending mode notch filter transfer function

N_{step}	number of steps in Rayleigh-step bearing
$N_{syn}(s)$	synchronous notch filter transfer function
P	normalized pressure or power
R	resistance
R_1	permanent magnet radius
R_2	rotor sleeve outer radius
R_3	damper winding inner radius
R_4	damper winding outer radius/machine winding inner radius
R_5	machine winding outer radius/stator iron inner radius
R_6	stator iron outer radius
R_{spec}	specific gas constant
T	temperature or torque
V	volume
V_{bnd}	Finite difference boundary vector
(X, Y, Z)	normalized Cartesian coordinates
Z	impedance
α	coefficient of thermal expansion
α_{fe}	Steinmetz coefficient
β	complex rotor inclination angle
β_{fe}	Steinmetz coefficient
δP	pressure variation
ϵ	journal or rotor displacement
η	dynamic viscosity
γ	angular rotor position
λ	lubrication area length to width ratio or thermal conductivity
λ_j	journal bearing length to diameter ratio
μ, μ_0	magnetic permeability, in vacuum
ν	Poisson's ratio
ω	perturbation frequency
ω_w	whirl frequency
ϕ	bearing attitude angle
φ	angle of damper current space vector

ρ	density
σ	gas bearing dimensionless squeeze number or stress
τ	normalized time
(θ, ζ)	space coordinates for journal bearing fluid film
$\theta_1, \theta_2, \theta_3$	Rayleigh step bearing parameters
ϵ	journal displacement
ε	normalized journal displacement
ξ	state vector
Δ_θ	finite difference discretization step in θ direction
Δ_ζ	finite difference discretization step in ζ direction
$\Delta_{c\Omega}$	centrifugal growth of journal
Δ_{cT}	thermal growth of bushing
Δ_{cb}	thermal growth of bushing
Δ_{cj}	thermal growth of journal
Λ	dimensionless bearing number
Λ^*	dimensionless bearing number under steady whirl
Ω	rotational speed, angular frequency
Ψ	flux linkage

Subscripts

0	initial or centered
<i>amb</i>	ambient
<i>b</i>	bearing bushing
<i>cg</i>	center of gravity
<i>cl</i>	closed loop
<i>cu</i>	machine winding
<i>d</i>	damper
δ	disturbance
<i>dq</i>	rotor field oriented
<i>fe</i>	stator iron
<i>fr</i>	viscous friction
<i>ind</i>	induced
<i>j</i>	journal, journal bearing
<i>lrtz</i>	from Lorentz force integration
<i>m</i>	measurement auxiliary element
<i>min</i>	minimum
<i>nom</i>	nominal design
<i>p</i>	originating from pressure
<i>pm</i>	permanent magnet
<i>r</i>	radial direction or rotor
<i>ref</i>	reference
<i>rem</i>	remanent flux
<i>res</i>	resultant
<i>sh</i>	originating from viscous shear stress
<i>shunt</i>	shunt
θ	tangential direction
<i>x</i>	x direction
<i>y</i>	y direction

Abbreviations

AMB	active magnetic bearing
AMD	active magnetic damper
ADC	analog-to-digital converter
DSP	digital signal processor
EDM	electro discharge machining
FDM	finite difference method
FEM	finite element method
FPC	flexible printed circuit
HG	herringbone grooved
LDI	laser direct imaging
LTI	linear time invariant
PSD	power spectral density
PCB	printed circuit board
SPI	serial peripheral interface
RMS	root mean square
rpm	revolutions per minute
VCCS	voltage controlled current source

Contents

Acknowledgements	iii
Abstract	v
Kurzfassung	vii
Notation	ix
1 Introduction	1
1.1 Motivation and Applications	1
1.1.1 Turbo-compressor for Automotive Fuel Cells . . .	3
1.1.2 Turbo-compressors for Heat Pump Applications .	3
1.2 State-of-the-Art	4
1.2.1 High Speed Electrical Drive Systems	4
1.2.2 High Speed Magnetic Bearings	5
1.2.3 High Speed Gas Bearings	6
1.3 Challenges	7
1.4 Outline of the Thesis	8
1.5 Scientific Contributions	9
1.6 List of Publications	10
2 High Speed Bearing Technology	13
2.1 Ball Bearings	13
2.2 Magnetic Bearings	15
2.3 Gas Bearings	16
2.4 Comparison of Bearing Types	19
2.5 Gas-Magnetic Hybrid Bearing Concept	20

3	Modeling and Design of Gas Bearings	25
3.1	Reynolds Equation	25
3.2	Scaling of Gas Bearings	29
3.3	Gas Bearing Reaction Forces	32
3.4	Friction Losses	34
3.5	Centrifugal and Thermal Expansion	34
3.6	Numerical Modeling of Gas Bearings	39
3.6.1	Review on Numerical Modeling of Gas Bearings	40
3.6.2	Numerical Solution of the Steady State Reynolds Equation	42
3.6.3	Bearing Transient Behavior	45
3.7	Dynamic Stability	51
3.7.1	Attitude Angle and Damping	51
3.7.2	Critical Mass	53
3.7.3	Means for Stability Improvement	54
3.8	Rayleigh Step Bearing Design	56
4	Active Magnetic Damper	61
4.1	Electro-Magnetic Modeling	61
4.1.1	Slotless Homopolar Damper Winding	62
4.1.2	Slotless Heteropolar Damper Winding	64
4.2	Evaluation of Sensing and Damping Concepts	73
4.2.1	Back-EMF based Homopolar Damper	75
4.2.2	Back-EMF based Heteropolar Damper	78
4.2.3	Eddy current based self-sensing concept	80
4.2.4	Comparison of the Concepts	86
4.3	Heteropolar Eddy Current based Self-Sensing AMD	88
4.3.1	Functional Overview	89
4.3.2	Winding Concept	90
4.3.3	Circuit Topology	91
4.3.4	Power Amplifier	95
4.3.5	Self-Sensing Angular Position Measurement	97
4.3.6	Concluding Remarks	98
5	Control	101
5.1	Rotor Dynamic Modeling	101
5.1.1	Rigid Rotor Model	101
5.1.2	Rotor Gas-Bearing System	105
5.2	D-Controller	108
5.3	Synchronous Whirling	111

5.4	Rotor Bending Mode	112
6	Hardware Prototype and Experimental Results	115
6.1	System Integration	115
6.1.1	Electrical Machine	116
6.1.2	Magnetic Damper Winding	121
6.2	Gas Bearings	123
6.2.1	Journal Bearings	123
6.2.2	Thrust Bearing	123
6.3	Damper Electronics	125
6.4	Experimental Results	125
6.4.1	Displacement measurement	125
6.4.2	Stabilization of the Gas Bearings	128
6.4.3	Deceleration Test	131
7	Conclusion	135
7.1	Summary	135
7.2	Outlook	137
	Bibliography	139
	Curriculum Vitæ	149

Chapter 1

Introduction

1.1 Motivation and Applications

An increasing number of ultra-high-speed electrical drive systems is expected in industrial applications of turbo-compressors in heat pumps, fuel cells, generators for portable gas or air turbines and cryogenic systems with rotational speed ranging from 200'000 rotations per minute (rpm) to 1 Million rpm at power ratings of a few tens of watts to a few kilowatts. Further applications of ultra-high-speed electrical machines include micro machining spindles, medical and dental drills, optical devices and flywheels. An overview of these ultra-high-speed applications is given in [1] and [2].

A number of challenges involved with electrical machine design for ultra-high speeds have been addressed in [3, 4, 1] which are of thermal, elastic, and rotor-dynamic nature. Thus, in a multi-physical machine design approach, optimized machine designs have been presented with low losses at high speeds as well as a robust rotor construction in order to cope with rotor-dynamics and the high centrifugal stresses under rotation.

Yet, the use of such ultra-high-speed drive systems in industrial applications is limited mainly due to the absence of low cost and reliable bearings with long lifetime at high rotational speeds. Bearing technologies employed at elevated speeds are ball bearings, gas bearings and magnetic bearings. However, each technology brings besides its advantages also some major drawbacks.

Commercially available ball bearings can be used in applications at the lower end of the mentioned speed range, especially where a total life time of some hundreds of hours is sufficient, such as in medical or dental tools. However due to high friction losses and wear at high rotational speeds, ball bearings seem not to meet the lifetime requirement for most of the mentioned miniature scale applications at the top end of the specified rotational speed range.

Top speeds reached with active magnetic bearings (AMBs) are as high as 150 krpm [5] and in a recent achievement 505 krpm have been achieved [6]. Although allowing for high-speed operation without an inherent lifetime limitation due to the contactless operation, magnetic bearings usually increase the systems installation size considerably and enhance the overall system complexity with the need of displacement sensors, actuators, power amplifiers, control and an emergency touch-down bearing system.

Compared to magnetic bearings, gas bearings are compact and provide high load capacity. Rotational speeds above 1 million rpm have been reached with rotating machinery supported by gas bearings. However, the main limiting factors are its stringent production tolerances and the related susceptibility to self-excited whirl instability, especially when rotors with high inertial mass such as used in permanent magnet machines need to be supported.

Thus in this thesis, a hybrid bearing concept is suggested which employs a self-acting gas bearing as the main load carrying element and a small sized self-sensing active magnetic bearing or damper as a stabilizing element. The hybrid bearing concept aims to combine the advantages of both bearing concepts, while minimizing or eliminating the drawbacks of the individual bearing technologies. In particular, it allows for a gas bearing design with more relaxed production tolerances and with the self-sensing active magnetic damper (AMD) approach, the increase of installation size and system complexity is kept at a minimum.

The choice of an appropriate bearing technology for a given application is often not obvious and in some cases several types of bearings may yield a satisfactory performance. Still, application of the hybrid bearing concept is primarily seen in miniature scale turbo-machinery. In turbo-machinery applications, the self-acting gas bearing has well established. When scaling to the miniature scale and proceeding towards higher speeds, fabrication tolerances become stringent and high speed operation is limited due to poor dynamic stability. In combina-

tion with the magnetic damper, i.e. in a hybrid bearing approach, the speed range can be extended and fabrication tolerances can be relaxed. It also presents a mean to reduce the viscous friction losses of the gas bearing by permitting a larger bearing clearance.

1.1.1 Turbo-compressor for Automotive Fuel Cells

In an automotive fuel cell application a compressor has to provide oxygen for the oxidation of H_2 to H_2O . Oxygen is provided from the ambient by means of a compressor which compression power is typically a fixed percentage of approximately 10% to 15% of the fuel cell output power. Optimal pressures are 1.5 bar to 2.5 bar for a proton exchange membrane fuel cell [7]. Key requirements for the compressor systems in an automotive fuel cell are compact size, low weight, high efficiency and a lifetime of more than 5000 hours. A further essential requirement is oil-free operation, in order not to contaminate the process. For this purpose, a turbo-compressor supported by gas bearings is found optimal. A rotational speed of the turbo-compressor is in the range of 100 to 500 krpm is then required.

A design of an electrically driven fuel cell turbo-compressor with a power rating of 580 W at a speed of 250 krpm is given in [8]. While in a prototype status, the compressor however runs on ball bearings, which as indicated require changing due to their limited lifetime. While in a research status, ball bearings represent a convenient solution as being available out-of-the-shelf, they will not meet the lifetime requirement in the final application.

When aiming for smaller fuel cell output powers, the turbo-compressor will downscale to a smaller size to reduce the mass flow and in order to maintain the pressure ratio higher rotational speeds will be needed. There, a hybrid gas-magnet bearing concept will be a promising solution.

1.1.2 Turbo-compressors for Heat Pump Applications

The main driver for employing small scale turbo-machinery in heat pumps is the potential for reaching higher efficiencies than with commonly used volumetric compressors and the potential for making the compressor oil-free [9]. A 1.8 kW turbo-compressor for use in a domes-

tic heat pump with a speed of 210 krpm and an efficiency of 79% has been presented in [10]. The compressor uses self-acting gas bearings for rotor support, which has been found the most promising solution among currently available bearing technologies.

In conventional combustion engine driven vehicles, the waste heat from the combustion engine is used for compartment heating. In more efficient hybrid, fuel cell driven or pure electric vehicles however, the waste heat is not sufficient anymore to heat the compartment. Therefore, heat pumps are also employed in the automotive sector [11, 12]. A commonly used compressor type for automotive air conditioning systems is the scroll compressor which has substantial size and weight does not operate completely oil-free. Oil-free small scale turbo machinery realizable with compact size and low weight will therefore bring a considerable improvement.

When scaling the domestic heat pump for automotive use, lower powers at higher speeds will be required. For such an application, a turbo-compressor system operating at speeds up to 600 krpm is presented in [13]. For rotor support at these elevated speeds and a lifetime requirement of more than 5000 hours, the hybrid gas-magnetic bearing concepts seems a promising option.

1.2 State-of-the-Art

1.2.1 High Speed Electrical Drive Systems

High speed electrical machines with speeds above 200 krpm are reported by a number of research groups. In [4], a slotless permanent magnet machine is reported which operates at 200 krpm at a power level of 2 kW. A machine design with the same specification for a cryogenic cooling application is presented in [14]. Ball bearings are used for the prototype design while a gas bearing is planned for the final application. No further upgrade however is found on the current project status. [15] reports on the design of a 5 kW, 240 krpm permanent magnet machine which was operated up to 180 krpm under no load condition.

In a recent development, commercial high speed electrical drives engineered for customer defined applications are available up to speeds of 1 Mrpm [16]. Electrical drive systems with speeds ranging up to 450 krpm are also available from [17].

The present work is based on the recent achievements of preceding

research and developments in ultra-high-speed drive system at ETH Zurich. A slotless permanent magnet machine design with low losses at high rotational speeds, a robust rotor construction and power electronics to drive the machines up to speeds of up to 1 Mrpm have been detailed in [1]. The work presents machine designs and experimental results with rotational speeds of 500 krpm and 1 Mrpm. [2] is a follow-up project employing the same basic machine design concept in small scale turbo-machinery applications. As one of the main results, an electrically driven miniature two-stage with a rotational speed tested at a speed of 600 krpm is presented. In these machine prototypes, ball bearings were used.

1.2.2 High Speed Magnetic Bearings

A permanent magnet biased reluctance type AMB achieving a rotational speed of 90 krpm in a spindle application is reported in [18]. With a combined radial and axial bearing of the same type, a speed of 120 krpm has been achieved in [19]. A high speed magnetically levitated micro-machining spindle rotating at 150 krpm is reported in [5]. [3] reports on the design challenges of high speed permanent magnet machines in general and also presents a machining spindle implementation supported on AMBs at a maximum speed of 156 krpm. For a textile yarn spinning application, a magnetically levitated rotor spinning at 140 krpm is presented in [20]. Most of these applications are operating at peripheral speeds close to the possible structural limits given by the rotor construction and the used materials. Although the rotational speeds achieved with the mentioned active magnetic bearings are well below 200 krpm, in terms of peripheral speed, they can be counted as high speed application. Higher speeds of up to 300 krpm achieved with magnetic bearings are mentioned in [21], however no closer details are given.

In recent research with a slotless Lorentz type magnetic bearing, a rotational speeds of 115 krpm is reported [22] in a bearing-less drive configuration. Scaling towards smaller dimensions and also employing a slotless and bearing-less drive design, a remarkable surge in rotational speed was accomplished in [6] with a demonstrator system rotating at a speed of 505 krpm.

Magnetic bearing technology has been employed at highest speeds in terms of peripheral speed, though mostly at rotational speeds below

200 krpm. It is therefore noticed, that magnetic bearing technology at speeds above 200 krpm is a very new field of research which can be expected to involve new challenges.

1.2.3 High Speed Gas Bearings

Several research groups are investigating self-acting miniature gas bearings for ultra-high rotational speeds. [23] reports on the testing of a foil bearing operated at speeds up to 700 krpm, however driven by a relatively lightweight air turbine. Foil bearings supporting the rotor of a permanent magnet machine at a speed of 350 krpm are reported in [24]; the rated power of the machine is approximately 100 W while operation is demonstrated under idle condition without the load of a typical application.

High speed operation of a 100 W mesoscale gas turbine for portable power application has been accomplished with 4 mm diameter hydro-inertia gas bearings at 890 krpm [25]. While power consumption of the hydro-inertia bearings are a multiple of the gas turbine's output power due to the immense amount air flow provided by pressurized air supply [26], attempts with more efficient self-acting gas bearing types such as herringbone grooved journal bearings which require a minimum film height of 3 μm to 4 μm could not meet the speed goal of 870 krpm. Still, within the same research group, a 8 mm diameter foil bearing operating at a speed of 642 krpm is reported. Referencing on the same project, [27] reports on the design and testing of a herringbone grooved journal bearing supporting a light weight titanium test rotor reaching a speed of 804 krpm.

A wave shaped self-acting gas bearing design achieving a rotational speed of 1203 krpm is presented in [28]. A flexible support of the gas bearings by means of O-rings is used in order to increase the damping capability of the bearing system. For the bearing testing, a light weight turbine driven by pressurized helium is used. Applying the principle of flexible bearing support with increased damping capability to a permanent magnet machine with a rated power of 200 W and a rated speed of 600 krpm, a maximum speed of 410 krpm is achieved [29]. The minimum film height of the employed wave shaped gas bearing is specified as 4 μm . In order to reach the target speed of 600 krpm, a further improvement of the already highly precise production of the bearing parts must be expected.

Most of the above mentioned record-speed bearing tests have been conducted with light weight rotors driven by air turbines in idle condition. In a given application, the gas bearing needs to support a rotor of an electrical machine capable of providing a required shaft power. The rotor of such a system will be heavier than the air-turbines used for record speed bearing tests and therefore instability can be expected to occur already at lower speeds, which the above examples with permanent magnet rotors show.

Although externally pressurized gas bearings are out of focus of the present thesis because of their need for a pressurized air supply, which would substantially increase the total weight and size of a drive system, achievements with this type of bearing are worth mentioning. [30] presents results of a turbine driven micro spinner supported by hydro-inertia gas bearings at a rotational speed of 1.2 Mrpm.

A gas bearing supported ultra-centrifuge operated by a helium turbine at a speed of 1.3 Mrpm is reported in [31]. This result achieved in the year 1937 represents the highest speed achieved in terms of peripheral speed by means of gas bearing support.

Details on a silicon based air turbine supported by externally pressurized gas bearings rotating at 1.7 Mrpm are presented in [32]. Resulting from the constraints imposed by the silicon manufacturing technology, a very small ratio of the journal bearing length to diameter is obtained.

Externally pressurized bearings have established in micro-machining spindles, especially in printed circuit board drilling where with smaller hole sizes, high speeds are required in order to abide cutting speeds. Air bearing supported drilling spindles rotating up to 370 krpm are commercially available e.g. by [33].

1.3 Challenges

The main challenges involved with the hybrid gas-magnetic bearing conceptual design and its implementation are:

- ▶ The selection, modeling and design of a gas bearing for operation at high rotational speeds.
- ▶ The selection and modeling of a magnetic damper concept and its integration into the machines active region in order to minimize an additional space requirement.

- ▶ The identification of a displacement measurement principle suitable for a self-sensing method and providing sufficient resolution and bandwidth for feedback control in order to stabilize the rotor within the gas bearing's clearance, which is in the order of a few micrometers.
- ▶ The conception of a circuit topology enabling the reuse of the magnetic damper actuator as a displacement sensor search coil in a self-sensing method and providing clean separation of actuator current and displacement measurement signals.
- ▶ The conception of a self-sensing angular rotor position measurement, which is required for field oriented feedback control.

1.4 Outline of the Thesis

The goal of this thesis is the concept evaluation, design and experimental testing of a hybrid gas-magnetic bearing system for ultra-high-speed electrical drive systems. The hybrid bearing concept employs a gas bearing for the main load carrying element which is stabilized by a self-sensing AMD to enable stable operation at high rotational speeds. As a new challenge, the combination of the two technologies requires a high sensitivity rotor displacement measurement resolving micron amplitude motion within the gas bearing's clearance for active stabilization. As established self-sensing techniques used in state-of-the-art AMB system are not applicable in the proposed AMD design, different strategies are evaluated and a new eddy current based displacement self-sensing method is developed.

After this introductory chapter, Chapter 2 gives an overview of the chances and limitations of current high speed bearing technologies: ball bearings, magnetic bearings and gas bearings. The hybrid gas-magnetic bearing is introduced and its chances and new challenges are discussed.

In Chapter 3, the basic properties of gas bearings are reviewed including scaling by means of dimensionless numbers, bearing reaction forces and friction losses. Furthermore, their limitations and critical design aspects impacting dynamically stable operation at ultra-high-speeds are identified. A finite difference numerical scheme in combination with linearization of the governing Reynolds equation is detailed for modeling the transient behavior of gas bearings. Finally, design results for a Rayleigh step journal bearing are presented.

Chapter 4 evaluates the slotless AMD actuator construction integrated into an ultra-high speed permanent magnet machine and discusses besides the proposed eddy current based self-sensing AMD also potential back-EMF based self-sensing AMD concepts. Auxiliary circuit topologies are derived, enabling the eddy current displacement self-sensing method using a high frequency signal injection technique. Furthermore, also a self-sensing angular rotor position measurement is presented which is needed for field oriented control.

Stability of a rotor supported by the hybrid bearing system discussed in Chapter 5 based on a rigid rotor model and stabilization by means of a D-controller is analyzed. Furthermore, the need for notch filtering for the suppression of a synchronous controller response as well as a response at the rotor's natural frequency is discussed.

Chapter 6 describes the implementation of a prototype permanent magnet machine employing the hybrid gas-magnetic bearing system. Measurements are presented to verify the performance of the eddy current based displacement self-sensing technique. Further experimental results are given which demonstrate the capability of the hybrid approach to enable operation of gas bearings at elevated rotational speeds.

1.5 Scientific Contributions

The following list summarizes the main scientific contributions related to and originating from the present thesis:

- ▶ [I] studies analytically and experimentally the torque and force contributions resulting from skewed air-gap type machine windings, which may disturb the bearing system. In [III] the analysis is enhanced by rhombic windings. The analysis represents a basis for the choice and design of a winding type and its impact on a given bearing system.
- ▶ The slotless Lorentz type AMB actuator is identified as the preferred choice for ultra-high speed applications [II]. An analytical derivation of the magnetic forces obtained with a skewed type AMB winding are given in [I].
- ▶ in [IV] the concept of the hybrid gas-magnetic bearing approach employing gas bearing as the main load carrying element and an

eddy current based, self-sensing AMD for stabilization of the gas bearing at high rotational speeds is suggested and elaborated.

- ▶ Further, an adapted winding topology for the magnetic damper actuator is suggested in [IV] combined with a dedicated auxiliary circuit which facilitates the eddy current based displacement self-sensing method. In the present thesis, the circuit is further improved enabling a high resolution displacement measurement in the sub micrometer range with high bandwidth.
- ▶ In present work, a prototype machine employing the hybrid bearing system and experimental results thereof are presented which prove the feasibility of the proposed hybrid bearing concept.

1.6 List of Publications

Publications originating from this Ph.D. project are:

- [I] A. Looser, T. Baumgartner, C. Zwyssig, and J. Kolar, “Analysis and measurement of 3D torque and forces for permanent magnet motors with slotless windings,” in *Proceedings of the IEEE Energy Conversion Congress and Exposition (ECCE 2010)*, Sept. 2010.
- [II] T. Baumgartner, A. Looser, C. Zwyssig, and J. Kolar, “Novel high-speed, Lorentz-type, slotless self-bearing motor,” in *Proceedings of the IEEE Energy Conversion Congress and Exposition (ECCE 2010)*, Sept. 2010.
- [III] A. Looser, T. Baumgartner, J. Kolar, and C. Zwyssig, “Analysis and measurement of three-dimensional torque and forces for slotless permanent-magnet motors,” *IEEE Transactions on Industry Applications*, July/Aug. 2012.
- [IV] A. Looser and J. Kolar, “A hybrid bearing concept for high-speed applications employing aerodynamic gas-bearings and a self-sensing active magnetic damper,” in *Proceedings of the 37th Annual Conference on IEEE Industrial Electronics Society (IECON 2011)*, Nov. 2011.

Further publications which are contributed during the Ph.D. research period at Power Electronics Systems Laboratory (PES), ETH

Zurich in electrical machine related topics but not directly related to the Ph.D. project are:

- ▶ D. Bortis, L. Fässler, A. Looser and J. W. Kolar, “Analysis of rotary transformer concepts for high-speed applications,” in *Proceedings of the 28th Applied Power Electronics Conference and Exposition (APEC 2013)*, March 2013.
- ▶ A. Tüysüz, D. Koller, A. Looser and J. W. Kolar “Design of a test bench for a lateral stator electrical machine,” in *Proceedings of the 37th Annual Conference of the IEEE Industrial Electronics Society (IECON 2011)*, Nov. 2011.
- ▶ B. Wrzecionko, A. Looser, J. W. Kolar and M. Casey, “High-temperature (250 °C / 500 °F) 19 000 rpm BLDC fan for forced air-cooling of advanced automotive power electronics,” in *Proceedings of the 37th Annual Conference of the IEEE Industrial Electronics Society (IECON 2011)*, Nov. 2011.
- ▶ J. W. Kolar, T. Friedli, F. Krismer, A. Looser, M. Schweizer, P. Steimer and J. Bevirt, “Conceptualization and multi-objective optimization of the electric system of an airborne wind turbine,” in *Proceeding of the 20th IEEE International Symposium on Industrial Electronics (ISIE 2011)*, June 2011.
- ▶ A. Tüysüz, A. Looser, C. Zwyssig and J. W. Kolar, “Novel miniature motors with lateral stator for a wide torque and speed range,” in *Proceedings of the 36th Annual Conference of the IEEE Industrial Electronics Society (IECON 2010)*, Nov. 2010 .
- ▶ A. Looser, L. Linares, C. Zwyssig and J. W. Kolar, “Novel power supply topology for large working gap dry EDM,” in *Proceedings of the IEEE/IEEJ International Power Electronics Conference (ECCE Asia 2010)*, June 2010.
- ▶ J. Luomi, C. Zwyssig, A. Looser, J. W. Kolar, Efficiency optimization of a 100-W 500 000-r/min permanent-magnet machine including air-friction losses, in *IEEE Transactions on Industry Applications*, July/Aug. 2009

Chapter 2

High Speed Bearing Technology

For the targeted applications presented in Section 1.1, bearings supporting the rotor of a permanent magnet machine with a power rating of some tens of watts to a few kilowatts at speeds ranging from a few hundred thousand rpm to one million rpm with a lifetime of up to several years will be required. Friction losses should be low for a high overall system efficiency. For use in industrial applications, costs should be low. Thus, the ideal bearing requirements are summarized as long lifetime at high speeds, low friction and low cost.

Basic assistance to the selection of mechanical bearings for a given application is provided in [34]. Possible bearing candidates for high speed use have been identified in [3] and [1] as ball bearings, gas bearings and magnetic bearings. A review of the basic properties of these bearing types is given in the following. As each of the discussed bearing types has its advantages and drawbacks, and neither of individual bearing types can comply with the ideal conception of a high speed bearing, a hybrid bearing concept is suggested in order to cope with the challenges imposed by operation at high operational speeds.

2.1 Ball Bearings

The main advantages of ball bearings is their commercial availability for a wide range of different specifications, compact size, high load ca-

capacity and stiffness. Ultra high speed operation however is problematic because of high velocities occurring at the contacting surfaces and the involved wear and high friction losses imposing a limit on the bearing's lifetime.

Limiting speeds of ball bearings are generally referred in terms of the DN number, which is defined as the bearing bore D in millimeters times the rotational speed N in rpm. Material stresses are proportional to $(DN)^2$ while friction per surface area is proportional to the surface speed and hence proportional to DN . The definition therefore indicates the limitations concerning material limitations and friction, i.e. fatigue and thermal limitations. Typical values range from $DN = 500'000$ to $DN = 1.6$ million. Under ideal conditions, numbers of $DN = 3.5$ million were reached [35]. As an example a lifetime of 60'000 hours is reported for a ball bearing of 150 mm diameter running at $DN = 3$ Million [36].

At speeds above usual ratings early failures have to be expected. Possible causes are lubricant starvation from centrifugal throw-off from the inner ring and cage, overheating, skidding of the rolling elements, centrifugal forces acting on rolling elements and centrifugal expansion of the components [35].

The centrifugal force acting on e.g. the balls with mass m is

$$F_c \propto mDN^2, \quad (2.1)$$

which for the assumption of DN being constant increases linear with speed N . Thus, when proceeding towards higher speeds and smaller bearing diameters, the centrifugal force is gaining significance although keeping DN constant. Due to the increase of centrifugal forces acting on the rolling elements, the distribution of applied loads is changed, which has a major impact on the bearing's lifetime. An investigation thereof is given in [37, 38]. Thus, the DN number seems not to reflect properly the scaling of rolling element bearings at ultra-high speeds and must therefore be used with caution.

In preceding works, ball bearings were operated at speeds of 500 krpm to 1 Mrpm corresponding to $DN = 1.6$ million to $DN = 3.2$ million [1, 2]. Comparing to the limiting values given in literature, one should think that operation at those DN numbers should be challenging but feasible. In fact, lifetime was very much reduced to a few hundred hours at $DN = 1.6$ million respectively a few minutes at $DN = 3.2$ million.

In general, bearing lifetime is a function of the rotational speed and the application specific bearing loading. For a given lifetime requirement the maximum allowable load can therefore be obtained as a function of speed. Basic speed-load charts for rolling element bearings as well as fluid film bearings are given in [34].

Taking into account the discussed limitations of ball bearings at high rotational speeds, an enhanced chart is obtained which is quantitatively depicted in Figure 2.3a). At low speeds the ball bearing's load is limited due to brinelling. As speed is increased, the load needs to be decreased because of material fatigue due to contact stress on raceways and balls. At a certain speed, excessive temperature needs to be avoided by further reducing the bearing's load and therewith the bearing's friction. Skidding due to centrifugal forces can be considered an ultimate condition. Preloading of the ball bearing would to some extent counteract skidding however, causing increased friction which would drive the bearing into over temperature. Thus, an ultimate speed is reached once skidding due to centrifugal force and/or over temperature cannot be avoided.

2.2 Magnetic Bearings

The main advantage of magnetic levitation in respect to high rotational speeds is its contact-less operation, which completely avoids wear and material fatigue and therefore no inherent lifetime limitation exists. A major advantage of AMBs is the controllability of the rotor dynamics. A disadvantage is its major complexity coming with the driving electronics, displacement sensors, control and the need of an emergency touchdown bearing. The space requirement for the bearings actuator is usually much higher than for ball or gas bearings of the same load capacity.

A large variety of different types of magnetic bearings exist. A classification of the different types and principles of magnetic levitation is given in [39]. One of the most common type of an AMB is the reluctance force bearing type, where an electromagnet on the stator is used to produce a pulling force acting on the ferromagnetic rotor. Force densities of up to 650 kN/m^2 can be obtained with this type of bearing, depending on the saturation flux density of the employed material [21].

Another type of magnetic bearing which has gained interest in recent bearing-less motors and high speed machines is the slotless Lorentz force

bearing [40,22,41]. The slotless design eliminates slot harmonic induced losses which would be imposed with slotted designs at high rotational speeds. A major advantage of the slotless Lorentz force type actuator is also its linear relation between bearing current and bearing force, which facilitates control. With the slotless design, i.e. with an air-gap winding, inductance is low and hence high control bandwidth can be achieved with a low driving voltage. The slotless Lorentz type actuator is therefore seen as the preferred choice for ultra-high-speed magnetic bearing applications.

With AMBs, a restriction on the achievable rotational speed is only given by the rotor materials stress under rotation and its burst limit. The maximum allowable load is mainly determined by the maximum allowable bearing current and the corresponding losses. With losses increasing with speed, the maximum load must be reduced. The corresponding speed-load diagram of the AMB is given in Figure 2.3c).

2.3 Gas Bearings

With fluid film bearings, load is provided by a liquid or gas film which is formed between the rotating and stationary members of the bearing. Separated by the fluid film, no contact of the bearing members occurs under normal conditions. Thus the bearing lifetime is widely unlimited. The working principles of liquid lubricated bearings and gas bearings are similar except that with gas bearings, the fluid is compressible and furthermore, viscosity is much lower. As a result, viscous friction is much lower, which makes the gas bearing a candidate for high speed applications.

Gas bearings can be of externally pressurized or self-acting types. With the externally pressurized bearing the fluid film is generated by means of pressurized air fed through orifices into the bearing clearance. In contrary, self-acting type bearings avoid the need of a pressurized air supply. Instead, the film is generated by viscous shear forces due the relative motion of journal and bushing under rotation. Self-acting bearing types have no load capacity at standstill. Hence at start-up, the journal first slides on the bushing surface until the fluid film is formed and the journal lifts off, carried by the fluid film. Lifetime limitations for self-acting type bearings are therefore imposed by the wear during start and stop. Thus the limiting factor is the number of start-stop cycles.

In the simplest case, the self-acting gas bearing is composed of a plain journal and a plain bushing as depicted in Figure 2.1. When the journal is centered in respect to the bearing bushing, the pressure within the fluid film is equal to the ambient. When the journal is displaced by ϵ as depicted, a converging air gap is formed. Due to journal rotation, the air is dragged into the converging gap resulting in an increasing pressure towards the converging gap. On the diverging gap, gas expands and a low pressure results. The pressure distribution around the journal yields a resulting force f_j which in the ideal case points straight into the bearing center and restores the journal to its centered position.

Unfortunately, it is common for most gas bearing types that not only a restoring force pointing into the center is present but also a force perpendicular thereto. This tangential force component is one of the main causes for the self-excited whirl instability which finally imposes a limitation on the achievable rotational speed. Given sufficient damping by the fluid film itself, a certain amount of the destabilizing tangential force can be tolerated and the journal will converge in a spiral orbit to the bearing center. If damping is insufficient, the orbit of the displacement will increase and finally reach the ultimate limit cycle given by the bearing clearance and the journal will touch the bushing wall. Stability is usually worsened when heavy rotors need to be supported and as a result, instability onset occurs already at lower speeds.

The self-acting plain journal bearing is the type of bearing where the phenomenon of whirl instability is most striking; it does however occur with any type of gas bearing and even with externally pressurized bearings. The phenomenon of whirl instability has been known from the beginning of fluid film lubrication and is studied e.g. in [42]. A variety of different gas bearing types has been invented in order to cope with the problem of whirl instability. An overview of self-acting bearing types is given in [43]. Drawings of the most common bearing types are given in Figure 2.2.

Grooved bearings contain micro structures on either the bearing journal or the bushing in order to generate a pressure profile, also when the rotor is centered. The herringbone grooved bearing, the Rayleigh step bearing and the lobed bearings fall in this category. The herringbone grooved bearing uses inward pumping grooves for pressure build-up under rotation, and the Rayleigh step journal bearing has ax-

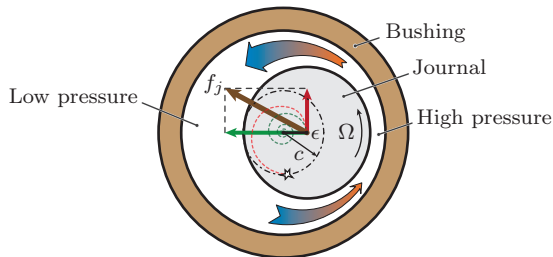


Figure 2.1: Illustration of working principle of self-acting gas bearings with pressure build-up due to a converging bearing clearance and viscous shear forces (bearing clearance not drawn to scale).

ial grooves in order to generate a converging gap profile for pressure build-up. Also the lobed bearing uses the principle of a converging gap. With these bearings, the structure is rigid and is not thought to change under operation.

In contrary, tilting-pad bearings have flexible structures which adapt themselves to the governing film pressure. Also in foil bearings, compliant structures yielding to the journal displacement and adapting to the film pressure are used. Foil bearings are commonly constructed with a bump foil, which is covered by a top foil.

A major advantage of the bearing types with compliant structures is the capability to self-align, resulting in a relatively high tolerance to manufacturing deviations and misalignment. Moreover, the compliant structure can be designed to provide additional damping in order to improve the bearings dynamic stability. Modeling however is more complex compared to fixed geometry bearings because the compliant structure, which is yielding to the resulting pressure distribution, needs to be incorporated into the modeling. Often, an empirical approach is therefore followed with foil bearings.

A typical speed-load diagram of a self-acting gas bearing is given in Figure 2.3b). Starting from zero load capacity at standstill, load capacity gradually increases with speed. The achievable load capacity is defined by the speed dependent pressure distribution. When considering the inert mass of the supported rotor as a bearing load, rotor mass must be reduced when proceeding towards higher speeds in order to retain dynamic stability. An ultimate speed limitation is given by the rotor material's stress under rotation, i.e. its burst limit.

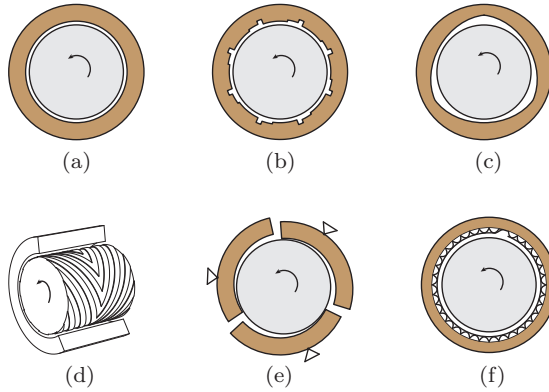


Figure 2.2: Self-acting gas bearing types (gap geometry is not drawn to scale): plain journal bearing (a), Rayleigh step journal bearing (b), three-lobe journal bearing (c), herringbone grooved journal bearing (d), tilting-pad journal bearing (e) and foil-bearing (d).

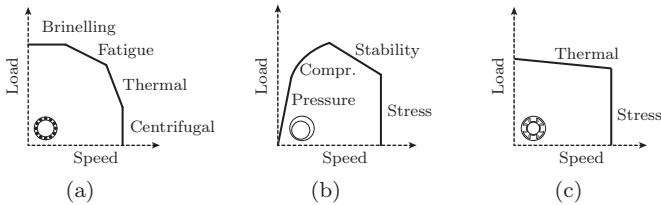


Figure 2.3: Speed and load limitations for ball bearings (a), gas bearings (b) and magnetic bearings (c).

2.4 Comparison of Bearing Types

A comparison of the discussed bearing types is given in tabular form in Table 2.1. Nominal load capacity is usually highest with ball bearings. However, in order to reach high speeds, loading needs to be reduced drastically and will become comparable to the load capacity achieved with gas bearings. Although load capacity per surface area of magnetic bearings can be much higher than with gas bearings, compared to the required installation size of the actuator, load capacity of magnetic bearings can only be rated fair. A further drawback of the increased

installation size coming with actuators, displacement sensors and touch-down bearings is usually the demand for additional rotor length, which may be problematic for rotor-dynamic reasons.

Static stiffness of AMBs depends on the employed control law and can therefore theoretically be infinite, depending on the resolution and quality of the used displacement sensor. The dynamic stiffness however is given by the control bandwidth which always is limited.

Ball bearings usually need oil or grease lubrication which can be a source of failure due to deterioration. Both magnetic bearings and gas bearings operate oil-free which makes them more robust in this perspective. The oil-free operation makes them also possible bearing candidates for high temperature environments. Furthermore, oil-free operation is a key requirement for certain applications, such as turbo-compressors in fuel cells or heat pumps.

With AMBs, dynamic stability is given by active control. However, this benefit comes with the major complexity of the AMB system. With gas bearings, dynamic stability is the main challenge, especially when supporting heavy rotors at high speeds. In order to obtain stability also at high speeds, scaling of the bearing clearance is usually needed which however leads to very tight or infeasible manufacturing tolerances and moreover negatively impacts the bearing viscous friction losses.

While ball bearings represent a robust solution with long lifetime for high speed applications in terms of the DN number at large scale, they do not meet the lifetime requirements for miniature scale applications with high rotational speeds in terms of rotations per unit time ranging up to 1 Million rpm. The ball bearing is therefore no candidate for miniature high speed applications. Gas bearings and magnetic bearings remain as possible options.

2.5 Gas-Magnetic Hybrid Bearing Concept

Concluding from the above bearing comparison, the AMB and the gas bearing remain as possible candidates fulfilling the basic requirement for high lifetime at high rotational speeds. When deciding for one of the two bearing types, one has to either accept the major increase of installation size and system complexity introduced by the AMB system or one has to cope with the stringent manufacturing tolerances and the limitation for a maximum allowable rotor weight imposed by the critical dynamic stability of the gas bearing.

	Ball bearing	AMB	Gas bearing
Load capacity	good	fair	good
Stiffness	high	good	good
Installation Size	compact	bulky	compact
Lubricant	grease/oil	none	ambient gas
Dyn. stability	not critical	controllable	critical
Fabr. tolerance	high	low	very high
System complexity	low	very high	low
Lifetime	insufficient	unlimited	start/stop

Table 2.1: Comparison of ball bearing, AMB and self-acting gas bearing for ultra-high-speed use.

A hybrid bearing approach employing a gas bearing as the main load carrying element in combination with a small sized magnetic bearing or damper for stabilization of the gas bearing at high rotational speeds can minimize or eliminate the main shortcomings of the individual bearing types. In order to derive full advantage of the hybrid bearing concept the following measures need to be taken.

- ▶ In order to render fabrication possible or easier, manufacturing tolerances need to be relaxed. As a result, the gas bearing clearance must be increased in regard to a theoretical bearing design yielding dynamic stability by itself at high rotational speeds. The main consequence thereof is a decrease in dynamic stability which will have to be counteracted by magnetic stabilization. As a benefit resulting from the larger bearing clearance, lower viscous friction losses result and therewith, a higher overall system efficiency can be obtained.
- ▶ As the gas bearing provides the load capacity, the magnetic damper can be designed of reduced size. It only needs to provide forces when the rotor is unsteady and whirling motion occurs.
- ▶ In order to avoid additional rotor length, integration of the magnetic damper into the electric machine's active region is aimed. In a machine design with magnetic bearing support, such systems are commonly referred to as self-bearing motors or bearing-less motors [44, 40].

- Size and complexity of the drive system can be further reduced when the rotor displacement measurement is achieved in a self-sensing technique, avoiding the need of dedicated displacement sensors for feedback control. In a heteropolar AMD implementation, the same is true for the angular rotor position measurement, which is needed for field oriented control.

With the hybrid bearing approach, the choice of the type of gas bearing is not a priori given. A drawing of a possible hybrid bearing realization with herringbone grooved bearings and AMD windings integrated into the active region of high speed slotless permanent magnet machine is shown in Figure 2.4. Besides the gas lubricated journal bearings for radial load support, also a gas lubricated thrust bearing is needed for axial support. In contrary to journal bearings, dynamic stability of thrust bearings is usually much less of a concern. Therefore, no active magnetic stabilization of the thrust bearing must be considered.

The new challenge involved with the hybrid bearing approach is seen in the requirement for a high sensitivity and high resolution displacement measurement with sufficient bandwidth in order to control the rotor displacement within the gas bearing's clearance which is in the order of some micrometers. Thus, the challenge is shifted from ultra-precise fabrication of the gas bearing parts to the design of a high performance measurement electronics.

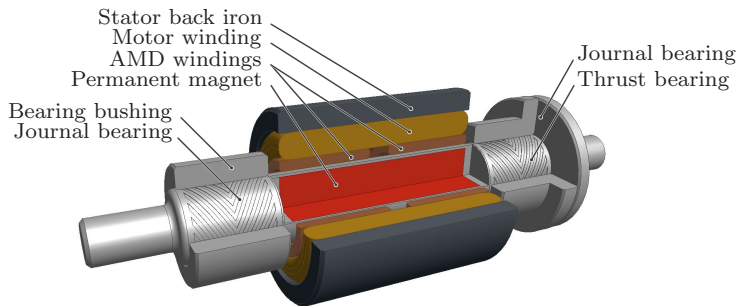


Figure 2.4: CAD drawing of a possible realization of a slotless permanent magnet machine with a hybrid bearing system consisting of herringbone grooved journal bearings for radial load support and active magnetic dampers for stabilization of the gas bearings at high rotational speeds.

Chapter 3

Modeling and Design of Gas Bearings

For the design of a hybrid bearing system consisting of a gas bearing and an AMD, the basic properties of gas bearings need to be understood. Therefore, known fundamentals of gas bearing modeling are summarized. The governing Reynolds equation and established dimensionless numbers for the scaling of gas bearings are discussed. The viscous friction losses and the related thermal rotor growth are analyzed. Furthermore, the critical design parameters in respect to the dynamic stability of gas bearings at high operational speeds are studied.

For the analysis of a bearing-rotor system, a dynamic model of the gas bearing is finally needed. Therefore, a numerical scheme for the calculation of the bearing film pressure is given and the modeling by means of a linear time invariant system (LTI) is presented.

3.1 Reynolds Equation

The differential equation governing the pressure distribution in a fluid-film bearing was first derived by Osborne Reynolds in 1886 and is therefore known as the “Reynolds equation” [45]. A detailed derivation of the Reynolds equation can be found in [45]. The Reynolds equation can be obtained from the Navier-Stokes and continuity equations or from the laws of viscous flow and the principle of mass conservation. The

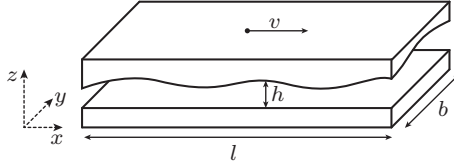


Figure 3.1: Plates with parallel motion v . The pressure distribution in the clearance with variable height h is governed by the Reynolds equation.

derivation is based on the assumption of laminar flow and a negligible inertia of the fluid.

Reynolds Equation in Cartesian Coordinates

For the case of two plates with parallel relative motion v in x direction as visualized in Figure 3.1 the pressure p of the fluid film formed between the two plates is given by the so-called Reynolds equation as

$$\frac{\partial}{\partial x} \left(-\frac{\rho h^3}{12\eta} \frac{\partial p}{\partial x} \right) + \frac{\partial}{\partial y} \left(-\frac{\rho h^3}{12\eta} \frac{\partial p}{\partial y} \right) + \frac{\partial}{\partial x} \left(\frac{\rho h v}{2} \right) + \frac{\partial}{\partial t} (\rho h) = 0, \quad (3.1)$$

where h denotes the local film height, ρ is the lubricant density and η the dynamic viscosity. The first two terms of (3.1) are referred to as Poiseuille flow terms and represent the mass flow rates due to a pressure gradient while the third term is referred to as Couette flow term and describe the entraining flow rate due to the surface velocity. The fourth term originates from the principle of mass conservation and represents the accumulating mass in an infinitely small volume within the lubricant.

For scaling of fluid film bearings, a dimensionless form of the Reynolds equation is commonly used. Therefore, the normalization

$$P = p/p_a \quad (3.2)$$

$$H = h/h_{min} \quad (3.3)$$

$$X = x/l \quad (3.4)$$

$$Y = y/b \quad (3.5)$$

$$\tau = t \cdot \omega \quad (3.6)$$

is applied, where p_a is the ambient pressure, h_{min} is the minimum of the local film thickness, l and b are the length and width of the lubrication area and ω is an arbitrary excitation frequency. For gas lubricated bearings, the fluid is compressible and the density is a function of the pressure p . Assuming ideal gas, the pressure p is given by the relation

$$\rho = \frac{p}{R_{spec}T}, \quad (3.7)$$

where R_{spec} is the specific gas constant and T the gas absolute temperature [45]. Note that for compressible fluids, i.e. with the density being a function of the pressure, the Reynolds equation is becoming a non-linear partial differential equation which cannot be solved in a closed analytical form. Using the above normalization and substituting (3.7) into (3.1), the dimensionless Reynolds equation [45] can be given as

$$-\frac{\partial}{\partial X} \left(PH^3 \frac{\partial P}{\partial X} \right) - \lambda^2 \frac{\partial}{\partial Y} \left(PH^3 \frac{\partial P}{\partial Y} \right) + \Lambda \frac{\partial(PH)}{\partial X} + \sigma \frac{\partial(PH)}{\partial \tau} = 0 \quad (3.8)$$

with the length to width ratio

$$\lambda = \frac{l}{b}, \quad (3.9)$$

the dimensionless bearing number¹

$$\Lambda = \frac{6\eta vl}{p_a h_{min}^2} \quad (3.10)$$

and the dimensionless squeeze number²

$$\sigma = \frac{12\eta\omega l^2}{p_a h_{min}^2}. \quad (3.11)$$

Reynold Equation in Cylindrical Coordinates

With journal bearings, the fluid film is formed in the gap between the bearing bushing and the rotating journal. Therefore, a representation of the Reynolds equation in cylindrical coordinates (r, θ, z) is applicable. The definition of the coordinate system used with the journal bearing

¹also referred to as bearing compressibility number

²also referred to as frequency number

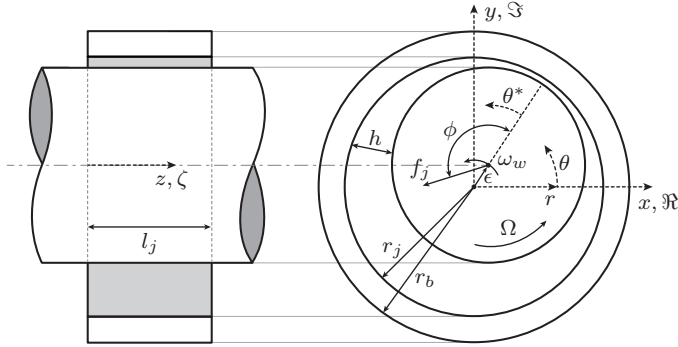


Figure 3.2: Parameter definition and coordinate systems for a journal bearing.

is depicted in Figure 3.2. The journal displacement ϵ and bearing force f_j are represented in a Cartesian coordinate system (x, y) . A complex plane $(\mathfrak{R}, \mathfrak{S})$ is also introduced which is used later for a simplified notation of ϵ and f_j as complex numbers.

In order to obtain the Reynolds equation in cylindrical coordinates for a journal rotating with a angular speed Ω ,

$$x = r_j\theta \quad y = r_j\zeta \quad v = r_j\Omega \quad (3.12)$$

is substituted into (3.1). Normalizing with

$$P = p/p_a \quad H = h/c \quad \tau = t \cdot \omega, \quad (3.13)$$

where c denotes the bearing's nominal centered film clearance, yields

$$-\frac{\partial}{\partial\theta} \left(PH^3 \frac{\partial P}{\partial\theta} \right) - \frac{\partial}{\partial\zeta} \left(PH^3 \frac{\partial P}{\partial\zeta} \right) + \Lambda_j \frac{\partial(PH)}{\partial\theta} + \sigma_j \frac{\partial(PH)}{\partial\tau} = 0. \quad (3.14)$$

For the journal bearing, the bearing number is defined as

$$\Lambda_j = \frac{6\eta\Omega r_j^2}{p_a c^2} \quad (3.15)$$

and the squeeze number is

$$\sigma_j = \frac{12\eta\omega r_j^2}{p_a c^2}. \quad (3.16)$$

As bearings with the same dimensionless numbers yield the same dimensionless pressure distribution, scaling or comparison of gas bearings can be accomplished by means of the dimensionless numbers.

3.2 Scaling of Gas Bearings

In the previous section, the dimensionless Reynolds equation has been introduced as the governing equation for the pressure distribution of the bearing's fluid film. Therefrom, the dimensionless numbers Λ_j and σ_j have been defined, which allow comparison and scaling of gas bearings to a certain extent. For static bearing properties, the bearing number Λ_j is considered. When dynamic properties are investigated, σ_j would come into play.

Load Capacity

The dimensionless load capacity can be introduced as

$$F_j = \frac{f_j}{\varepsilon p_a l_j 2r_j}, \quad (3.17)$$

where $\varepsilon = \epsilon/c$ is the normalized displacement. The load capacity is determined by the pressure distribution in the fluid film bearing and is therefore a function of the bearing number $F_j(\Lambda_j)$.

The dimensionless load capacity $F_j(\Lambda_j)$ has been calculated for the infinitely wide plain journal bearing [46] and also for infinitely wide Rayleigh-step journal bearings [47]. Although these theoretical solutions for infinitely wide bearings neglecting side leakage flow seem to be of little practical use, they represent limiting solutions for the maximum achievable load capacity of these bearing types. With finite bearing width, load capacity compared to the infinitely wide solution is decreased because of side leakage flow having a major influence on the bearing performance. Consequently in literature, bearing scaling charts are often presented in dependence of the width-to-diameter ratio

$$\lambda_j = \frac{l_j}{2r_j}. \quad (3.18)$$

Load capacity design charts for plain journal bearings with finite width have been given in [48] where a perturbation method was used to linearize the Reynolds equation and obtain an approximate solution of the

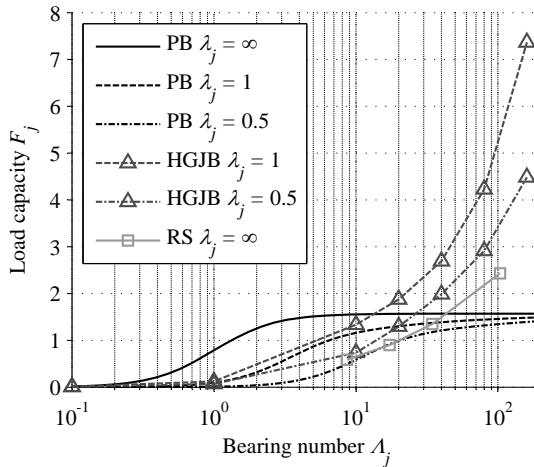


Figure 3.3: Load capacity of plain bearing (PB) [48], herringbone grooved journal bearing (HGJB) [49] and a six-step Rayleigh-step journal bearing (RS) [47].

pressure distribution. In [49], load capacity design charts for herringbone grooved journal bearings have been presented for various values of λ_j .

Figure 3.3 plots the dimensionless load capacity from [47, 48, 49] for the plain, herringbone grooved and Rayleigh step bearing in comparison, in dependency of λ_j and λ_j . Towards high bearing numbers, the load capacity of the plain bearing is converging to a limiting value, as a result of the compressibility of the gas lubricant. The herringbone grooved journal bearing overcomes this compressibility effect. As a result of the inward pumping grooves, its load capacity increasing without limit towards higher bearing numbers [49]. For both plain and herringbone grooved bearing it is seen, that load capacity decreases towards smaller λ_j , as a result of side leakage. In respect to load capacity, the Rayleigh step bearing resides between plain and herringbone grooved bearing.

Stability

One of the most limiting factors in the use of gas bearings and their operation at high rotational speeds is the phenomenon of whirl instability. A measure to quantify the stability of gas bearings has been introduced in [50] with the definition of the dimensionless stability parameter

$$M_j = \frac{mp_a}{2\eta^2 l_j} \left(\frac{c}{r_j} \right)^5. \quad (3.19)$$

The definition originates from the modeling of a concentrated mass m supported by a gas bearing (see also Section 3.7.1). With the definition of M_j , m denotes the maximum mass supported by the bearing such that the bearing-mass system is still operating stable. A heavier mass than m will generally render the system unstable and a smaller mass will yield stability.

The definition represents a simple and comprehensible mean for the comparison of different gas bearing designs or also different gas bearing types. In a design phase, it can therefore be a parameter to optimize for without anticipating already further knowledge of a finally constructed bearing-rotor system. Clearly, for a final system design consisting of a rotor and a set of gas bearings, an in-depth stability analysis based on a more accurate rotor model will usually be needed to ensure stability.

Data for the stability parameter M_j of optimized herringbone journal bearings has been provided in tabular form in [50] which is plotted in Figure 3.4. It can be seen that stability decreases with increasing bearing numbers and hence it also decreases with speed because $\Lambda_j \propto \Omega$. As $m \propto M \cdot c^{-5}$ and the bearing number scales as $\Lambda_j \propto c^{-2}$, an increase of stability, i.e. an increase of the supported mass m , can generally be achieved by decreasing the bearing clearance. Thus, an increase in rotational speed generally demands for a reduction of the bearing clearance, in order to retain stability. The same conclusion is also made in [51].

Unfortunately scaling of bearing clearance is only conditionally possible. Viscous friction will increase with a smaller clearance (see Section 3.4) and in order to guarantee a designed film clearance in absolute measures, fabrication tolerances will have to be tightened. As an example, a parametric analysis of a specific Rayleigh step bearing design in respect to stability is given in Section 3.8.

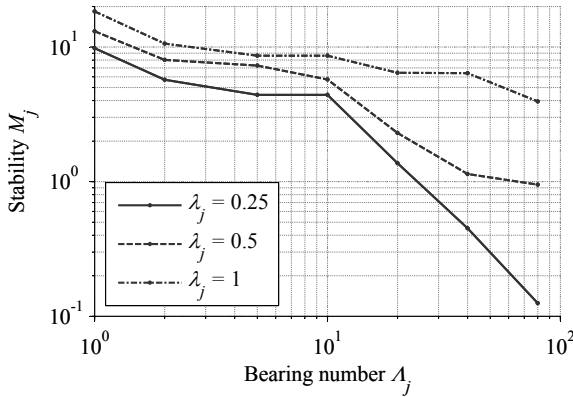


Figure 3.4: Stability parameter M_j against bearing number Λ_j for optimized herringbone journal bearings with different width-to-diameter ratios (data from [50]).

3.3 Gas Bearing Reaction Forces

As a result of the film pressure generated in the bearing clearance, a force is exerted on the journal. Assuming small journal displacements, the force can be written as a linear function of the journal displacements ϵ_x and ϵ_y in x and y direction as

$$f_{j,x} = c_{xx}(s) \cdot \epsilon_x + c_{xy}(s) \cdot \epsilon_y \quad (3.20)$$

$$f_{j,y} = c_{yx}(s) \cdot \epsilon_x + c_{yy}(s) \cdot \epsilon_y \quad (3.21)$$

The functions $c_{xx}(s)$, $c_{xy}(s)$, $c_{yy}(s)$ and $c_{yx}(s)$ can be assumed rational functions in the Laplace variable s , representing the dynamic stiffness of the bearing as LTI systems. A definition of the coordinate system used for the representation of the journal displacement and the resulting force is given in Figure 3.2. Given the rotational symmetry of the journal bearing,

$$c_{xx} = c_{yy} \quad \text{and} \quad c_{xy} = -c_{yx} \quad (3.22)$$

must comply. The displacement, stiffness and bearing force can therefore be written in a complex representation as

$$f_j = f_{j,x} + jf_{j,y} \quad c_j(s) = c_{xx}(s) + jc_{xy}(s) \quad \epsilon = \epsilon_x + j\epsilon_y, \quad (3.23)$$

which then allows the notation

$$f_j = c_j(s) \cdot \epsilon. \quad (3.24)$$

Two force components contribute to the bearing force, namely a normal force component and a shear force component. The normal force component results from the pressure distribution of the fluid film around the circumference of the journal bearing. The normal force is obtained by integrating the pressure over the total lubrication area as

$$f_{j,p} = -r_j l_j \cdot \int_0^{2\pi} \int_0^1 p \cdot e^{i\theta} d\theta d\zeta, \quad (3.25)$$

where $e^{i\theta}$ is the surface normal unit vector. For a perfectly centered rotor, $f_{j,p} = 0$ complies for symmetry reasons. For a displaced rotor, the force is ideally pointing in the opposite direction of the displacement, restoring the journal to its centered position.

The shear force component results from viscous friction and can be calculated from the shear stress distribution [45], which is given as

$$\tau_{r\theta} = \frac{h}{2r} \frac{\partial p}{\partial \theta} + \frac{\eta \Omega r}{h}. \quad (3.26)$$

It is acting in tangential direction opposing to the surface velocity of the journal. The shear force acting on the journal is then obtained by integration over the journal surface as

$$f_{j,sh} = -r_j l_j \cdot \int_0^{2\pi} \int_0^1 \tau_{r\theta} \cdot j e^{j\theta} d\theta d\zeta, \quad (3.27)$$

where $j e^{j\theta}$ is the surface tangential unit vector. Again, for a perfectly centered journal $f_{j,sh} = 0$ complies for symmetry reasons.

The resulting bearing force is the sum of the two forces as

$$f_j = f_{j,p} + f_{j,sh} \quad (3.28)$$

The angle between the displacement ϵ and the resulting force f_j

$$\phi = \arg\left(\frac{f_j}{\epsilon}\right). \quad (3.29)$$

is referred to as the attitude angle of the bearing. Ideally, the attitude angle of a bearing at steady state is 180° , pointing directly to the bearing center; it is seen later that a deviation therefrom always decreases the bearing's stability.

3.4 Friction Losses

The friction torque is obtained by integrating the shear stress given in (3.26) over the lubrication area as

$$T_{fr} = r_j^2 l_j \cdot \int_0^{2\pi} \int_0^1 \tau_{r\theta} d\theta d\zeta. \quad (3.30)$$

For a concentric journal, (3.30) reduces to

$$T_{fr} = \frac{2\pi\eta r_j^3 l_j \Omega}{c}, \quad (3.31)$$

which is known as the Petrov's equation [45]. The bearing friction losses are then given by

$$P_{fr} = \Omega T_{fr} = \frac{2\pi\eta r_j^3 l_j \Omega^2}{c}. \quad (3.32)$$

Viscous friction scales inversely proportional to the bearing clearance. Thus, when proceeding towards smaller bearing clearances as a consequence of e.g. retaining stability at elevated rotational speeds or due to increased rotor mass, higher friction losses will have to be coped with.

3.5 Centrifugal and Thermal Expansion

The nominal clearance of a gas bearing ranges by design between a few micrometers to some tens of micrometers which is compared to the dimension of the journal diameter very small. A small absolute change of a few micrometers in journal or bushing diameter may therefore alter the relative dimension of the bearing clearance considerably and as a consequence affect the bearing's performance. Besides manufacturing imperfection, the bearing's clearance can deviate from its nominal design value due to centrifugal expansion of the journal as well as thermal strain. With both effects being dependent on rotational speed (obvious for centrifugal expansion and linked with viscous friction losses for thermal strain), their impact on high speed operation requires further contemplation.

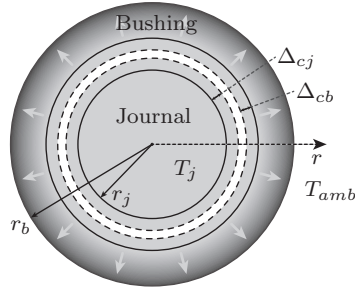


Figure 3.5: Thermal model of journal bearing with radial heat flow for calculation of thermal expansion of the journal Δ_{cj} and the bushing Δ_{cb} (bearing clearance not drawn to scale).

Centrifugal Rotor Expansion

In order to obtain an estimate of the radial expansion of the journal under rotation, the journal is considered a solid plain cylinder. The clearance reduction due to radial expansion is given by the displacement of the journal on its surface as

$$\Delta_{c\Omega} = -\frac{(1-\nu)\rho\Omega^2 r_j^3}{4E} \quad (3.33)$$

where E is the journal material elastic modulus, ρ its density and ν its Poisson's ratio [52].

Thermal Expansion and Clearance Reduction

Unequal thermal expansion of the bearing journal and the bushing can be identified as another cause of a bearing clearance distortion. Even when the journal and bushing materials are matched in regard to their coefficient of thermal expansion, a clearance change may occur due to thermal strain caused by a nonuniform temperature distribution in the journal and the bushing. As the temperature distribution is governed by the bearing friction losses P_{fr} as the main heat source which is increasing with rotational speed, the problem can be expected to aggravate when progressing towards higher rotational speeds.

A rudimentary thermal bearing model is used in order to study the fundamental limitations due to thermal strain imposed to fixed geometry gas bearings. Assuming rotational symmetry, a perfectly centered

journal and purely radial heat flow, the mathematical formulation of the thermal problem can be accomplished in cylindrical coordinates as depicted in Figure 3.5. With the assumption of purely radial heat flow, the temperature in the journal must be constant because of the absence of heat sinks or sources within the journal. Hence, the clearance reduction due to the thermal growth of the journal is

$$\Delta_{cj} = -\alpha_j r_j (T_j - T_{ref}), \quad (3.34)$$

where α_j is the material's coefficient of thermal expansion, T_j is the journal temperature and T_{ref} is the nominal temperature specified by design.

In the bearing bushing, a temperature gradient in radial direction exists because of the heat generated in the bearing clearance which is conducted to the outer surface of the bushing. With the temperature T being a function of r , thermal stresses are present in the bushing. Thus, the displacement on the inner surface of the journal must be calculated with the help of equations from the theory of elasticity.

In a first step, the temperature distribution along the radial direction has to be calculated. The radial temperature drop over a hollow cylinder element with a radius r , a wall thickness dr and length l_j can be derived from the definition of the material conductivity λ as

$$dT = \frac{P_{fr} dr}{2\pi r l_j \lambda}, \quad (3.35)$$

where P_{fr} are the viscous friction losses generated in the bearing clearance. Integration yields the temperature distribution

$$T(r) = T_j - \int_{r_j}^r \frac{P_{fr} dr}{2\pi r l_j \lambda} = T_j - \frac{P_{fr}}{2\pi l_j \lambda} \log\left(\frac{r}{r_j}\right). \quad (3.36)$$

The bearing journal temperature T_j can be calculated assuming a thermal equivalent resistor R_{amb} to the ambient at temperature T_{amb} as

$$T_j = T_{amb} + P_{fr} R_{amb} + \frac{P_{fr}}{2\pi l_j \lambda} \log\left(\frac{r_b}{r_j}\right), \quad (3.37)$$

where r_b is the bushing outer radius.

With the calculated temperature distribution $T(r)$, the radial growth of the bearing bushing can be obtained following [53]. Assuming mechanically free surfaces on the outer diameter of the bearing bushing,

the radial growth at the inner surface of the bushing is given by

$$\Delta_{cb} = C_1 r_j + \frac{C_2}{r_j}, \quad (3.38)$$

where the constants C_1 and C_2 are given by

$$C_1 = \frac{(1 - \nu)\alpha_b}{r_j^2 + r_b^2} \int_{r_j}^{r_b} (T(r) - T_{ref}) r dr \quad (3.39)$$

$$C_2 = \frac{(1 + \nu)\alpha_b r_j^2}{r_j^2 + r_b^2} \int_{r_j}^{r_b} (T(r) - T_{ref}) r dr, \quad (3.40)$$

and α_b is the coefficient of thermal expansion of the bushing's material.

Assuming equal coefficients of thermal expansion $\alpha_j = \alpha_b = \alpha$ which is approximately the case when e.g. choosing bronze (CuSn8) for the bushing material and stainless steel (1.4301) for the journal, the total clearance change due to thermal expansion can be written as

$$\Delta_{cT} = \Delta_{cb} + \Delta_{cj} = -K_c \cdot r_j \cdot \frac{P_{fr}}{l_j} \quad (3.41)$$

with

$$K_c = \frac{\alpha}{4\pi\lambda} \cdot \frac{(2 \log(\frac{r_b}{r_j}) - 1)r_b^2 + r_j^2}{r_b^2 - r_j^2}. \quad (3.42)$$

As a consequence of the equally assumed expansion coefficients, Δ_{ct} is independent of the bearing's thermal connection to the ambient: T_{amb} and R_{amb} have no influence. Therefore, the cooling conditions of the bearing bushing do not influence the thermally conditioned clearance change. This fact is rather fortunate as the bearing characteristics remain widely unchanged for different cooling conditions.

Influence on the thermally conditioned clearance change can be taken by the choice of the bearing bushing's outer radius. Considering that

$$\lim_{r_b \rightarrow r_j} \Delta_{cT} = 0, \quad (3.43)$$

the clearance change is minimized by choosing r_b as close to r_j as possible. Thus, in a design minimizing a potential clearance change, the bushing's wall thickness is chosen as small as mechanical strength for handling, assembly and operation allows.

Clearance Reduction and Friction Losses

In the previous section, bearing clearance reduction due to thermal strain has been calculated based on presumed bearing friction losses. In Section 3.4 the friction losses have been given as a function of the bearing clearance. A change in bearing clearance due to thermal strain will affect the bearing friction losses which in turn will change the temperature distribution of the bearing. The resulting change in thermal strain finally alters again the clearance and so on. The effective bearing clearance and the friction losses are therefore strongly coupled.

The bearing friction losses can be rewritten from (3.32) as a function of the thermal clearance change as

$$P_{fr} = \frac{2\pi\eta r_j^3 l_j \Omega^2}{c_{nom} + \Delta_{cT}}, \quad (3.44)$$

where c_{nom} denotes the nominal bearing clearance. Combining with (3.41) yields a quadratic equation for the steady state clearance change which has one physically meaningful solution with

$$\Delta_{cT} = -\frac{c_{nom}}{2} \left(1 - \sqrt{1 - 8\pi\eta r_j^4 \Omega^2 K_c / c_{nom}^2} \right) \quad (3.45)$$

A real solution only exists when

$$8\pi\eta r_j^4 \Omega^2 K_c / c_{nom}^2 > 1, \quad (3.46)$$

meaning that otherwise the bearing will be thermally unstable. For many common gas bearing designs, thermal instability is usually unproblematic. However when proceeding towards higher speeds and possibly smaller clearances, thermal instability can occur depending on the choice of the bearing materials, dimensions and assembly. Hence, these points should be addressed in high speed gas bearing design.

As an example, Figure 3.6 shows the viscous friction losses for two different bearing designs which parameters are listed in Table 3.1, for speeds up to 500 krpm. The only difference of the two bearing designs is the outer radius of the bearing bushing. While the bearing A has a bushing designed as a cylinder liner with a wall thickness of 1 mm, the bushing of bearing B has an outer radius of 15 mm as would e.g. be the case when combined into the motor flange as a single part. It can be seen that the bearing design A has only slightly higher losses compared to the nominal loss curve where a constant clearance over

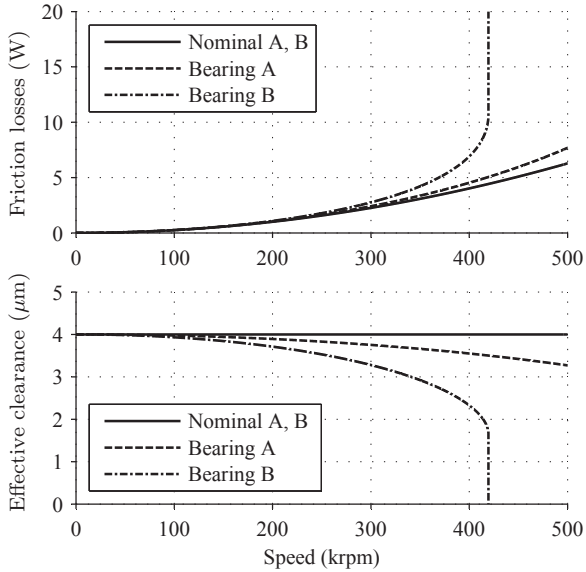


Figure 3.6: Viscous friction losses and bearing clearance change of two different bearing designs according to Table 3.1: calculation with nominal clearance (solid line) and under consideration of centrifugal rotor growth and thermal expansion for bearing design A (dashed line) and bearing design B (dash-dotted line). Bearing design B becomes thermally unstable around 420 krpm.

speed is assumed. Accordingly, the effective change in film clearance is less than one micrometer at 500 krpm. Bearing design B however differs heavily towards higher speeds and is becoming thermally unstable at around 420 krpm where the friction losses diverge and the bearing clearance shrinks to zero.

3.6 Numerical Modeling of Gas Bearings

In order to analyze the dynamic stability of a bearing-rotor system, a model reflecting the transient behavior of the gas bearing is needed. This requires to solve the Reynolds equation, which as discussed in Section 3.1, is a nonlinear partial differential equation for the bearing film

Quantity	Symbol	Bearing A / B
Nominal clearance	c_{nom}	4 μm
Journal radius	r_j	3 mm
Bushing outer radius	r_b	4 mm / 15 mm
Bearing length	l_j	6 mm
Journal material		Steel 1.4301
Bushing material		Bronze CuSn8

Table 3.1: Example bearing parameters for friction loss comparison

pressure P . As a consequence of the nonlinearity, a closed analytical solution cannot be given and the pressure distribution needs to be computed by numerical methods. Both finite element methods (FEM) as well as finite difference methods (FDM) have been applied in the field of fluid film lubrication [54]. Beginning with a short review on the numerical modeling of gas bearings, a FDM scheme in combination with a linearization method is presented which permits to model the transient bearing behavior as a LTI system.

3.6.1 Review on Numerical Modeling of Gas Bearings

Discretization of the Reynolds equation by means of FDM is usually accomplished by the introduction of an equally spaced grid, dividing the lubrication domain into discrete elements. Based on the introduced grid, the derivatives in the Reynolds equation are consequently approximated by finite differences. The FDM is usually applied straightforward due to its simplicity. It is favored for modeling domains with simple geometries which are preferably of rectangular shape. When proceeding to more complex shapes which require a variable grid spacing, the advantage of the simplicity with FDM is usually lost. For more complicated shapes, the FEM is therefore preferred. However, it generally involves a higher complexity with the implementation, also with simple geometries.

For both FEM and FDM, advanced numerical methods such as a high order Galerkin scheme [54] or a finite difference based multigrid approach [55] have been proposed in order to cope with increased bearing numbers $\Lambda_j > 100$ and the related numerical instability encountered

with ordinary solvers. Even though it could be suspected that very high bearing numbers will result when proceeding to rotational speeds of 500 krpm and beyond, they in fact are moderate compared to other applications of fluid film lubrication such as encountered in ultra-thin film computer disc sliders. Bearing numbers for the targeted bearing designs and are not expected to significantly exceed $\Lambda_j > 100$. Thus, an ordinary method such as a basic FDM can be used.

In order to predict stable and unstable behavior of the gas bearing in combination with a supported rotor, a characterization of the transient behavior of the bearing is needed. A number of approaches have been proposed in literature to predict the dynamic behavior of gas bearings.

Probably the most intuitive approach the orbit method, which combines transient simulation of the Reynolds equation together with the equations of motion of the supported rotor. The time-domain simulation of the full set of differential equations in order to obtain the journal orbit or trajectory is however computationally very intensive. Direct simulation of the journal trajectory is useful when the bearing's nonlinear properties are investigated [56, 57, 58]. Besides the computational effort, a further shortcoming of the orbit method is also that the simulation results depend on the choice of the initial conditions, such that it is difficult to make a general conclusion on the bearing's stability. Moreover, the choice of the time step together with the implementation of the time integration is crucial concerning the introduction of unwanted numerical damping which might distort the simulation result.

A technique which requires less computational effort is the so-called step-jump method [59, 60]. Based on a transient simulation of the bearing response to a forced displacement step, the transient behavior can be approximated by means of a lumped parameter model. Model identification can be based on a fit to Laguerre polynomials [59] or also to an LTI system. Fitting the bearing step response to a parametric model however requires careful attention in order to obtain a physically sound representation which in particular does not violate the second law of thermodynamics [61]. As with the orbit-method, the choice of an appropriate time step for the step response simulation is crucial because of numerical damping and the difficulty of representing both slow and fast transients with sufficient accuracy.

Procedures avoiding time simulation are based on transforming the Reynolds equation into the frequency domain by means of a perturbation technique [62, 63] or by applying an appropriate coordinate trans-

formation [42, 64]. Solving the Reynolds equation in the frequency domain is equivalent to solving the stationary equation which then imposes no extra difficulties. From the frequency domain solution, the frequency dependent stiffness and damping coefficients can be extracted [54] or a frequency domain model fit to an LTI system can be performed.

With the frequency domain approach, the bearing's behavior is usually investigated in its nominal operating point where a linearization of the governing equations is performed. Hence, the bearing's nonlinear properties then are lost. In order to avoid this drawback, a method employing piecewise linear approximations has been proposed in [65].

In the present thesis, a linearization of the Reynolds equation is used to obtain a set of linear equations describing the transient behavior of the gas film. A model order reduction is then applied, to reduce the computational effort for the subsequent stability analysis. A similar approach has also been presented in [66].

3.6.2 Numerical Solution of the Steady State Reynolds Equation

The solution of the Reynolds equation is obtained in two steps. In a first step, the Reynolds equation is discretized using a finite difference scheme to obtain a discrete system of nonlinear equations for the pressure P . In a second step, the equation system is solved for the pressure distribution by means of an iterative procedure.

In order to employ the finite difference scheme, the bearing domain is divided into equal rectangular volumes with side length Δ_θ and Δ_ζ according to Figure 3.7. Assuming symmetry in respect to the bearing's center plane in axial direction at $\zeta = l_j/(2r_j)$, only half the bearing needs to be modeled. The elements are indexed with $k = 0 \dots \Theta$ in θ direction and with $i = 0 \dots Z$ in ζ direction, with $\Theta \cdot \Delta_\theta = 2\pi$ and $Z \cdot \Delta_\zeta = l_j/(2r_j)$. Using the identity

$$f \frac{\partial f}{\partial x} = \frac{1}{2} \frac{\partial f^2}{\partial x}, \quad (3.47)$$

the Reynolds equation can be written as

$$-\frac{1}{2} \frac{\partial}{\partial \theta} \left(H^3 \frac{\partial P^2}{\partial \theta} \right) - \frac{1}{2} \frac{\partial}{\partial \zeta} \left(H^3 \frac{\partial P^2}{\partial \zeta} \right) + \Lambda_j \frac{\partial(PH)}{\partial \theta} + \sigma_j \frac{\partial(PH)}{\partial \tau} = 0. \quad (3.48)$$

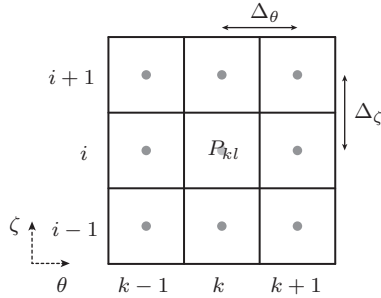


Figure 3.7: Control volume for discretization

Derivatives in the form of the Poiseuille flow terms can be approximated by a central finite difference as

$$\begin{aligned} \frac{\partial}{\partial \theta} \left(f \frac{\partial D}{\partial \theta} \right) &\approx \frac{(f_{k,i} + f_{k-1,i}) D_{k-1,i}}{2\Delta_\theta} \\ &\quad - \frac{(2f_{k,i} + f_{k+1,i} + f_{k-1,i}) D_{k,i}}{2\Delta_\theta} \\ &\quad + \frac{(f_{k+1,i} + f_{k,i}) D_{k+1,i}}{2\Delta_\theta} \end{aligned} \quad (3.49)$$

with the substitutions $f \rightarrow H^3$, $D \rightarrow P^2$ for the flow in θ direction. The Poiseuille flow in ζ direction is approximated accordingly by interchanging the subscripts k and i and replacing Δ_θ by Δ_ζ . The derivatives in the form of the Couette flow term can be approximated by

$$\begin{aligned} \frac{\partial(fD)}{\partial x} &\approx \frac{(f_{k,i} + f_{k+1,i})(D_{k,i} + D_{k+1,i})}{4\Delta_\theta} \\ &\quad - \frac{(f_{k,i} + f_{k-1,i})(D_{k,i} + D_{k-1,i})}{4\Delta_\theta} \end{aligned} \quad (3.50)$$

with the substitutions $f \rightarrow H$ and $D \rightarrow P$.

The boundary conditions are given at $\zeta = 0$ by the ambient as

$$P|_{\zeta=0} = 1 \quad (3.51)$$

and at the plane of symmetry as

$$\left. \frac{\partial P}{\partial \zeta} \right|_{\zeta=L/(2R_j)} = 0. \quad (3.52)$$

The equation system obtained from the discretization of the Reynolds equation at steady state where

$$\frac{\partial(PH)}{\partial\tau} = 0, \quad (3.53)$$

can be written in Matrix form as

$$M_P \cdot \text{diag}(P) \cdot P + M_C \cdot P + \text{diag}(V_{bnd}) \cdot P = V_{bnd}. \quad (3.54)$$

M_P contains the contributions from the finite difference approximation of the Poiseuille flow term and M_C the contributions from the Couette flow term; V_{bnd} is a vector containing ones at boundary elements to ambient and has zero entries otherwise.

In order to obtain the steady state pressure distribution P , the non-linear matrix equation (3.54) needs to be solved. This is accomplished by means of an iterative procedure starting from an initial value for the pressure distribution. A possible initial distribution is e.g. ambient pressure at all elements $P_{i=0} = 1$. The solution of the n^{th} iteration can be computed as

$$P_n = P_{n-1} + ((M_P \cdot \text{diag}(P_{n-1}) + M_C + \text{diag}(V_{bnd}))^{-1} \cdot V_{bnd} - P_{n-1}) \cdot \kappa \quad (3.55)$$

where the factor $\kappa > 0$ is used to control the convergence. Small values of κ result in slow convergence whereas larger values yield faster convergence. To large values of κ need to be avoided in order to maintain numerical stability. The iteration can be stopped when the error $|P_i - P_{i-1}|$ falls below a predefined residual value.

As an example, Figure 3.8 shows the pressure distribution obtained for a plain bearing with $r_j = 3 \text{ mm}$, $l_j = 6 \text{ mm}$ and $c = 4 \text{ }\mu\text{m}$ rotating at 500 krpm.

Numerical integration according (3.25) and (3.25) finally yields the bearing reaction force. Using the analytical solution for plain bearings from [48] which is valid for small displacements (e.g. $\varepsilon = 0.1$), the bearing force obtained from the FDM can be verified. In Figure 3.9 the nondimensional load capacity F_j of a plain bearing with $r_j = 3 \text{ mm}$, $l_j = 6 \text{ mm}$ and $c = 4 \text{ }\mu\text{m}$ computed by the FDM for speeds up to 500 krpm is compared to the analytical solution. It can be seen that for this case, the FDM results are in quite exact agreement with the analytical solution.

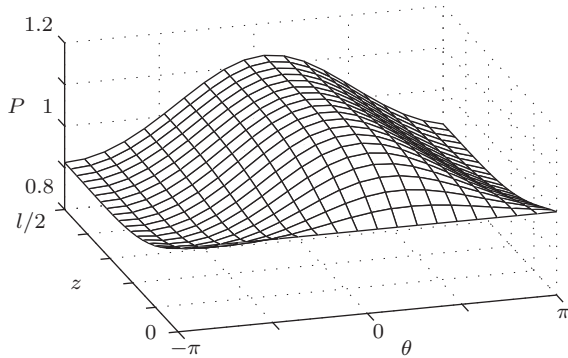


Figure 3.8: Static pressure distribution of a plain bearing with $r_j = 3 \text{ mm}$, $l_j = 6 \text{ mm}$ and $c = 4 \mu\text{m}$ at 500 krpm with $\varepsilon = 0.1$.

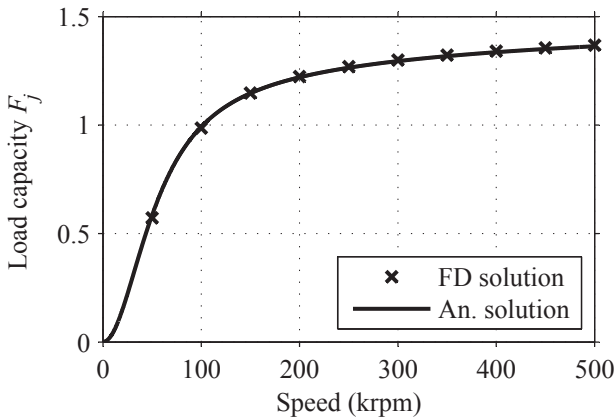


Figure 3.9: Load capacity as a function of rotational speed for a plain journal bearing with $R_j = 3 \text{ mm}$, $L_j = 6 \text{ mm}$ and $c = 4 \mu\text{m}$. Verification of finite difference calculation (crosses) with the analytical solution from [48] (solid line).

3.6.3 Bearing Transient Behavior

A commonly used method to analyze the bearing’s transient behavior is based on a frequency domain analysis using an appropriate coordinate

transform of the Reynolds equation. The method illustrates in an astonishing way the inevitability of whirl instability occurring with plain bearings. Therefore, the method is detailed in this section although it will not be used further for the calculation of gas bearings in the present thesis.

A second method based on a linearization of the Reynolds equation is presented, which will later be used to obtain a bearing model in a state-space representation or equivalently in a Laplace domain representation. The method is derived for the case of a Rayleigh step bearing, which is needed for a stability analysis of this bearing type in Section 3.8.

Frequency Response from Coordinate Transformation

Following [62] or [64], a steady whirl condition, i.e. a journal orbiting with a constant eccentricity ε at a whirl frequency ω_w is considered. For this purpose, a rotating coordinate system fixed to the orbiting journal center (θ^*, ζ) is introduced (see Figure 3.2), where

$$\theta^* = \theta - \omega_w t. \quad (3.56)$$

The local film height in the rotating coordinate system is given as

$$H = 1 - \varepsilon \cdot \cos \theta^*. \quad (3.57)$$

Considering

$$\frac{\partial}{\partial \theta} = \frac{\partial}{\partial \theta^*} \quad (3.58)$$

and

$$\frac{\partial(PH)}{\partial t} = -\frac{\partial(PH)}{\partial \theta^*} \cdot \omega_w, \quad (3.59)$$

the Reynolds equation for the plain bearing (3.14) is rewritten in rotating coordinates as

$$-\frac{\partial}{\partial \theta^*} \left(PH^3 \frac{\partial P}{\partial \theta^*} \right) - \frac{\partial}{\partial \zeta} \left(PH^3 \frac{\partial P}{\partial \zeta} \right) + \Lambda_j^* \frac{\partial(PH)}{\partial \theta^*} = 0 \quad (3.60)$$

with

$$\Lambda_j^* = \frac{6\eta r_j^2 (\Omega - 2\omega_w)}{p_a c^2}. \quad (3.61)$$

It is noted that after the coordinate transformation, the obtained equation (3.60) is free from the time derivative $\frac{\partial}{\partial \tau}$. Solving for the pressure distribution depending on the whirl frequency ω_w and integrating according (3.25) and (3.27) to obtain the bearing force, finally yields the bearing frequency response $F_j(\omega_w)$. An LTI model in state space representation with the state vector ξ_j and the system matrices A_j , B_j , C_j and D_j can then be obtained in the form

$$\begin{aligned}\dot{\xi}_j &= A_j \xi_j + B_j \epsilon \\ f_j &= C_j \xi_j + D_j \epsilon\end{aligned}\tag{3.62}$$

using a frequency domain model identification method according [67]³.

It is seen, that for $\omega_w = \Omega/2$ the bearing number is $\Lambda_j^* = 0$. The pressure in the fluid film is then equal to the ambient pressure and the bearing loses its load capacity [42]. The phenomenon is known as the half frequency whirl of plain journal bearings which is the very limiting factor for the practical use of plain journal bearings. It is therefore that axial grooving has been introduced in Rayleigh step bearings or lobed bearings to interrupt the pressure profile and enable superior stability.

The coordinate transform method can also be applied to herringbone grooved journal bearings where the pressure along a groove-ridge pair can be approximated by its average pressure [64]. Due to the inward pumping grooves, the herringbone grooved bearing has no condition where load capacity is lost and therefore, stability of this bearing type is much improved [64].

Perturbation and and Model Order Reduction

For a Rayleigh step journal bearing, a perturbation method can be applied when a larger number of steps N_{step} on the circumferential of the bearing is used. With a large number of steps and small journal displacements, the curvature of the bearing becomes small across a single step/pad and the fluid film between the journal and the bushing can be approximated by parallel planes, see Figure 3.10. In this case, it is sufficient to compute the pressure distribution and the dynamic properties of a single step and in the end account for the remaining steps by an appropriate superposition considering their relative orientation.

³An implementation of the model identification algorithm is provided in the model identification toolbox in MATLAB

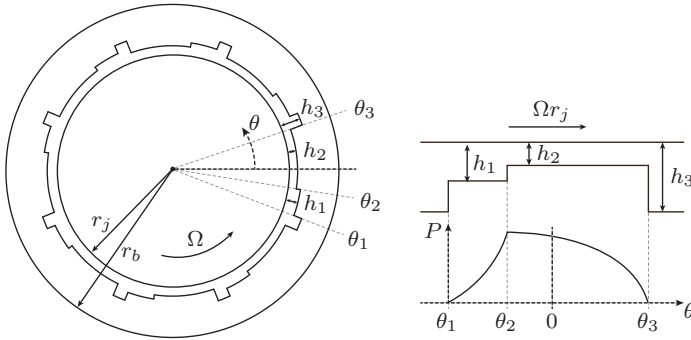


Figure 3.10: Rayleigh step journal bearing, parameter and coordinate system definition, not drawn to scale (left). Planar approximation of a single step and qualitative pressure distribution (right).

For the Rayleigh step bearing, the nominal local film height is given as a function of the circumferential coordinate θ as

$$h_0(\theta) = \begin{cases} h_1 & \text{for } \theta_1 < \theta < \theta_2 \\ h_2 & \text{for } \theta_2 < \theta < \theta_3 \end{cases} \quad (3.63)$$

where θ_1 and θ_2 denote the step locations as visualized in Figure 3.10. The deep groove with depth h_3 is not incorporated in the lubrication domain under analysis. It is assumed that h_3 is chosen to guarantee ambient pressure along the groove for the full operating range. Under rotation, a pressure is then generated by the fluid squeezed into the converging step profile as visualized.

In a first step, the steady state pressure P_0 is obtained by solving the stationary Reynolds equation (3.48) with $\frac{\partial(PH)}{\partial T} = 0$ according to the FDM procedure given in Section 3.6.2. The boundary conditions imposed by the deep groove at ambient pressure are

$$P|_{\theta=\theta_1} = P|_{\theta=\theta_3} = 1. \quad (3.64)$$

In a second step, to calculate the dynamic behavior of the fluid film, the film height is assumed a function of the varying displacement described as

$$h = h_0 + \epsilon \quad (3.65)$$

or equivalently in the dimensionless notation

$$H = h/h_2 = H_0 + \varepsilon. \quad (3.66)$$

The varying film height will result in a pressure variation which is denoted as δP . Assuming $\varepsilon \ll 1$, the pressure variation can be approximated as

$$\delta P = \frac{\partial P}{\partial \varepsilon} \cdot \varepsilon. \quad (3.67)$$

A partial differential equation for δP can be obtained by a linearization of the unsteady Reynolds equation (3.48). Linearization around the centered operating point at zero displacement $\varepsilon = 0$ and the corresponding pressure P_0 by means of the operator

$$\varepsilon \cdot \frac{\partial}{\partial \varepsilon} \Big|_{\varepsilon=0} \quad (3.68)$$

yields the linear partial differential equation for δP as

$$\begin{aligned} & -\frac{\partial}{\partial \theta} \left(H_0^3 P_0 \frac{\partial \delta P}{\partial \theta} + H_0^3 \delta P \frac{\partial P_0}{\partial \theta} + \varepsilon \cdot \frac{\partial H^3}{\partial \varepsilon} \Big|_{\varepsilon=0} \cdot P_0 \frac{\partial P_0}{\partial \theta} \right) \\ & -\frac{\partial}{\partial \zeta} \left(H_0^3 P_0 \frac{\partial \delta P}{\partial \zeta} + H_0^3 \delta P \frac{\partial P_0}{\partial \zeta} + \varepsilon \cdot \frac{\partial H^3}{\partial \varepsilon} \Big|_{\varepsilon=0} \cdot P_0 \frac{\partial P_0}{\partial \zeta} \right) \\ & + \Lambda_j \frac{\partial}{\partial \theta} \left(H_0 \delta P + \varepsilon \cdot \frac{\partial H}{\partial \varepsilon} \Big|_{\varepsilon=0} \cdot P_0 \right) \\ & + \sigma_j \frac{\partial}{\partial \tau} \left(H_0 \delta P + \varepsilon \cdot \frac{\partial H}{\partial \varepsilon} \Big|_{\varepsilon=0} \cdot P_0 \right) = 0. \end{aligned} \quad (3.69)$$

The bearing force f_{step} generated by a single step is obtained by integration of δP according (3.25) and (3.27) over the lubrication domain of the single step under analysis. The total bearing force considering the contribution of all N_{step} steps of the bearing is then given as

$$f_j = f_{step} \cdot \sum_{k=0}^{k=N_{step}} \cos \left(\frac{2\pi k}{N_{step}} \right) \cdot e^{j \frac{2\pi k}{N_{step}}} = \frac{N_{step} \cdot f_{step}}{2}. \quad (3.70)$$

Discretizing the partial differential equation (3.69) using the finite difference approximation for the derivatives (3.49) and (3.50), yields a linear equation system for δP which can be written in state space

representation by means of the system matrices A'_j , B'_j and C'_j as

$$\begin{aligned}\delta\dot{P} &= A'_j \cdot \delta P + B'_j \cdot \begin{bmatrix} \epsilon \\ \dot{\epsilon} \end{bmatrix} \\ f_j &= C'_j \cdot \delta P.\end{aligned}\tag{3.71}$$

The matrices A'_j , B'_j and C'_j resulting from the discretization procedure are generally very large as the vector δP can contain several hundreds of unknowns. Stability and rotor dynamic analysis will therefore be computationally inefficient and a model order reduction to a state space representation with fewer states is recommended. A reduced order approximation of the model can be computed using the balanced order reduction method described in [68]⁴. It is found that two states are usually already sufficient to represent the original system with high accuracy at the frequencies of interest which range from zero to a few tens of kilohertz.

When comparing the state space representation of (3.71) to the state space representation given in (3.62) one notices that the direct input to output transfer matrix D_j is not present in the description obtained from the perturbation analysis. The direct coupling to the system output is hidden in the time derivative of the system input $\dot{\epsilon}$. Hence a nonzero transfer matrix D_j will be always obtained when transforming the system description from the perturbation analysis into the general state space representation of the form (3.62).

The dynamic bearing stiffness in a Laplace domain representation is given by transforming (3.71) into the Laplace domain and solving for $f_j/\epsilon = c_j(s)$ as

$$c_j(s) = C'_j(sI - A'_j)^{-1} \cdot B'_j \cdot \begin{bmatrix} 1 \\ s \end{bmatrix}.\tag{3.72}$$

Due to the complex definition of the bearing force f_j given in Section 3.3, the transfer function $c_j(s)$ has complex coefficients in its numerator and denominator and therefore, poles and zeros will not occur in complex conjugated pairs as one is used with real representations of Laplace domain transfer functions.

⁴An implementation thereof is provided in MATLAB

3.7 Dynamic Stability

Cross coupling forces embodied by the bearing's attitude angle and high inertial loading have a major impact on the dynamic stability of gas bearings. Thus, based on a simplified bearing-mass model, the influence of the bearing's attitude angle and the supported mass together with the ability of a damping force to enable stability is analyzed. Subsequently, means for improving the stability of gas bearings are reviewed and discussed.

3.7.1 Attitude Angle and Damping

For a simplified stability analysis, the dynamic system consisting of a gas bearing supporting a concentrated mass m is considered. The system has two degrees of freedom, namely translational motion in x and y direction, represented by the real and imaginary part of the displacement ϵ . The bearing-mass system can be described by the differential equation

$$m\ddot{\epsilon} = c_j \cdot \epsilon + f_\delta \quad (3.73)$$

where f_δ denotes an arbitrary disturbance force and c_j is the dynamic bearing stiffness of the bearing. In Laplace domain, the transfer function from the disturbance force to the displacement is then written as

$$\frac{\epsilon}{f_\delta} = \frac{1}{ms^2 - c_j(s)}. \quad (3.74)$$

Stability of the considered system can be determined by consulting the poles of the above transfer function. If the system exhibits only poles in the left half of the complex plane (LHP), the system is known to be stable. Otherwise, if a pole in the right half plane (RHP) exists, the system behaves unstable.

As a simplification, the bearing stiffness is assumed

$$c_j = -c_s e^{j\phi} - d \cdot s, \quad (3.75)$$

where $c_s e^{j\phi}$ denotes a static bearing stiffness with attitude angle ϕ , i.e. $c_s e^{j\phi}$ contains a restoring component $c_s \cos(\phi)$ and a cross coupling component $c_s \sin(\phi)$. The factor d is the damping factor which yields a force proportional to the velocity. Then, the poles are given by the roots of the system's characteristic polynomial

$$ms^2 + ds + c_s e^{j\phi} = 0 \quad (3.76)$$

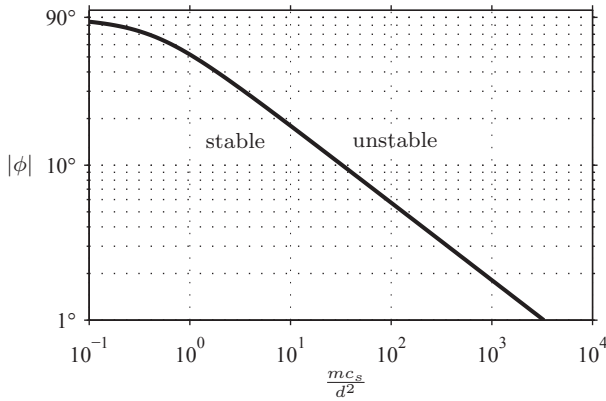


Figure 3.11: Stability limit for the bearing attitude angle ϕ depending on the supported mass m , static bearing stiffness c_s and the damping factor d .

which are

$$p = \frac{-d \pm \sqrt{d^2 - 4mc_s e^{j\phi}}}{2m}. \quad (3.77)$$

Stability is given if $\Re\{p\} < 0$ which implies that the inequality

$$\Re \left\{ \sqrt{1 - \frac{4mc_s e^{j\phi}}{d^2}} \right\} < 1 \quad (3.78)$$

must hold.

The above inequality can be solved numerically for the maximum allowable attitude angle ϕ given a supported mass m , static stiffness c_s and damping ratio d . The obtained result is plotted in Figure 3.11. Attitude angles larger than the indicated line result in unstable systems while smaller attitude angles yield stability. On the line, the system is boundary stable. For small values of $\frac{mc_s}{d^2}$, the attitude angle ϕ which still yields stability approaches 90° while for large values of $\frac{mc_s}{d^2}$, ϕ needs to be gradually decreased.

It can be seen that for a heavier supported mass m , stability is harder to achieve and a smaller attitude angle or a larger damping ratio may be required. A bearing with zero attitude angle will be stable

for any supported mass. It can be concluded that theoretically, a bearing with a positive restoring stiffness and any amount of cross coupling stiffness can be stabilized by providing a large enough amount of damping force. Thus, either by an increase of damping from within the fluid film or also from external damping system, the bearing's stability can always be improved.

3.7.2 Critical Mass

In this section, the bearing-mass system with the transfer function (3.74) is reconsidered. Now, the dynamic bearing stiffness $c_j(s)$ is assumed a complex transfer function in the Laplace variable s representing the dynamic behavior of the gas bearing. Pleading to the governing Reynolds equation, $c_j(s)$ itself must be stable. It is assumed that $c_j(s)$ has only LHP zeros. Considering the transfer function of the bearing-mass system (3.74) for a very small supported mass, the poles of the bearing-mass system become the zeros of the dynamic stiffness and with the assumption of LHP zeros only, the bearing-mass system will be stable. Increasing the mass will usually shift the poles toward the imaginary axis and finally into the RHP.

As a measure of stability of a gas bearing, the critical mass m_{crit} is defined as the maximum supported mass such that the bearing-mass system is still stable, i.e. the system operates in a boundary stable condition. A pole then exists on the imaginary axis $p = j\omega_w$ such that the denominator of (3.74) vanishes at the whirl frequency ω_w which yields the condition for the critical mass

$$m_{crit}\omega_w^2 + c_j(j\omega_w) = 0. \quad (3.79)$$

Splitting into real and imaginary part gives

$$\Im\{c_j(j\omega_w)\} = 0 \quad (3.80)$$

$$-\Re\{c_j(j\omega_w)\} = m_{crit}\omega_w^2, \quad (3.81)$$

which needs to be solved for ω_w and m_{crit} .

The critical mass gives a trend of the bearing for a stably supported rotor mass. Because of its simplicity and independence of a final rotor system, it can be used to compare different gas bearing designs or gas bearing types, or it can serve as an objective parameter in a bearing stability optimization. Because of the underlying simplified bearing-mass model, stability of a rotor supported by a set of gas-bearings

however needs finally be determined with a particular rotor dynamic model.

3.7.3 Means for Stability Improvement

Down-Scaling of the Gas Bearing Clearance

As seen in Section 3.2, stability can be increased by reducing the bearing clearance. According to [51] the damping ratio from the fluid film scales inversely proportional to the third power of the gas bearing clearance. Hence, a significant increase of stability can be expected with a reduced bearing clearance. However, the increase in damping is traded for an increase in friction losses which with the reduced clearance worsens the ability to cope with thermal and centrifugal expansion and the related thermal instability as discussed in Section 3.5. Another major limitation of the clearance downs-scaling is imposed by bearing fabrication, when the required bearing clearance is specified to only a few micrometers which then is in the same order of magnitude as high-precision production tolerances.

Minimization of Attitude Angle

The poor dynamic stability of the plain bearing spurred the invention of a variety of different bearing types. For the bearing types with a fixed geometry such as the herringbone grooved, the Rayleigh step or the lobed bearings the improvement in stability can be attributed to a decrease of the attitude angle due to the special geometric features of the bearings.

With the use of steps or lobes, the typical pressure profile encountered with plain bearings which leads to attitude angles approaching 90° is interrupted by the introduction of axial grooves. At the locations of the grooves, the pressure is equal to the ambient and is therewith independent of the bearings lubrication regime. Hence, lubrication surfaces located between the grooves act independent. Considering only the normal force exerted by the resulting pressure distribution of an individual surface or pad and neglecting the shear force which is usually minor, the attitude angle cannot be larger than the coverage angle of the pad. As the coverage angle of a pad is bound to the number of pads, an augmentation of pads/axial grooves reduces the attitude angle.

For the herringbone grooved bearing, the reduction of attitude angle comes with the introduction of inward pumping grooves. The grooves are acting as a viscous pump increasing the fluid pressure. As a consequence, the attitude angle can be controlled by choice of the groove parameters [64].

External Damping and Active Control

Even when the gas bearing is optimized for minimum attitude angle and maximum damping given by a clearance defined by producibility and robustness against rotor growth, stability might be insufficient for operation at high rotational speeds. In Section 3.7.2 it was shown for the case of a bearing-mass system, that stability can always be achieved when the amount of damping is sufficiently high. Thus, the introduction of external damping, i.e. from outside the fluid film can be considered to achieve stability. Several possibilities exist to add damping to the gas bearing system.

Compliant structures are used in foil bearings where dry friction between the top foil and the bump foil is thought to provide structural damping. The bushing surface is formed by the foil and can yield to and absorb journal motion. Guidelines how to design optimal foil bearings are presented in [66].

In [69], so-called active gas bearings, i.e. tiling pad bearings with built-in piezoelectric actuators, are employed for controlling of the bearing's self-excited whirl instability.

External damping by means of an elastic bearing support in combination with a tunable squeeze film damper has been demonstrated in [28]. The elastic support is realized with elastomeric O-rings. Damping forces are transferred via the bearing journal to the rotor, i.e. the damper forces act serially to the gas bearing forces as depicted in Figure 3.12 (a). A careful design is needed to match the stiffness of the elastic support c_d , the strength squeeze film damper d , the mass of the bearing bushing m_b to the gas bearing dynamics c_j in order to obtain optimal performance [28].

Figure 3.12 (b) shows a damper configuration where the damping force is exerted directly on the rotor, i.e. parallel to the gas bearing forces. The advantage of this approach is that no tuning of an elastic support is required and the mass of the bearing bushing does not need to be accounted for in a design. To apply such a force, a contactless damper principle is needed which can be an AMB or AMD as is the

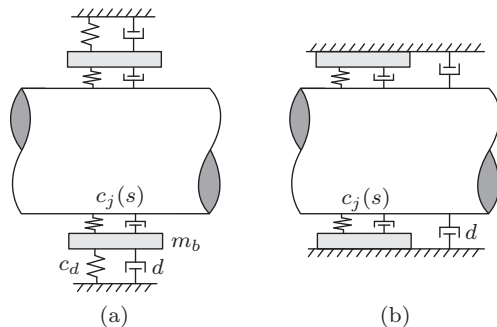


Figure 3.12: Introduction of external damping: indirect/serial damping via the bearing bushing (a), direct/parallel damping (b).

focus of the present thesis. Passive magnetic dampers based on eddy current damping may be another option. Possible magnetic damper strategies are discussed in Section 4.2.

Only little work has been reported in the field of stabilization of fluid film bearings by means of AMBs or AMDs. To the author's knowledge, open literature reports only stabilization of oil bearings [70, 71, 72]. Related to gas bearings, [73] reports on a hybrid foil-magnetic bearing which however is designed to improve the bearings load capacity at low speeds, which is not the scope of the present thesis.

In [70] three different control schemes have been studied for the control of oil whirl and whip instabilities, which are a position controller, an acceleration controller and a damping controller, i.e. a controller applying a force proportional to the translational velocity. In the referred work, the best performance was obtained with the damping controller.

3.8 Rayleigh Step Bearing Design

For a prototype machine design, a Rayleigh step journal bearing is employed (see Section 6.2.1). As already mentioned, the attitude angle can be controlled within certain limits by the choice of the number of steps. The angle contribution from the pressure distribution across a single step can be no greater than the span angle $\theta_3 - \theta_1$ of the step. Hence in respect to the attitude angle, the number of steps should be chosen large.

Quantity	Symbol	Value/Range	step size
Min. film height	h_2	4...15 μm	1 μm
Step height	$\delta_h = h_1 - h_2$	1...15 μm	1 μm
Rel. step location	g	0.05...0.9	0.023
Radius	R_j	3 mm	
Speed	Ω	500 krpm	

Table 3.2: Grid search optimization parameters for Rayleigh step journal bearing.

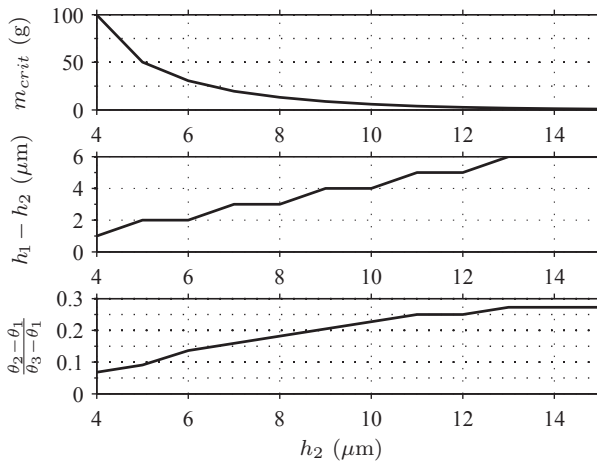


Figure 3.13: Stability optimization results of a Rayleigh step journal bearing with $R_j = 3$ mm at a speed of 500 krpm.

However, load capacity will be decreased with the number of steps increasing as a result of the deep groove h_3 which is not contributing a bearing force but will have a minimal extent for fabrication reasons. In a design, the number of steps needs therefore chosen in a trade-off.

Optimization for Stability

For the prototype machine design presented in Section 6.2.1, the number of steps is chosen $N_{step} = 8$. In order to determine the step location θ_2 and the clearances h_1 and h_2 , a parametric grid search optimization in

respect to the bearing's critical mass parameter is performed. The optimization is based on the numerical methods presented in Section 3.6. The parameter definition of the Rayleigh step bearing is given in Figure 3.10. The optimization parameters are the step height $h_1 - h_2$, the relative step location $\frac{\theta_2 - \theta_1}{\theta_3 - \theta_1}$ and the concentric minimum film height h_2 . The range of the parameters with the used discretization steps is given in Table 3.2. The optimization was conducted for a bearing with a radius of $R_j = 3$ mm at a speed of 500 krpm.

Figure 3.13 shows the maximum achievable critical mass m_{crit} depending on the minimum film height h_2 , together with the according optimum step height $h_1 - h_2$ and the optimum step location $\frac{\theta_2 - \theta_1}{\theta_3 - \theta_1}$. As expected, m_{crit} decreases rapidly with h_2 increasing. For the prototype design, a minimum film height of $h_2 = 8 \mu\text{m}$ is chosen as a tradeoff between stability and manufacturing accuracy requirements.

Figure 3.14 shows the critical mass m_{crit} as a function of the step height $h_2 - h_1$ and the relative step position $\frac{\theta_2 - \theta_1}{\theta_3 - \theta_1}$ for $h_2 = 8 \mu\text{m}$. For a maximum critical mass, the relative step location would be $\frac{\theta_2 - \theta_1}{\theta_3 - \theta_1} \approx 0.18$ and the step height $h_2 - h_1 = 3 \mu\text{m}$. However, as the critical mass is decreasing rapidly towards smaller steps heights, which imposes a risk with the given production tolerances, the nominal step is chosen $h_2 - h_1 = 5 \mu\text{m}$.

The dynamic stiffness $c_j(s)$ for the resulting bearing design is given in the bode diagram of Figure 3.15 for speeds of 100 krpm to 500 krpm. In Chapter 5, the dynamic stiffness $c_j(s)$ of the bearing will be used for a rotor dynamic stability analysis.

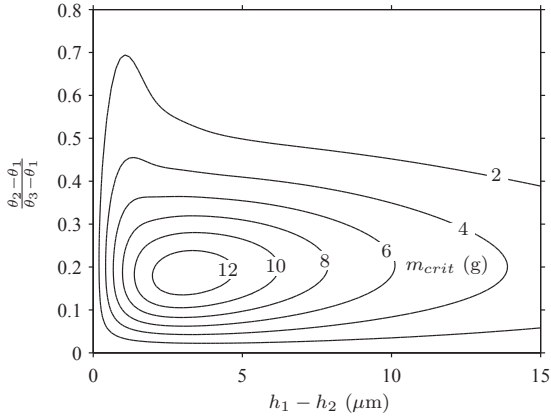


Figure 3.14: Critical mass m_{crit} as a function of the step height $h_2 - h_1$ and the relative step position $\frac{\theta_2 - \theta_1}{\theta_3 - \theta_1}$ for a bearing clearance of $h_2 = 8 \mu\text{m}$

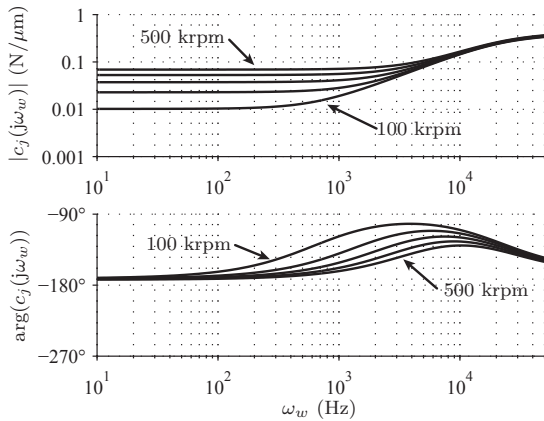


Figure 3.15: Frequency response $c_j(j\omega_w)$ of the final Rayleigh step bearing design for speeds of 100 krpm, 200 krpm, 300 krpm, 400 krpm and 500 krpm

Chapter 4

Active Magnetic Damper

For the stabilization of a rotor supported by gas bearings at high rotational speeds, different damper concepts may be applied. With a focus on a self-sensing displacement measurement approach in order to obtain a compact system, electro-magnetic models for the magnetic damper actuators are derived and back-EMF based and signal-injection based damper concepts are studied. Comparing the different approaches, a concept employing a heteropolar magnetic damper actuator integrated into the active region of the permanent magnet machine is elaborated, and a new eddy current based self-sensing signal-injection displacement measurement technique is proposed.

4.1 Electro-Magnetic Modeling

AMDs differ from AMBs mostly in the designated purpose. Apart from the applied control laws the technical implementation of a magnetic damper can be identical to its magnetic bearing counterpart. While AMBs are typically intended to control the absolute position of an object and provide static and dynamic load and stiffness, an AMD may only provide dynamic forces in order to reduce e.g. vibration in a system. The implementation of AMD and AMB actuators is therefore similar and actuator concepts originally developed for AMBs can be directly applied to AMDs.

AMBs can be divided into two categories regarding their magnetic configuration, namely into heteropolar and homopolar bearing types.

The term heteropolar refers to a bearing configuration where the polarity of the stator winding or the rotor is exposed to magnetic field with alternating polarity under rotation [21]. With homopolar bearing types, the polarity is not changing under rotation.

For ultra-high-speed machines, it was found that a slotless machine design is beneficial [1]. Losses are minimized by the use of a slotless rather than a slotted stator in order to avoid slot harmonic induced losses. With the choice of an air gap winding made from litz wire and the use of amorphous iron for the stator yoke, the losses at high speeds are further reduced. The rotor consists of a cylindrical permanent magnet encased in a metallic retaining sleeve to cope with the high centrifugal stresses resulting at high rotational speeds [1].

Based on the well proven slotless machine concept it seems self-evident to apply the slotless concept to a high speed AMB or AMD design. In a recent achievement, ultra-high-speed operation of such a Lorentz force based magnetic bearing has been demonstrated to speeds up to 505 krpm [6].

A major advantage of the slotless concept is the low negative stiffness added to the rotor bearing system due to the relatively large magnetic air gap. Also due to the large magnetic air-gap, the self-inductance of the bearing coils is relatively small and therefore, only low reactive power needs to be spent even for heteropolar types at high rotational speeds. Furthermore as armature reaction is small due to the large magnetic air-gap, saturation effects in the stator back-iron can be easily avoided in a design. Therefore, the force to current relationship can be expected a linear function of currents in a wide operating range. If necessary for stabilization of the rotor, short current peaks can be tolerated if they are in accordance with the thermal limitations of the machine design. The only drawback of the slotless design is its relatively low force density compared to common reluctance type realizations.

Slotless type bearings can be built in both a homopolar and a heteropolar configuration. In the following, analytic magnetic models are given for the two realizations.

4.1.1 Slotless Homopolar Damper Winding

In order to study the basic control laws for the homopolar damper, the relationship between generated force, damper terminal voltage and current are needed. For this purpose, a simplified model of the damper is

considered. A schematic view of a possible realization of a homopolar magnetic damper is depicted in Figure 4.1. With a permanent magnet on the rotor which is magnetized in radial direction to produce a homopolar magnetic field, a set of two conductors arranged on the x axis yield a Lorentz force in y direction and another set of two conductors arranged in the y axis are used to produce a Lorentz force in x direction. Forces exerted on the rotor are perceived as reaction forces corresponding to the generated Lorentz forces in the winding.

Assuming a permeability $\mu = \mu_0$ for the whole actuator domain, and neglecting armature reaction, the damper force resulting from a current i in a conductor can be written for an centered rotor as the Lorentz force

$$f_d = B \cdot l_d \cdot i = \Psi i, \quad (4.1)$$

where l_d is the length of the conductor in the magnetic field B and $\Psi = B \cdot l_d$ denotes the flux linkage. From energy conservation it follows that the electrical power converted to mechanical power must be equal, hence

$$u_{ind} \cdot i = f_d \cdot \dot{\epsilon}, \quad (4.2)$$

where $\dot{\epsilon}$ denotes the translational velocity of the rotor. The voltage across the conductor is composed of the induced voltage u_{ind} and an inductive and a resistive voltage drop. Combining (4.1) and (4.2) to obtain u_{ind} , the conductor terminal voltage can then be written as

$$u = \Psi \cdot \dot{\epsilon} + L\dot{i} + Ri, \quad (4.3)$$

where L denotes the actuators self-inductance and R is its resistance.

For a magnetic bearing or damper, the flux linkage definition differs from the definition encountered in rotating machines. There, the flux linkage is in the unit volt seconds (Vs) whereas for magnetic bearings/dampers considered here, the flux linkage takes the units volt seconds per meter (Vs/m), which is the same definition as for linear motors.

It is noted that the terminal voltage depends on the rotor velocity. Hence for a control law with damping forces proportional to the velocity, a self-sensing technique based on the actuators back-emf voltage seems applicable. Control strategies based on the above equation are detailed in Section 4.2.1.

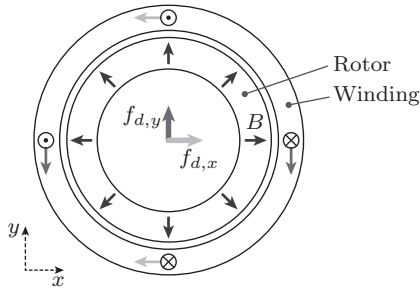


Figure 4.1: Homopolar slotless AMB/AMD topology.

4.1.2 Slotless Heteropolar Damper Winding

When using a permanent magnet rotor with a pole pair number p_r , a force can be generated when using a pole pair number $p_s = p_r \pm 1$ on the stator winding. With such a heteropolar damper, the choice of $p_r = 1$ suggests itself as also the permanent magnet machine will be designed with a single pole pair on the rotor and therewith the machine and the damper can be combined using the same permanent magnet as proposed in the self-bearing AMB machine design in [40, 6]. Hence with $p_r = 1$, the damper winding will have $p_s = 2$; p_s equal to zero cannot exist. The damper winding can then be arranged on the innermost radius defined by the rotor radius and the required mechanical air-gap. The machine winding is arranged between the outer diameter of the damper winding and the inner diameter of the stator back-iron. A cross section view of the arrangement is shown in Figure 4.2.

Under the assumption of a linear relation between force and current which will later be confirmed, the damper forces can be written as

$$f_{d,y} = \Psi \cdot i_d \quad (4.4)$$

$$f_{d,x} = \Psi \cdot i_q, \quad (4.5)$$

where Ψ is the flux linkage and i_d and i_q denote the field oriented stator currents referenced to the rotational position of the rotor, i.e. the d and q current components. As a result from the following analysis of the AMD winding, it is found that the flux linkage is direction independent, i.e. Ψ is unchanged for d and q direction. Unlike dq coordinates in permanent synchronous machines, where the coordinates

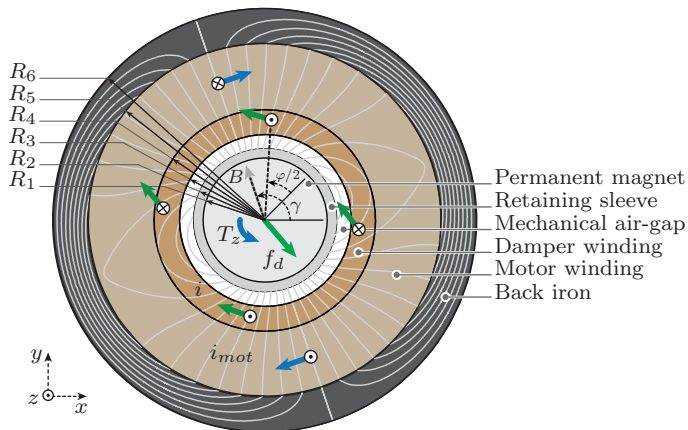


Figure 4.2: Heteropolar slotless AMD winding integrated into active region of the permanent magnet machine. The damper winding is used to generate a resultant force f_d on the rotor while the motor winding produces a force couple resulting in a torque T_z .

refer to fixed locations on the rotor, the dq coordinates introduced here cannot be attached to a rotor location. For each rotor position, the effective direction of the d and q axis is changed.

In the following, analytical expressions for the flux linkage Ψ and the phase terminal voltages will be derived. For this purpose, a straight winding with $m = 2$ phases and $p_s = 2$ is considered, which is, as will result from Section 4.3 the preferred choice of winding in a displacement self-sensing configuration. When neglecting end winding effects and assuming a vanishing component in axial direction of the magnetic field, i.e. $B_z = 0$, a two-dimensional magnetostatic problem formulation can be applied.

The magnetic forces will be calculated using two different approaches. In a first approach, the forces are calculated from the Lorentz force density integrated over the winding volume. This yields a simplified solution as reluctance forces, which are present due to the stator back iron and the armature field, are neglected. In a second approach, the armature field is calculated the magnetic forces are analytically derived by means of the Maxwell stress tensor.

Lorentz Force Integration

Neglecting armature reaction and reluctance forces resulting from the stator back iron, the magnetic forces can be approximated by integrating the Lorentz force density over the winding volume V as

$$f_d = \int_V J \times B_{pm} \cdot dV, \quad (4.6)$$

where J denotes the current density in the winding and B_{pm} is the magnetic field caused by the permanent magnet in the rotor. The phase currents are described by means of a current space vector

$$i = \hat{I} \cdot e^{j\varphi} \quad (4.7)$$

where \hat{I} is its amplitude and φ its phase. The corresponding currents in the two phases A and B are

$$i_a = \hat{I} \cdot \cos(\varphi) \quad (4.8)$$

$$i_b = \hat{I} \cdot \sin(\varphi). \quad (4.9)$$

The amplitude of the current density in the winding is then given as

$$\hat{j} = \frac{8N \cdot \hat{I}}{\pi(R_4^2 - R_3^2)} \quad (4.10)$$

where N is the turn number per phase belt and R_3 and R_4 are the damper winding's inner and outer radii.

The spatial current density distribution can be described as

$$J = \begin{cases} \hat{J} \cdot \cos(\varphi) & \text{for } A^+ \\ -\hat{J} \cdot \cos(\varphi) & \text{for } A^- \\ \hat{J} \cdot \sin(\varphi) & \text{for } B^+ \\ -\hat{J} \cdot \sin(\varphi) & \text{for } B^- \end{cases} \quad (4.11)$$

where A^+ , A^- , B^+ and B^- refer to the phase belt definitions given in Figure 4.3.

An analytical solution of the magnetic field caused by the diametrically magnetized permanent magnet in a slotless machine design is given in [74]. Due to the rotational symmetry of the machine geometry,

the field can be described in cylindrical coordinates (r, θ) . The field components in radial and azimuthal directions can be written as

$$B_r = \hat{B}_r(r) \cdot \cos(\theta - \gamma) \quad (4.12)$$

$$B_\theta = \hat{B}_\theta(r) \cdot \sin(\theta - \gamma) \quad (4.13)$$

where γ describes the angular rotor orientation. Under the assumption of the relative permeability in the permanent magnet $\mu_{r,pm} \approx 1$ and the permeability of the stator back iron $\mu_{r,Fe} \rightarrow \infty$, the radial dependency of the magnetic field can be written as

$$\hat{B}_r(r) = \frac{B_{rem} R_1^2}{2R_5^2} \left(\frac{R_5^2}{r^2} + 1 \right) \quad (4.14)$$

$$\hat{B}_\theta(r) = \frac{B_{rem} R_1^2}{2R_5^2} \left(\frac{R_5^2}{r^2} - 1 \right), \quad (4.15)$$

where B_{rem} denotes the remanent flux density of the permanent magnet and R_1 and R_5 denote the permanent magnet and the iron inner radii respectively. Evaluating the Lorentz force density and integrating over the winding domain according (4.6) yields the damper forces as

$$\begin{bmatrix} f_{d,x} \\ f_{d,y} \end{bmatrix} = \hat{I} \cdot \Psi_{lrtz} \begin{bmatrix} \cos(\varphi - \gamma) \\ \sin(\varphi - \gamma) \end{bmatrix} \quad (4.16)$$

with the flux linkage

$$\Psi_{lrtz} = \frac{8\sqrt{2}Nl_d R_1^2 B_{rem}}{\pi(R_4^2 - R_3^2)} \cdot \log\left(\frac{R_4}{R_3}\right), \quad (4.17)$$

where l_d denotes the active length of the magnetic damper.

It is noted, that (4.16) is independent of the iron inner radius R_5 . The reason therefor is the fact that the damper winding utilizes both the radial and azimuthal permanent magnet flux which sum is independent of the iron inner radius R_5 .

In the rotating frame, the stator space vector current can be defined as

$$i_{dq} = \hat{I} \cdot e^{j(\varphi - \gamma)}. \quad (4.18)$$

With the definition of the magnetic damper force in a complex representation

$$f_d = f_{d,x} + jf_{d,y}, \quad (4.19)$$

the (4.16) can be written in the form

$$f_d = \Psi_{lrtz} \cdot i_{dq}. \quad (4.20)$$

Armature Flux

The governing equation for the armature flux is given by the Poisson's equation

$$\nabla^2 A = -J, \quad (4.21)$$

where A is the vector potential which for the present two dimensional analysis can be written with only a z component as $A = [0, 0, A_z]$. The vector potential is defined such that

$$H_s = \nabla \times A, \quad (4.22)$$

where H_s denotes the magnetic field caused by the winding current. The Poisson's equation can be solved analytically for the present two-dimensional slotless machine layout by means of the standard approach of representing the unknown function by Fourier series. Hence for each harmonic order k , $\nabla^2 A_k = -J_k$ needs to be solved and to obtain a solution for $H_{s,k}$. The total field is then given by the superposition

$$H_s = \sum_{k=1}^{k=\infty} H_{s,k}. \quad (4.23)$$

The vector potential must be defined in the three regions I , II and III according to Figure 4.3. For $k = 1$, a different general solution to the Poisson's equation (4.21) must be used than for $k > 1$ [75]. For $k = 1$ the solution takes the form

$$A_I = a_{11} r^2 \sin(p_s \theta) \quad (4.24)$$

$$A_{II} = \left(a_{21} r^2 + \frac{a_{22}}{r^2} - \frac{r^2 J_2 \log(r)}{4} \right) \sin(p_s \theta) \quad (4.25)$$

$$A_{III} = \left(a_{31} r^2 + \frac{a_{32}}{r^2} \right) \sin(p_s \theta). \quad (4.26)$$

For $k > 1$ the solution is

$$A_I = a_{11} r^{kp_s} \sin(kp_s \theta) \quad (4.27)$$

$$A_{II} = \left(a_{21} r^{kp_s} + a_{22} r^{-kp_s} - \frac{r^2 J_k}{k^2 p_s^2 - 4} \right) \sin(kp_s \theta) \quad (4.28)$$

$$A_{III} = \left(a_{31} r^{kp_s} + a_{32} r^{-kp_s} \right) \sin(kp_s \theta), \quad (4.29)$$

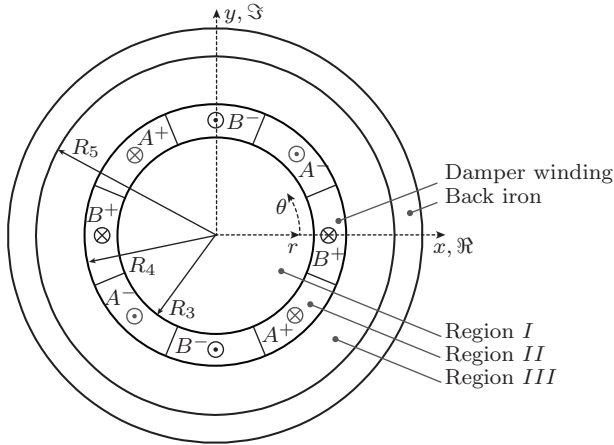


Figure 4.3: Coordinate system and region definition for magnetic damper's armature magnetic field calculation.

where the constants a_{11} to a_{32} need to be determined from the continuity conditions on the internal interfaces and the boundary condition. The continuity conditions are

$$H_s|_{r=R_3} = H_s|_{r=R_3} \quad \text{and} \quad H_s|_{r=R_4} = H_s|_{r=R_4} \quad (4.30)$$

and the boundary condition to the stator back iron is given by the assumption of infinite permeability of the iron. Thus the magnetic field enters the iron perpendicularly. The boundary condition is therefore formulated as

$$H_{s\theta}|_{r=R_5} = 0 \quad (4.31)$$

The solution for the winding field for a winding with $R_3 = 3.25\text{mm}$, $R_4 = 3.75\text{mm}$ and $R_5 = 6\text{mm}$ is depicted in Figure 4.4. In the analytical result, harmonic orders were considered up to $k = 21$. The resulting magnetic fields are verified by an according FEM calculation which show exact agreement. The field components in the air-gap between the AMD winding and the rotor ($r < R_3$) are obtained of the form

$$H_{sr,k} = \hat{H}_{s,k} \cos(2k\theta - \phi) \quad (4.32)$$

$$H_{s\theta,k} = -\hat{H}_{s,k} \sin(2k\theta - \phi). \quad (4.33)$$

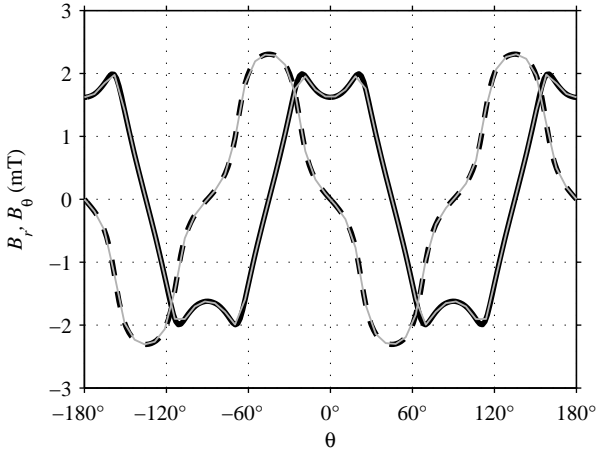


Figure 4.4: Armature field of a damper winding with $R_3 = 3.25\text{mm}$, $R_4 = 3.75\text{mm}$ and $R_5 = 6\text{mm}$ and a total current of $NI = 10\text{ A}$ in the air-gap ($r = 3\text{ mm}$), analytical solution for radial field component (solid black) and tangential component (dashed black) in comparison with an FEM calculation (fine gray).

As it will be seen in the following, only the fundamental component ($k = 1$) of the winding field will contribute to the magnetic force. For $k = 1$ the amplitude of magnetic field is obtained as

$$\hat{H}_{s,1} = \frac{\sqrt{2}\hat{J}r}{4\pi} \left(\frac{R_4^4 - R_3^4}{R_5^4} + \log\left(\frac{R_4}{R_3}\right) \right). \quad (4.34)$$

Maxwell Stress Integration

According to [76], the Maxwell stresses in a cylindrical coordinate system (r, θ) are given by

$$\sigma_{rr} = \frac{\mu_0}{2}(H_r^2 - H_\theta^2) \quad (4.35)$$

$$\sigma_{\theta r} = \mu_0 H_\theta H_r, \quad (4.36)$$

where H_r and H_θ denote the total field obtained by superposition of the permanent magnet field and the stator winding field. The magnetic

force can then be obtained by integration over a cylindrical surface surrounding the permanent magnet rotor on a radius r with $R_1 < r < R_3$ as

$$f_d = l_d r \int_0^{2\pi} (\sigma_{rr}|_r + j\sigma_{\theta r}|_r) e^{j\theta} d\theta. \quad (4.37)$$

With the integration over the full circumference $\theta = 0 \dots 2\pi$, the only contribution to a resultant force from the infinite sum of the winding harmonic field components (4.23) is the fundamental field component $H_{s,1}$. Therefore, only the fundamental field needs to be evaluated together with the permanent magnet field given in (4.12) to (4.15). Integration of the Maxwell stresses according (4.37) yields

$$\begin{bmatrix} f_{d,x} \\ f_{d,y} \end{bmatrix} = \hat{I} \cdot \Psi \cdot \begin{bmatrix} \cos(\varphi - \gamma) \\ \sin(\varphi - \gamma) \end{bmatrix}. \quad (4.38)$$

with the flux linkage

$$\Psi = \frac{8\sqrt{2}Nl_d R_1^2 B_{rem}}{\pi(R_4^2 - R_3^2)} \cdot \left(\frac{R_4^4 - R_3^4}{4R_5^4} + \log\left(\frac{R_4}{R_3}\right) \right). \quad (4.39)$$

Comparing the flux linkage obtained from the Lorentz force integration Ψ_{lrtz} to the flux linkage obtained from the Maxwell stress integration, one notices that they differ in the extra term $(R_4^4 - R_3^4)/(4R_5^4)$. With R_5 increasing, the influence of the stator back iron is reduced and comes closer to an iron-less design. As a result, Ψ approaches Ψ_{lrtz} for $R_5 \gg R_4$. Ψ cannot exceed $2\Psi_{lrtz}$ which is given by the limiting solution for an infinitely thin winding with $R_3 = R_4 = R_5$

Figure 4.5 shows the ratio of Ψ_{lrtz}/Ψ for geometry variations R_3/R_4 and R_5/R_4 . Good agreement is found to the observations made in [77], where the flux linkage of skewed windings was studied by means of three dimensional FEM. It seems that the ratio of Ψ_{lrtz}/Ψ of the straight winding is very close to the ratio of the skewed winding. Therefore in a practical approach, one may surrender the cumbersome three dimensional modeling of skewed or rhombic windings and estimate the flux linkage from Lorentz force based analytical models and correct it by a factor obtained by comparison to the above solution for the straight winding.

It is to be noted that the magnetic force is a linear function of the winding current. The armature reaction has therefore no degrading influence on the generated magnetic force.

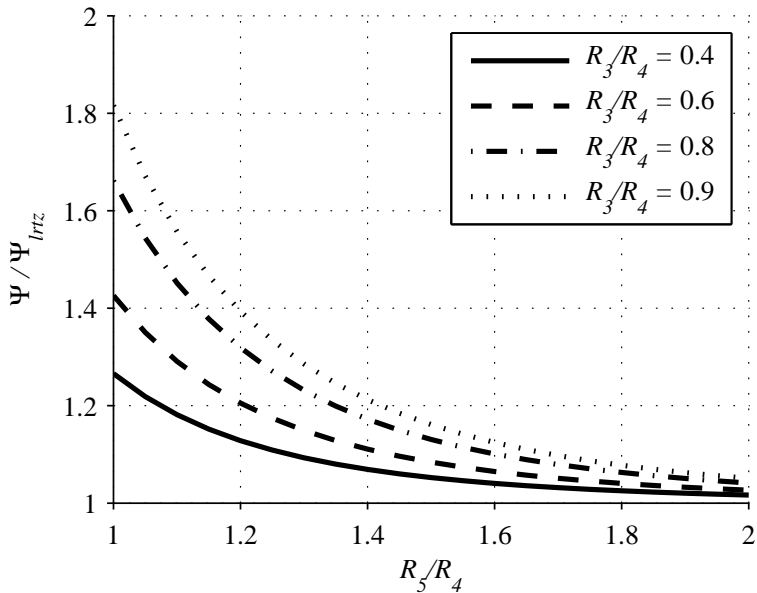


Figure 4.5: Ratio of flux linkage obtained from Maxwell stress integration Ψ to Lorentz force integration Ψ_{lrtz} depending on the geometry parameters winding inner radius R_3 , winding outer radius R_4 and stator back iron inner radius R_5 .

Equivalent Circuit Model

Similar to the equivalent circuit model of the homopolar damper winding, the terminal voltage of the heteropolar damper winding contains besides resistive and inductive contributions also induced voltages. An electrical model of the present winding type has been presented in [77]. For completeness, a detailed derivation of the model is given here.

For a rotor which is not rotating, the induced voltage is obtained from the principle of energy conservation. Considering the equations for the mechanical and electrical power for a non-rotating rotor

$$f_d \dot{\epsilon}^* = \Psi e^{-j\gamma} \cdot \hat{I} e^{j\varphi} \cdot \dot{\epsilon}^* = u_{ind}^* \cdot \hat{I} e^{j\varphi}, \quad (4.40)$$

where the operator $*$ denotes the complex conjugate of the respective quantity, it follows that the induced voltage due to the translational

motion $\dot{\epsilon}$ must be

$$u_{ind} = \Psi e^{j\gamma} \cdot \dot{\epsilon}. \quad (4.41)$$

When the rotor is displaced, an asymmetry exists and when rotating, the winding sees a changing flux alternating with the frequency of the rotational speed. Hence an induced voltage occurs with the frequency of the rotational speed. The resulting total flux linkage $\Phi(\epsilon)$ when displaced is closely related to the already derived Ψ which describes the current to force ratio of the winding.

In general, the induced voltage is given by the total flux linkage Φ as

$$u_{ind} = -\frac{d}{dt}\Phi. \quad (4.42)$$

Considering (4.41) which describes the induced voltage for a non-rotating rotor, the total flux Φ seen by the winding, when the rotor is displaced, can be obtained by integration as

$$-\Phi = \int \Psi e^{j\gamma} \cdot \dot{\epsilon} \cdot dt = \Psi e^{j\gamma} \cdot \epsilon \quad (4.43)$$

When the rotor is rotating, i.e. $\gamma = \Omega t$ the induced voltage is obtained as

$$u_{ind} = -\frac{d\Phi}{dt} = (\Psi \cdot \dot{\epsilon} + j\Omega\Psi \cdot \epsilon)e^{j\gamma}. \quad (4.44)$$

Together with the resistive and inductive voltage contributions, the terminal voltage can finally be written as

$$u = Ri + L\dot{i} + (\dot{\epsilon} + j\epsilon\Omega)\Psi \cdot e^{j\gamma}. \quad (4.45)$$

Transforming the above equation into a dq representation by means of the multiplication with $e^{-j\gamma}$ yields

$$u_{dq} = Ri_{dq} + (\dot{i}_{dq} + j\Omega i_{dq})L + (\dot{\epsilon} + j\epsilon\Omega)\Psi. \quad (4.46)$$

4.2 Evaluation of Sensing and Damping Concepts

For stabilization of the gas bearing by means of active magnetic damping, a position or velocity feedback information of the translational rotor motion will be needed. With the hybrid bearing approach, the

maximum rotor displacements are defined by the gas bearing's clearance which can be expected in the range of ten or maximally twenty micrometers. For successful control, the displacement sensing device needs to be capable of resolving the translational rotor motion within this micron-scaled range. Thus, high resolution and sensitivity will be required. The bandwidth specification is obtained from the required control dynamics analyzed in Chapter 5 and will generally be in the order of a few kilohertz. Depending on the type of gas-bearing and the dimension of the rotor to be stabilized, a high feedback gain may be demanded for stabilization.

A possible option for a displacement measurement would be the use of conventional non-contact type distance sensors such as eddy current, inductive, capacitive, optical or hall element sensors. An evaluation of the mentioned sensor types for use in AMB systems has been conducted in [78] with the conclusion that the eddy current sensor is the preferred choice for AMB systems featuring high resolution, high bandwidth and a low sensitivity to environmental influences.

Printed circuit board (PCB) based eddy current sensors have been presented in [79, 80]. These so called transversal flux eddy current sensors use search coils implemented as tracks on a multi-layer PCB and can therefore be realized in a very compact form such that only a small portion of the rotor length needs to be spent for position sensing.

Rotor length is a critical design parameter in ultra-high-speed drives as the length severely influences the rotordynamics and therewith in most cases imposes a speed limitation. The speed limitation is given by the first bending mode. Excitation thereof with the fundamental component of the rotational speed as a result of residual imbalance usually ends destructive. When approximating the rotor as an Euler-Bernoulli beam, the frequency of the first bending mode scales inversely proportional to the square of the rotor length [81]

$$\omega_{bend} \propto \frac{1}{l_{rotor}^2}. \quad (4.47)$$

Therefore, displacement sensing concepts which completely avoid additional rotor length are preferred. In AMB designs, concepts without the need of additional sensors but reusing the actuator's winding along with the bearings linear or switched amplifier for displacement sensing are referred to as self-sensing AMB concepts. While with the present magnetic damper design, the two-fold use of the damper winding as

both actuator and displacement sensor search coil is of primary concern, the reuse of the damper's amplifier is not seen as an absolutely needed requirement.

Two main approaches of displacement self-sensing techniques for the slotless damper design can be thought of. They can be divided into observation based concepts and high frequency test signal injection based concepts. Concepts based on the derived electrical winding model, which observe the displacement and velocity by means of the dampers back-EMF voltage appear theoretically possible at first glance, which gives reason for a more detailed analysis.

Test signal injection concepts have widely established in active magnetic bearing systems. Mainly based on the extraction of the displacement dependent self-inductance of the actuator, these concepts however cannot be applied directly with slotless AMB or AMD designs. Therefore, a new eddy current based signal injection self-sensing method is developed in the scope of the present work.

As a basic control law, damping can be realized by providing a force proportional to the translational rotor velocity $f_d = d\dot{\epsilon}$, where d denotes the damping factor. The corresponding transfer function in the Laplace domain is

$$f_d = -d \cdot \epsilon \cdot s. \quad (4.48)$$

With this definition, damping forces are -90° phase shifted to the displacement signal with its amplitude increasing with higher frequencies. Therefore, either a rotor displacement measurement ϵ which needs to be derivated, or a direct measurement of the translational rotor velocity $\dot{\epsilon}$ can be used for control. Depending on the particular damper concept, either a measurement of ϵ or $\dot{\epsilon}$ will be preferred.

4.2.1 Back-EMF based Homopolar Damper

Originating from the back electromotive force (EMF) the term $\dot{\epsilon}$ appears in the electrical model of the homopolar damper winding (4.3). A very simple form of a magnetic damper can therefore be realized when generating a damping force $f_d \propto \dot{\epsilon}$ by sensing the the actuators back EMF voltage and directly feeding back a damper current i which is proportional thereto, i.e.

$$i \propto \Psi \cdot \dot{\epsilon}. \quad (4.49)$$

In this section, both a passive and an active approach are examined in an attempt to achieve a current proportional to the back EMF

voltage.

Passive Damping

First, the damper force of a homopolar winding with shorted terminals is studied. Transforming (4.3) into the Laplace domain, the terminal voltage is forced to zero as

$$u = \Psi \cdot \epsilon \cdot s + Li \cdot s + Ri = 0. \quad (4.50)$$

Solving for the damper current i and combining with the current to force relation from (4.1), the damper force is obtained as

$$f_d = \frac{-\Psi^2 \epsilon s}{Ls + R}. \quad (4.51)$$

For frequencies below the cutoff frequency $\omega_c = R/L$, a damping force is provided with a damping factor equivalent to $d = \Psi^2/R$. For frequencies above ω_c , the phase of the force fades to -180° and therefore, the damper provides no longer a damping force but adds stiffness to the bearing rotor system. In a given design, the bandwidth limit represented by ω_c can be changed by the choice of the winding turn number N as $\omega_c \propto 1/N$; however by simultaneously scaling the damping factor $d \propto N$.

Active Damping

Higher amounts of damping can be achieved by means of additional active circuitry. A circuit topology employing a linear amplifier which then allows for an increased bandwidth and damping factor has been investigated in [82]. A schematic thereof is depicted in Figure 4.6. Besides an operational power amplifier, the circuit contains two capacitors C_{01} and two resistors, R_{01} and R_{02} . With the circuit, the necessary degree of freedom is added in order to compensate for the winding inductance L and resistance R . The transfer function from the displacement to the damper force obtained from the winding together with the amplifier circuit can be written as

$$f_d = \frac{-\Psi^2 \epsilon s}{(L - R_{01}R_{02}C_{01})s + R - R_{02}}, \quad (4.52)$$

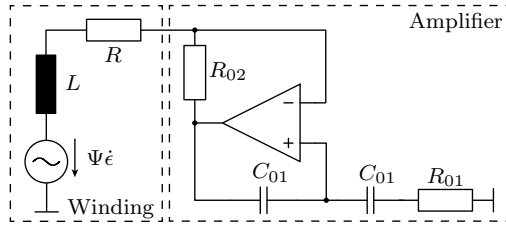


Figure 4.6: AMD configuration with a homopolar winding and a power amplifier with compensation of the winding resistance R and inductance L .

which is as with the passive system of the above section again a first order system. From the transfer function is seen that the winding resistance R can be compensated with the choice of R_{02} , which allows to adjust the gain at low frequencies $d = \Psi^2/(R - R_{02})$. The bandwidth $\omega_c = (R - R_{02})/(L - R_{01}R_{02}C_{01})$ can be adjusted with the choice of R_{01} and C_{01} . A necessary stability criterion is that all coefficients of the denominator polynomial in s need to have the same sign (Routh-Hurwitz stability criterion). Attention must therefore be paid not to overcompensate R and L . The two resistors need to be chosen $R_{02} < R$ and $R_{01} < R_{02}C_{01}/L$ in order not to change the sign of the damping force which would result in negative damping and/or render the electrical system unstable.

For damping forces in both radial directions x and y a damper with two phases, i.e. windings in x and y directions each with a dedicated amplifier is needed. In this case, the windings of the two phases are arranged perpendicularly according Figure 4.1 and therefore in theory no magnetic coupling exists between the two phases. In a practical implementation a mutual magnetic coupling will always exist as a result of small asymmetries in the arrangement of the individual conductors. Under consideration the mutual inductance M , the winding model with the two phases can be written as

$$u_x = \Psi \dot{\epsilon}_x + L \dot{i}_x + M \dot{i}_y + R i_x \quad (4.53)$$

$$u_y = \Psi \dot{\epsilon}_y + L \dot{i}_y + M \dot{i}_x + R i_y. \quad (4.54)$$

The damper transfer functions for the two damping directions are then

given by

$$f_{d,x} = \frac{-\Psi^2((L'\epsilon_x - M\epsilon_y)s^2 + R'\epsilon_x s)}{(L'^2 - M^2)s^2 + 2L'R's + R'^2} \quad (4.55)$$

$$f_{d,y} = \frac{-\Psi^2((L'\epsilon_y - M\epsilon_x)s^2 + R'\epsilon_y s)}{(L'^2 - M^2)s^2 + 2L'R's + R'^2}, \quad (4.56)$$

where for the passive damper the equivalent resistance and inductance is $R' = R$ and $L' = L$ and for the active damper $R' = R - R_{02}$ and $L' = L - R_{01}R_{02}C_{01}$.

For moderate gains and a small magnetic coupling two independent amplifiers will still deliver damping forces. At higher frequencies the phases will fade to -180° , adding stiffness. When large gains are needed, the existence of a magnetic coupling M can yield a violation of the stability criterion and therefore render the electrical system unstable. Compensation of M would then be required.

For high gains of the damper, modeling accuracy and invariability of the winding's resistance R and inductance L under the all operating conditions are seen key factors in order to succeed with back-EMF based dampers. The high sensitivity of control performance to slight parameter variations, e.g. due to temperature variations, requires tuning of the circuit within safe margins. As a consequence, the adherence of these margins inherently puts a limitation to the achievable gain and bandwidth.

4.2.2 Back-EMF based Heteropolar Damper

In the previous section it has been seen that a damping force is produced when shorting the damper winding. This observation is consistent with the basic principle summarized in Lenz's law that an induced electromotive force causes a current whose magnetic field opposes the origin of the initial flux change and hence produces a force against the driving motion. As back-EMF voltages due to rotor motion also appear in the electrical model of the heteropolar magnetic damper winding, a similar effect could be expected for the heteropolar actuator. Therefore, the resulting forces of the short circuited heteropolar winding are studied in the following.

Considering the model in the dq representation (4.46), the corresponding equation for the voltage in the Laplace domain can be written

as

$$u_{dq} = R \cdot i_{dq} + L \cdot \dot{i} \cdot (s + j\Omega) + \Psi \cdot \epsilon \cdot (s + j\Omega) \quad (4.57)$$

$$(4.58)$$

Forcing $u_{dq} = 0$ and solving for the current yields

$$i_{dq} = \frac{-\Psi \cdot (s + j\Omega) \cdot \epsilon}{L \cdot (s + j\Omega) + R} \quad (4.59)$$

The corresponding force is then

$$f_d = \Psi \cdot i_{dq} = \frac{-\Psi^2 \cdot (s + j\Omega) \cdot \epsilon}{L \cdot (s + j\Omega) + R}, \quad (4.60)$$

which is a similar form of a transfer function as for the short circuited homopolar damper except for the frequency shift $s \rightarrow s + j\Omega$.

The generalized frequency response of f_d/ϵ is plotted in Figure 4.7. When the rotor is rotating with a speed Ω , the winding generates a static restoring force and a cross coupling force which will not help stabilizing the gas bearing. The winding acts as an electrodynamic magnetic bearing [83], which itself needs a damper in order to be stabilized. Thus, it is clear that the short circuited homopolar winding cannot be used as a damper.

In a digital observer based approach measuring the winding currents and terminal voltages, it seems theoretically possible to estimate the rotor radial velocity \dot{e} and feed back a current which generates a damping force. But it is seen as a major challenge to extract the back-EMF voltage caused by rotor translational motion and resolve the rotor motion of micrometer or sub-micrometer amplitude with sufficient accuracy. Depending on the controller gain and the design of the actuator, voltage drops across the winding resistance R and the inductance L are estimated orders of magnitude larger than the back-EMF voltage from rotor motion. Finally, the same difficulty as with the homopolar active damper concept exist, that the adherence of margins for the compensation of R and L will represent an inherent limitation to the achievable feedback gain and bandwidth.

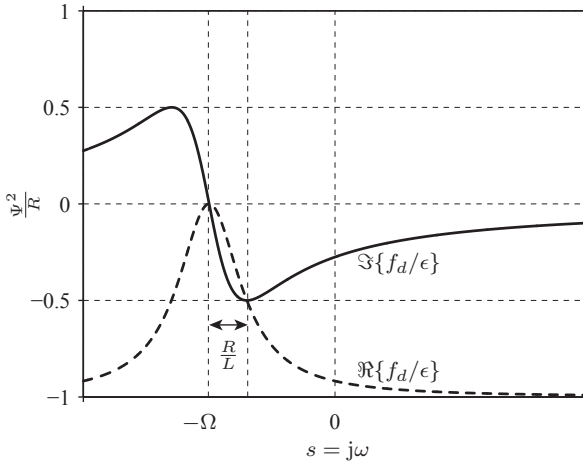


Figure 4.7: Frequency response f_d/ϵ of the short circuited heteropolar damper winding.

4.2.3 Eddy current based self-sensing concept

Signal Injection Self-Sensing AMBs

The concept of test signal injection has been widely employed in both AMB systems and rotating electrical machines. The concept utilizes an auxiliary high frequency test signal to extract information on the rotor's translational or angular position. Rather than extracting the information from the existing back-EMF voltage which may be concealed by resistive and inductive voltage contributions due to large actuator currents, the signal injection approach employs the test signal at a frequency above the actuator current control bandwidth to make visible the position information which then allows for a more independent position measurement.

In self-sensing AMB systems, the concept of high frequency test signal injection for rotor displacement sensing has therefore yielded superior results than back-EMF observer based approaches [84]. An overview on different implementations of signal injection self-sensing AMB systems is given in [85, 21]. In AMB systems, the signal injection concept is usually accomplished with reluctance type AMB designs where the bearing forces are generated by means of a ferromagnetic ro-

tor and coils on a ferromagnetic stator forming an electromagnet. For the reluctance type AMB the generated force f can be written as a function of the magnetic energy W_{mag} as

$$f = \frac{dW_{mag}}{d\epsilon} = \frac{dL}{d\epsilon} \cdot i^2, \quad (4.61)$$

where L denotes the actuators inductance and i is the actuator current. From the above equation it is seen, that a force is generated due to the displacement dependent inductance change $\frac{dL}{d\epsilon}$. Therefore with this type of bearing, which force generation principle inherently depends on the displacement dependent inductance, the rotor displacement ϵ can always be deduced from the observation of the actuator's inductance.

In a self-sensing displacement measurement approach, the bearing's linear or switched power amplifier is commonly used to superimpose a high frequency voltage or current signal on the actuator's control voltage respectively control current. The actuator's response is then measured with the already existing current sensors [84] or also by means of a dedicated signal extraction circuit such as e.g. a Wheatstone bridge [85]. The position signal is contained in the amplitude of the high frequency carrier signal which needs to be extracted using an amplitude demodulation technique. For the mentioned systems, the frequency of the carrier signal was chosen some tens of kilohertz. Much higher frequencies would not be recommended because of eddy currents in the employed ferromagnetic materials degrading the displacement to inductance relation.

With reluctance type AMBs, signal injection based displacement self-sensing can be seen as the reuse of the existing actuator coil and electronics for an implementation of an inductive distance sensor. In a slotless damper design as is intended in the present work for ultra-high-speed applications, only a marginal displacement dependent inductance change exist, which would originate from the relative permeability of the permanent magnet being slightly greater than one ($\mu_r \approx 1.05$). In practice, the inductance change will hardly be measurable. Therefore the method cannot be applied straightforward with slotless designs.

Eddy current based self-sensing

In a slotless design, rather than exploiting magnetic reluctance, the impedance change of the winding due to eddy currents can be utilized for displacement self-sensing as is done in eddy current distance sensors.

A review on eddy current distance sensor design is given in [86]. The working principle of an eddy current sensor can be summarized as follows. A search coil conducting an alternating current in proximity of a solid electrical conductor will cause eddy currents on the conductor's surface which counteract the causing magnetic field of the coil and effect a change of the coil's impedance. As the effect is dependent on the relative distance between the search coil and the conductor, it can be exploited for displacement sensing.

Instead of utilizing a single search coil, a modified type of eddy current sensor has been suggested for AMB systems in [79]. It makes use of an excitation coil and two with respect to the rotor oppositely arranged search coils which are connected anti-serially. Thus, a total induced voltage in the series connection exists when the magnetic fluxes on the two coils differ, i.e. no voltage is measured for a centered rotor. When displaced, the voltage increases and takes the sign of the displacement. In [79], a PCB based implementation of the so called transversal flux eddy current sensors has been proposed. A sensitivity optimization has been conducted in [80] for use in a high-speed AMB system with a target speed of 500 krpm. The same type of sensor has also been used in [6] in an AMB system with a demonstrated speed of 500 krpm.

In an eddy current based self-sensing AMD design, neither the use of an extra coil for excitation nor an axial flux winding arrangement is in accordance with the concept of a self-sensing design and employable actuator windings. Therefore, a winding arrangement similar to state-of-the-art reluctance type bearings is suggested where two oppositely arranged coils are used for displacement measurement in a radial flux configuration such that the existing damper winding coils can be reused. The principle of anti-serial coil connection is adopted in order to obtain a signal according to the amplitude and sign of the displacement.

A drawing of the suggested coil arrangement is depicted in Figure 4.8. The coil on the left side of the y axis is denoted as L_{x-} and the coil on the right side is denoted as L_{x+} . For a positive displacement ϵ_x , eddy currents predominate on the right side. Thus, the impedance seen on the terminals of L_{x+} is smaller than the impedance of L_{x-} . Another pair of coils will be needed for the measurement of the displacement ϵ_y in y direction. For this purpose, a pair of coils L_{y+} and L_{y-} must be arranged accordingly along the y axis.

As a result of the magnetic coupling of the coils L_{x+} and L_{x-} to the coils L_{y+} and L_{y-} and vice versa, the impedance of a coil must be

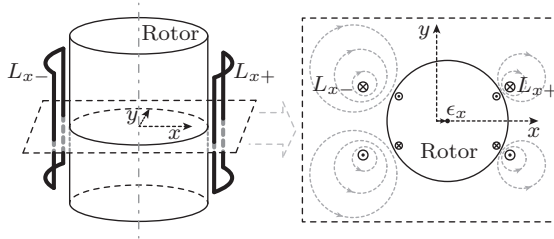


Figure 4.8: Coil arrangement of for eddy current displacement sensing.

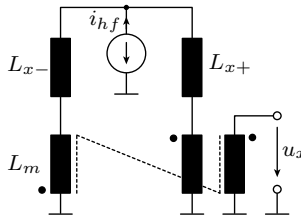


Figure 4.9: Measurement bridge for eddy current based displacement measurement employing a differentially coupled inductor L_m .

assumed a general function of the rotor displacements in both x and y direction. For the coil L_{x-} the impedance can be defined as

$$Z_{x-} = Z_x(\epsilon_x, \epsilon_y). \quad (4.62)$$

Assuming symmetry, L_{x+} will correspond to $Z_{x+} = Z_x(-\epsilon_x, \epsilon_y)$. For small rotor displacements, the coil impedances can then be described by their first order approximations as

$$Z_{x+} \approx Z_0 - \frac{\partial Z_x}{\partial \epsilon_x} \cdot \epsilon_x + \frac{\partial Z_x}{\partial \epsilon_y} \cdot \epsilon_y \quad (4.63)$$

$$Z_{x-} \approx Z_0 + \frac{\partial Z_x}{\partial \epsilon_x} \cdot \epsilon_x + \frac{\partial Z_x}{\partial \epsilon_y} \cdot \epsilon_y \quad (4.64)$$

where $Z_0 = Z_x(0, 0)$ denotes the coil impedance for a perfectly centered rotor.

To measure the impedance change, a modified Wheatstone bridge is proposed which instead of resistors employs a differentially coupled

inductor L_m , as depicted in Figure 4.9. Injecting a high frequency test current i_{hf} into the mid-tapping of the series connected coils L_{x+} and L_{x-} , the current will split into the two branches L_{x+} and L_{x-} according to the ratio of their impedances Z_{x+} and Z_{x-} . Rather than measuring a voltage difference by means of a difference amplifier as would be the case with an ordinary Wheatstone bridge, the differentially coupled inductor L_m is used to measure the difference of the currents in L_{x+} and L_{x-} . As a nonzero winding resistance of L_m will exist in an implementation which would add a common mode voltage on the measurement signal, the voltage u_x corresponding to the current difference of the two branches L_{x+} and L_{x-} is measured on the terminal of the third coupled inductor, which is not conducting the injected high frequency current.

The proposed measurement principle with the differentially coupled inductor can be expected to allow higher test signal frequencies than with a difference amplifier implementation, as the common mode rejection ratio for available state-of-the-art difference amplifiers is known to degrade with increasing frequency.

The voltage across the inductor L_m measured to ground can be calculated as

$$u_x = i_{hf} \cdot \frac{Z_m}{Z_0 + \frac{\partial Z_x}{\partial \epsilon_y} \cdot \epsilon_y + 2Z_m} \cdot \frac{\partial Z_x}{\partial \epsilon_x} \cdot \epsilon_x. \quad (4.65)$$

When assuming that the impedance change $\frac{\partial Z_x}{\partial \epsilon_y} \cdot \epsilon_y$ due to a displacement in y -direction is small compared to the nominal coil impedance Z_0 , the measured voltage u_x simplifies to

$$u_x = i_{hf} \cdot \frac{Z_m}{Z_0 + 2Z_m} \cdot \frac{\partial Z_x}{\partial \epsilon_x} \cdot \epsilon_x, \quad (4.66)$$

wherefrom it can be seen that the measured voltage u_x is directly proportional to the displacement ϵ_x . The amplitude of u_x is mainly given by the term $\frac{\partial Z_x}{\partial \epsilon_x}$ which can be defined as the sensitivity of the coil arrangement.

To apply the measurement principle in an eddy current based self-sensing design, the damper winding needs to be to partitioned such to obtain the required arrangement of the four search coils L_{x+} , L_{x-} , L_{y+} and L_{y-} . A self-sensing winding configuration can then obtained by combining the measurement bridge and search coils to superimpose a damper drive current, which will be detailed in Section 4.3

Quantity	Symbol	Value
Inner radius	R_3	3.25 mm
Outer radius	R_4	4.25 mm
Length	l	12 mm
Number of turns per coil	N	20
Inductance	L_{x+}, L_{x-}	5.6 μ H

Table 4.1: Test coil specifications for eddy current displacement measurement

Sensitivity Measurement

In order to evaluate the suitability of the coil arrangement and the proposed measurement bridge for an eddy current based self-sensing AMD concept, a measurement of the sensitivity for a test winding has been conducted. A wire wound winding with dimensions given in Table 4.1 together with a solid 6 mm stainless steel rod (1.4301) is used for this purpose.

For the coupled inductor L_m a double-aperture core (Epcos K1) with three windings of each 10 μ H is used. A high frequency current with an amplitude of $i_{hf} = 20$ mA is injected into the winding and the voltage u_x is measured at the measurement bridge output. Figure 4.10 shows the measured output voltage u_x normalized with the injected current i_{hf} as a function of the rotor displacement ϵ_x for injection frequencies of 1 to 15 MHz.

Relating the impedance change to the total coil impedance allows for a comparison with the AMB eddy current sensor design of [80]. The relative impedance change can be calculated as

$$\frac{1}{Z_0} \frac{\partial Z_x}{\partial \epsilon_x} = \frac{1}{\epsilon_x} \frac{u_x(i_{hf}Z_m + u_{hf})}{u_x^2 + i_{hf}Z_mu_{hf}}, \quad (4.67)$$

where u_{hf} denotes the voltage measured at the mid-tapping of the series connection of L_{x+} and L_{x-} . Using a linear fit in ϵ_x to approximate the measurement of $\frac{u_x}{i_{hf}}$, the relative sensitivity per unit displacement as a function of the injection frequency is obtained and plotted in Figure 4.11.

The measurement shows a significant increase of sensitivity with increased frequencies. Therefore, a signal injection frequency of 10 MHz or higher must be considered in a design. At a frequency of 10 MHz,

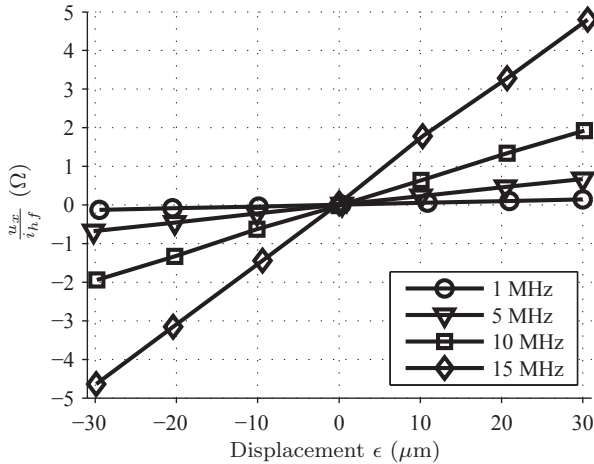


Figure 4.10: Measurement bridge output voltage u_x normalized with the injected current i_{hf} as a function of the rotor displacement ϵ_x .

the relative impedance change is approximately 0.1% per micrometer which is approximately sixty times more than for the transversal flux eddy current sensor design presented in [80], where a relative change of 0.0017% per micrometer can be constituted. The higher sensitivity is mainly attributed to the different arrangement of the coils which are located at closer distance and parallel to the rotor instead of perpendicular, exploiting a larger area of the rotor.

With the much higher sensitivity compared to the mentioned AMB sensor design, the resolution of the proposed eddy current sensing concept can be expected sufficiently high to measure the rotor motion within the gas bearing's clearance.

4.2.4 Comparison of the Concepts

While the passive homopolar damper goes without additional electronics at all it represents the most simple damper concept analyzed concerning required electronics. Though very simple in design, influence on the control is very limited. With the addition of merely an operational amplifier plus a few passive components a very simple active damper

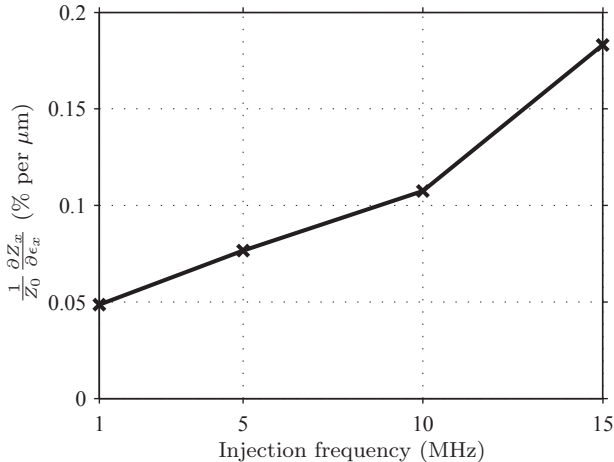


Figure 4.11: Relative sensitivity per micrometer of the eddy current position test measurement as a function of the injection frequency.

concept was shown. Based on the back-EMF voltage raised by translational journal motion, the controller design requires certain margins which put a limitation on the achievable gain and bandwidth.

The simplicity in the damper electronics however comes with a more complicated rotor construction as an additional radially or axially magnetized permanent magnet is required which cannot be easily integrated into the active region of the electric machine. Therefore, it will require additional rotor length which then represents a limit to the achievable speed for rotordynamic reasons.

Heteropolar dampers can be integrated much better into the permanent magnet machine as requiring a diametrically magnetized permanent magnet which is already present. While the attempt of construction of a passive heteropolar damper does not yield the desired damping functionality, a back-EMF observer based heteropolar damper concept is considered too vulnerable to modeling errors and is therefore not seen as a robust solution.

Providing a high sensitivity displacement measurement by means of an eddy current based self-sensing approach, rotor motion can be controlled independently and without inherent gain and bandwidth re-

strictions. Clearly, the complexity on the electronics side is considerably higher compared to the homopolar concepts as the construction of an eddy current sensor signal processing electronics will be required. However, providing the highest flexibility in control among the studied concepts and with the ease of integration into the electrical machine, the eddy current based self-sensing AMD is considered the preferred choice for stabilization of gas bearings in a slotless high speed permanent magnet machine.

4.3 Heteropolar Eddy Current based Self-Sensing AMD

As already stated earlier, the heteropolar damper uses a winding with a pole pair number of $p_s = 2$ which together with a permanent magnet rotor with a pole pair number of $p_r = 1$ yields a force f_d which amplitude and direction is determined by the damper current space vector $i = \hat{I}e^{j\varphi}$ and the angular rotor position γ .

The motor winding uses a pole pair number of $p_{mot} = 1$ which then with the permanent magnet rotor of $p_r = 1$ produces force couple corresponding to a torque T_z . As both damper and motor winding use the same pole pair number on the rotor, the damper winding can be integrated into the active region of the motor as depicted in Figure 4.2.

The damper winding is arranged on the innermost possible radius given by the rotor radius and the minimum required physical air gap in order to maximize the sensitivity of the displacement measurement. The eddy current displacement measurement is accomplished through the metallic retaining sleeve which is primarily thought to protect the brittle permanent magnet from bursting at high rotational speeds. The sleeve represents a high quality homogenous conducting surface which is ideally suited for eddy current displacement sensing.

The motor winding is placed adjoining the damper winding and fills the remaining volume to the inner radius of the stator back iron. Clearly the torque capability of the motor will be reduced as a result of the damper winding decreased volume of the motor winding. According [74] the torque is proportional to

$$T_z \propto \frac{4}{3} - \frac{R_4}{R_5} - \frac{1}{3} \frac{R_4^3}{R_5^3}, \quad (4.68)$$

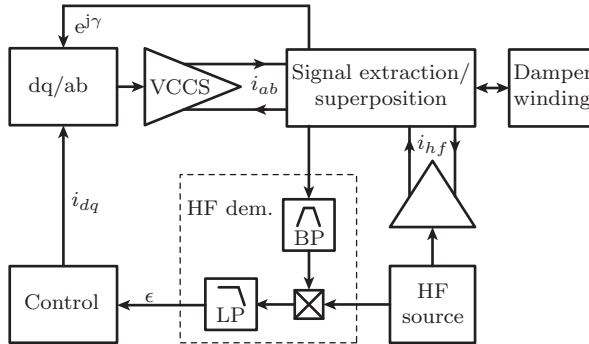


Figure 4.12: Functional diagram of the eddy current self-sensing damper with an auxiliary signal separation and extraction circuit.

when R_5 is assumed constant. Thus in the first instance, the torque reduction goes only linear with R_4 and will therefore not represent a fundamental limitation in most cases.

4.3.1 Functional Overview

In Section 4.2.3 it was found by means of a test measurement, that for the proposed eddy current based displacement self-sensing approach, a test signal frequency of 10 MHz or higher will be needed. Signal injection at this frequency is hard to accomplish with the damper's own power amplifiers which will be designed to deliver actuator currents with a bandwidth of a few tens of kilohertz maximally. A different approach employing dedicated signal injection and extraction circuits is therefore followed. An abstracted functional diagram of the proposed eddy current based self-sensing approach is shown in Figure 4.12.

The damper winding is connected to a signal superposition and extraction circuit which superimposes the high frequency carrier current i_{hf} on the damper phase currents i_{ab} and feeds the superimposed currents to the winding and back again. The high frequency carrier signal is generated by an auxiliary signal source which is buffered to provide the necessary current amplitudes. The high frequency displacement signal, which is extracted from the winding currents, contains the displacement information in its amplitude. It is processed through the known steps of amplitude demodulation to obtain the displacement ϵ . Accordingly,

the modulated signal is first processed through a bandpass filter followed by a frequency mixer. After the mixer, the signal is processed through a low-pass filter which eliminates the high frequency spectral components and yields a signal proportional to the displacement ϵ . The bandwidth of the displacement measurement signal is mainly given by the characteristics of the employed low-pass filter.

As control has to be accomplished field oriented, a transformation of the dq control reference currents into the phase reference currents i_a and i_b is needed. A measurement of the angular rotor position in terms of $e^{j\gamma}$ or equivalently in terms of $\sin\gamma$ and $\cos\gamma$ is therefore required, which can be obtained from the winding's back-EMF voltage (see Section 4.3.5).

The damper power amplifier, which takes the control reference currents as an input and injects the damper currents via the superposition circuit into the damper windings, can be seen idealized as a voltage controlled current source (VCCS).

4.3.2 Winding Concept

As discussed in Section 4.2.3, two oppositely arranged coils L_{x+} and L_{x-} are needed to measure the displacement ϵ_x in x direction. For the measurement of ϵ_y in y direction, another pair of coils L_{y+} and L_{y-} must be arranged perpendicularly thereto. In order to reuse the damper winding analyzed in Section 4.1.2 as an eddy current sensor search coil, phase A needs to be wound in a way such to obtain the four coils L_{x+} , L_{x-} , L_{y+} and L_{y-} . As electrical access is needed to each of the coils, additional tappings within phase A are required. Phase A needs therefore be split into the four distinct coils as depicted in the winding cross section view in Figure 4.13. The winding sense is indicated by the dots. Phase B is not used for search coils and thus remains unchanged.

A series connection of the four coils is finally required to form phase A . The order of the series connection is unconstrained and can be chosen later to meet the requirements for eddy current signal extraction; only, the winding sense of the coils indicated by the dot must be maintained in the series connection.

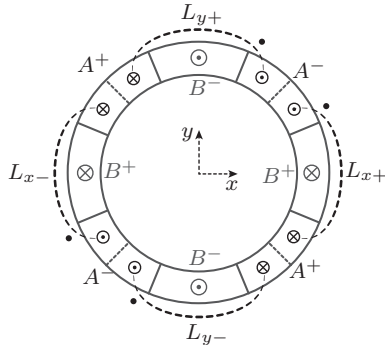


Figure 4.13: Cross section view of the proposed two-phase damper winding for reuse as eddy current search coils. Phase A is split into four distinct coils, L_{x+} and L_{x-} to measure the displacement in x direction ϵ_x and L_{y+} and L_{y-} to measure the displacement in y direction ϵ_y . Phase B is not used for displacement sensing and remains unchanged.

4.3.3 Circuit Topology

A key challenge of the proposed eddy-current self-sensing approach is to provide a circuit topology with the functionality of the signal superposition and extraction block which has been introduced the block diagram of Figure 4.12. Clean signal separation of the translational rotor displacement and angular position measurement from the actuator currents is needed for unconstrained control. Otherwise, cross talk from the actuator currents to a measurement channel will set a limitation to the achievable gain and control bandwidth. Fortunately, the required actuator current control bandwidth is in the range of a few tens of kilohertz while eddy current displacement sensing uses frequencies of 10 MHz or higher. Given this huge discrepancy in frequencies of interest, signal separation can be accomplished with an appropriate circuit topology employing frequency dependent passive components such as inductors and capacitors.

For eddy current displacement self-sensing, a modified Wheatstone measurement bridge according Figure 4.9 is favored. Two instances of the measurement bridge for the measurement of x and y displacements must be combined to obtain the required series connection of the four coils L_{x+} , L_{x-} , L_{y+} and L_{y-} from phase A.

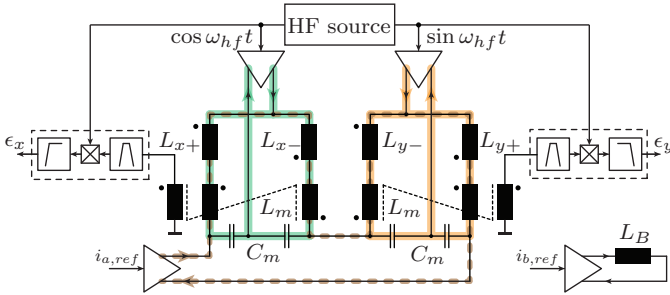


Figure 4.14: Eddy current displacement self-sensing topology with auxiliary signal injection and extraction circuits (serial type). The damper current is flowing through the serially connected coils L_{x+} , L_{x-} , L_{y+} and L_{y-} of phase A and also the coupled measurement inductors L_m (dashed brown line). The high frequency test signals are superimposed by of capacitive coupling through C_m (green and orange lines).

Two possible circuit topologies are proposed; a topology where the damper current flows through the measurement inductor L_m in series to the four coils and another topology where the measurement inductor L_m does not conduct a damper current but is arranged in a parallel branch to damper current flow. Accordingly, the two topologies will be referred to as serial and parallel type topologies.

Serial Type Topology

A possible circuit topology providing the desired functionality of signal superposition and separation is depicted in Figure 4.14.

As the two coil pairs for position measurement in x and y direction are magnetically coupled, orthogonal injection signals are needed to avoid a coupling of the two measurement channels. Hence a sine and a cosine signal or 90° phase shifted rectangular signals can be used. The signal injection buffer must either operate from an isolated supply or use a capacitive coupling at its output, which is necessary for two reasons.

- The damper current from the power amplifier should not be drained

off through the signal injection buffers via possible ground connections and therewith change the intended current distribution in the winding which then would yield an altered damper force.

- Each of the four coils generate an induced voltage during rotor rotation which in the series connection cancel each other out; but, at the mid-point of the series connection the induced voltage is visible (see also Section 4.3.5). Thus, the capacitive coupling or isolated supply of the injection buffers is needed to decouple and protect the signal injection buffers from the possibly high induced voltages.

The return path of the high frequency injected current is defined by a low impedance at the high frequency provided by the capacitors C_m . In the frequency range of the damper current, the capacitors represent a high impedance and therefore drained off currents through C_m are negligibly regarding the damper force generation, of course only as long as C_m is dimensioned properly with a sufficiently small value.

As the capacitors C_m bypass high frequency components contained in the damper current, they prevent them from being conducted through the measurement bridge which would generate a disturbance signal on the output of the measurement inductor L_m . Hence to minimize cross talk from the damper current to the displacement measurement, the capacitors C_m would need to be chosen as large as possible. A trade-off must therefore be taken in the dimensioning of C_m which however with the huge discrepancy in the two competing frequency bands of the damper current and the high frequency injection signal imposes no further problem.

One major drawback of the parallel type topology is that the measurement inductor L_m conducts the damper current, which has several consequences.

- It is obvious that the L_m has to be designed for the damper RMS current regarding the thermal dimensioning, respectively for the peak current regarding its magnetic core. A relatively large inductor size will therefore result.
- The damper current flow through L_m is twice in the same direction regarding the inductor's winding sense and hence a major flux is contributed which generates a signal on the output of the

measurement inductor. This signal must then be sufficiently suppressed by the subsequent demodulation stage in order to avoid cross coupling.

- As the flux density within the core of L_m will primarily be defined by the damper current, a slight variation of the inductance value of L_m will occur as the permeability of the core material is not exactly constant but is a function of the flux density. As can be seen from the equation derived for the measurement bridge output voltage (4.66), a variation of L_m will modulate the measurement signal. As a result, a cross talk from the damper current to the displacement measurement will be observed. The dependency is given by the absolute value of the damper current i_a which defines the amplitude of the flux density and hence the relative permeability.

Phase B which is symbolized by the inductor L_B in Figure 4.14 is not used for position sensing and is therefore simply connected to a power amplifier providing a damper current i_b .

Parallel Type Topology

A topology avoiding damper current flow through the measurement inductor L_m is the parallel type topology depicted in Figure 4.15. The high frequency test signal injection with the capacitors C_m and the consideration for the injection buffer with a capacitive coupled output or isolated supply is resumed from the parallel type topology.

The main difference is the way and location of the damper current injection which is accomplished through additional inductors L_c connected directly to the series connection of the winding coils. The inductors are needed to avoid the high frequency injected current from being drained through the damper power amplifier. The inductors need to be dimensioned for the damper current and must have a sufficiently high impedance at the test signal injection frequency. Linearity and stability of the inductance value is of minor importance if chosen large enough. Also for the measurement inductor L_m , the choice of the core material is uncritical. L_m is dimensioned only for the high frequency injection current and can therefore be of a much smaller size than with the serial topology.

Comparing to the serial type topology, a difference exist in the dimensioning of the capacitor C_m . High frequency spectral components

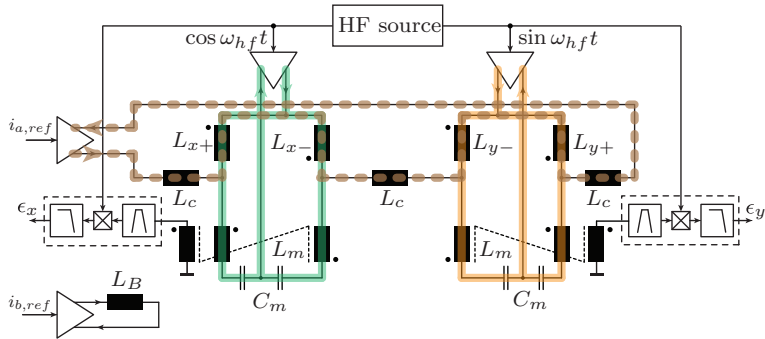


Figure 4.15: Eddy current displacement self-sensing topology with an auxiliary signal injection and extraction circuits (parallel type). The damper current is flowing through the serially connected coils L_{x+} , L_{x-} , L_{y+} and L_{y-} of phase A (dashed brown line) but not through the measurement inductor L_m . The high frequency test signals are superimposed by of capacitive coupling through C_m (green and orange line). The inductors L_c are required for signal separation.

of the damper current leaking through the parallel path given by L_m and C_m constitute a disturbance signal measured on the output of the measurement bridge. This effect is the main source for damper current to displacement measurement cross talk. The capacitors C_m have to be dimensioned as small as possible but still large enough to guarantee a sufficiently small impedance to conduct the injection current at high frequencies. In order to minimize cross talk, the damper power amplifier should be designed with a lowpass characteristic such that high frequency components are suppressed before the damper current is injected into the measurement circuit.

4.3.4 Power Amplifier

As mentioned above, the damper power amplifier needs to be implemented with a lowpass characteristic in order to minimize cross talk from the damper currents to the displacement signals. Using a discrete-time digital displacement feedback control and accordingly, discrete-time current reference signals, the lowpass power amplifier primarily takes the role of an interpolation filter, smoothing the current output

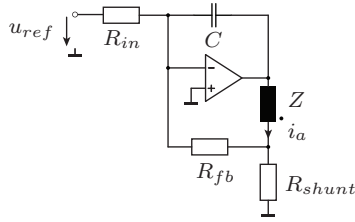


Figure 4.16: Damper linear power amplifier with lowpass characteristic.

response to the current reference signals.

An implementation can be accomplished either as a switched-mode or linear amplifier as long as a disturbance at the frequency of the eddy current measurement injected test signal is avoided. Clearly, for a minimization of the overall system losses, a switched amplifier would be preferred. However, in a first prototype design focusing primarily on the concept verification of the hybrid bearing approach, a linear amplifier is employed because of its simple implementation and the avoidance of switching frequency harmonics, which could be a potential disturbance source for the highly sensitive displacement measurement.

A basic implementation using a linear amplifier is given in Figure 4.16. The circuit is basically a low pass voltage controlled current source taking the winding reference current represented by a voltage signal $u_{ref} \propto i_{a,ref}$ as an input. The impedance Z represents the impedance of the winding and displacement measurement circuit seen by the power amplifier according the presented parallel and serial self-sensing topologies. A shunt resistor R_{shunt} is used for current measurement. When assuming the feedback resistor $R_{fb} \gg R_{shunt}$, the Laplace transfer function from u_{ref} to the winding current i_a or i_b can be given as

$$\frac{i_{a,b}}{u_{ref}} \approx \frac{R_{fb}}{R_{in}} \frac{1}{R_{shunt} + s \cdot C R_{fb} (Z + R_{shunt})}, \quad (4.69)$$

which has the form of a first order lowpass filter.

The power amplifier for phase B is constructed correspondingly. There, a lowpass characteristic is required primarily to avoid high frequency disturbances coupled capacitively to the search coils of phase A .

4.3.5 Self-Sensing Angular Position Measurement

For the transformation of the damper reference currents i_{dq} in dq coordinates to the phase currents i_{ab} , the angular rotor position γ will be needed. Recalling the transformation from i_{dq} to i_{ab} as

$$i_{ab} = i_{dq} \cdot e^{-j\gamma}, \quad (4.70)$$

with

$$i_a = \Re\{i_{ab}\} = i_d \cos \gamma + i_q \sin \gamma \quad (4.71)$$

$$i_b = \Im\{i_{ab}\} = -i_d \sin \gamma + i_q \cos \gamma \quad (4.72)$$

it is seen that the angular rotor position in terms of $\cos \gamma$ and $\sin \gamma$ are actually needed. These signals can be derived from the back-EMF voltage which occurs on the mid-tapping of each coil pair L_{x+} , L_{x-} and L_{y+} , L_{y-} during rotation.

A diagram of the measurement circuit needed to extract these signals is given in Figure 4.17. The induced voltage occurring at L_{x+} and L_{y+} with the polarity indicated by the arrow are given by

$$u_{x,i} = -\Omega \Phi_{xy} \sin \gamma \quad (4.73)$$

$$u_{y,i} = \Omega \Phi_{xy} \cos \gamma, \quad (4.74)$$

where Φ_{xy} denotes the flux linkage of a single coil and $\gamma = \Omega t$. For the straight winding as defined in Section 4.1.2 the flux linkage can be derived from Lorentz force integration and the principle of energy conservation and can be given as

$$\Phi_{xy} = \sqrt{2} \sin \frac{\pi}{8} \cdot \frac{NB_{rem}LR_1^2}{2\pi(R_4^2 - R_3^2)} \left(R_4 - R_3 + \frac{R_4^3 - R_3^3}{3R_5^2} \right). \quad (4.75)$$

For a coil pair, the voltages occur with opposite signs regarding their winding sense which is indicated by the point. Hence in the series connection, the induced voltages are canceled.

The induced voltage cannot simply be measured at the terminal connection of the respective coil because of the damper current causing a voltage drop due to the winding's resistance and inductance. These current dependent contributions need to be eliminated in order to obtain clean signals for the coordinate transform and an unconstrained control. Therefore, the voltage is measured in respect to an artificial

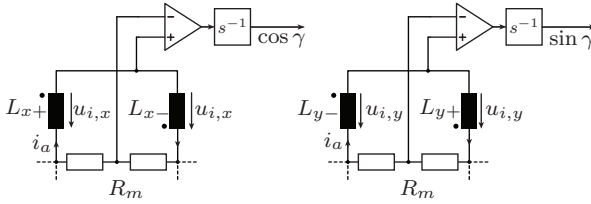


Figure 4.17: Circuit for angular rotor position measurement based on the back-EMF voltage occurring at the mid-point of the series connection of a coil pair L_{x+} , L_{x-} and L_{y+} , L_{y-} . The dashed lines indicate the integration in the eddy current self-sensing circuit which can be of the serial or parallel type.

mid-potential generated by means of a resistive voltage divider with equal resistors R_m . The subsequent integration yields the signals

$$\int u_{x,i} dt = \Phi_{xy} \cdot \cos \gamma \quad (4.76)$$

$$\int u_{y,i} dt = \Phi_{xy} \cdot \sin \gamma, \quad (4.77)$$

which are directly proportional to $\cos \gamma$ and $\sin \gamma$ respectively. It is seen that the integration yields signals with constant amplitude independent of the rotational speed Ω . Hence without further processing, they can be used for the coordinate transformation.

4.3.6 Concluding Remarks

Two possible circuit topologies have been presented enabling a self-sensing eddy current based displacement measurement. The parallel type topology is found more robust concerning crosstalk of the damper current to the displacement measurement and results in smaller dimensions of the required passive components. Combined with the self-sensing back-EMF based angular rotor position measurement, no dedicated sensors need to be installed in an implementation.

Though, in order to achieve both displacement and angular position self-sensing, auxiliary circuits have been proposed, which is not exactly in accordance with the usual denomination of a self-sensing system. Therefore some explanation is needed for the use of the term self-sensing in this work.

In a pure self-sensing system, sensors are completely avoided without the use of additional components in order to reduce the number of components. The benefits then are claimed to have a system of lower complexity, higher robustness and lower cost. Although the self-sensing approach is not fully in accordance with the original designation of self-sensing due to the additional circuitry, the similar benefits of the present self-sensing magnetic damper are evident. It allows for a simplified and compact mechanical construction of the machine and moreover, by avoiding the installation of sensors, a shorter and lighter rotor can be realized, enabling higher rotational speeds.

Chapter 5

Control

On the example of the rotor for a prototype permanent magnet machine employing a hybrid gas-magnetic bearing system, the dynamic stability of the rotor-bearing system with and without the employment of active magnetic damping is analyzed. The stability analysis is based on a rigid rotor model, which is detailed at first. Stabilization of the rotor-bearing system by means of feedback control using a basic D-controller is discussed and numerical results are presented. Furthermore, the need for notch filters is discussed, which are used to suppress a controller response at the synchronous frequency as well as at the frequency of the rotor's first bending mode.

5.1 Rotor Dynamic Modeling

5.1.1 Rigid Rotor Model

A rotor dynamic model is required for the study of the dynamic behavior of the rotor supported by gas bearings with and without the use of active magnetic damping. For a simplified analysis, the rotor is modeled as a rigid body. Therewith, most of the phenomena regarding gas bearing stability can be analyzed.

The radial position of the rigid rotor can be described by the displacement of the rotor's center of gravity (CG) and two inclination angles. A drawing of the rotor supported by the hybrid bearing system consisting of two gas bearings and two magnetic dampers is given in

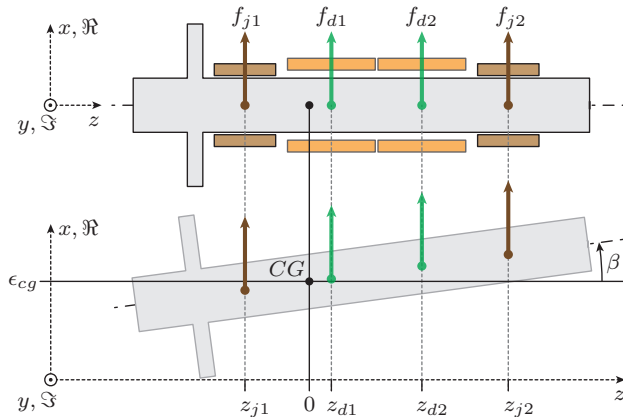


Figure 5.1: Rotordynamic model of rigid rotor with radial rotor motion defined by its center of gravity displacement ϵ_{cg} and inclination angle β . Gas bearings are indicated in brown and AMD actuator windings in orange color.

Figure 5.1. Assuming rotational symmetry of the rotor in respect to its primary axis of rotation z , a complex notation can be used. Hence the rotor position is defined by a complex center of gravity displacement ϵ_{cg} and a complex inclination angle β such that the displacement of the rotor in x and y direction at a location z can be written as

$$\epsilon_x(z) = \Re\{\epsilon_{cg}\} + z \tan(\Re\{\beta\}) \quad (5.1)$$

$$\epsilon_y(z) = \Im\{\epsilon_{cg}\} + z \tan(\Im\{\beta\}). \quad (5.2)$$

Assuming small inclination angles, the complex displacement which is defined as $\epsilon = \epsilon_x + j\epsilon_y$ can be approximated as

$$\epsilon(z) \approx \epsilon_{cg} + z \cdot \beta \quad (5.3)$$

As already introduced for the gas bearing forces in Section 3.3 and the magnetic forces in Section 4.1.2, a complex representation for the forces acting on the rotor according the definition $f = f_x + jf_y$ is used. The gas bearing forces denoted as f_{j1} and f_{j2} act at the locations z_{j1} and z_{j2} and damper forces denoted as f_{d1} and f_{d2} act at the locations z_{d1} and z_{d2} .

The governing equations of motion for a rigid rotor are given in [21]. With the above definitions, they can be written as

$$m\ddot{\epsilon}_{cg} = f_{res} \quad (5.4)$$

$$I_{x0}\ddot{\beta} - j\Omega I_{z0}\dot{\beta} = T_{res}. \quad (5.5)$$

where f_{res} and T_{res} denote the resultant force and torque acting on the rotor, I_{x0} denotes the inertia of the rotor about the x axis¹ and I_{z0} the inertia about the z axis. The term $j\Omega I_{z0}\dot{\beta}$ describes a cross coupling torque between the x and y axis, respectively between the real and imaginary axis, which originates from gyroscopic forces.

For the given rotor definition, the resultant force and torque in respect to the center of gravity are

$$f_{res} = f_{j1} + f_{j2} + f_{d1} + f_{d2} + f_{\delta} \quad (5.6)$$

$$T_{res} = z_{j1}f_{j1} + z_{j2}f_{j2} + z_{d1}f_{d1} + z_{d2}f_{d2} + T_{\delta} \quad (5.7)$$

where f_{δ} and T_{δ} are an arbitrary disturbance force and torque respectively.

State Space Representation

The equations of motion for the rotor system can be rewritten in a state space representation using the state vector

$$\xi_r = [\epsilon_{cg} \quad \dot{\epsilon}_{cg} \quad \beta \quad \dot{\beta}]^T \quad (5.8)$$

as

$$\dot{\xi}_r = A_r \xi_r + B_r f + B_{r\delta} \begin{bmatrix} f_{\delta} \\ T_{\delta} \end{bmatrix} \quad (5.9)$$

where the system matrices are

$$A_r = \begin{bmatrix} 0 & 1 & 0 & 0 \\ 0 & 0 & 0 & 0 \\ 0 & 0 & 0 & 1 \\ 0 & 0 & 0 & j\frac{I_{z0}}{I_{x0}}\Omega \end{bmatrix}, \quad (5.10)$$

¹which is under the given assumption of rotational symmetry equal to the inertia I_{y0} about the y axis

$$B_r = \begin{bmatrix} 0 & 0 & 0 & 0 \\ \frac{1}{m} & \frac{1}{m} & \frac{1}{m} & \frac{1}{m} \\ 0 & 0 & 0 & 0 \\ \frac{z_{j1}}{I_{x0}} & \frac{z_{j2}}{I_{x0}} & \frac{z_{d1}}{I_{x0}} & \frac{z_{d2}}{I_{x0}} \end{bmatrix} \quad \text{and} \quad B_{r\delta} = \begin{bmatrix} 0 & 0 \\ \frac{1}{m} & 0 \\ 0 & 0 \\ 0 & \frac{1}{I_{x0}} \end{bmatrix} \quad (5.11)$$

and the force vector is defined as

$$f = [f_{j1} \quad f_{j2} \quad f_{d1} \quad f_{d2}]^T. \quad (5.12)$$

The displacements at the location of the gas bearings and the magnetic dampers are obtained as

$$\epsilon = [\epsilon(z_{j1}) \quad \epsilon(z_{j2}) \quad \epsilon(z_{d1}) \quad \epsilon(z_{d2})]^T = C_r \xi_r \quad (5.13)$$

where

$$C_r = \begin{bmatrix} 1 & 0 & z_{j1} & 0 \\ 1 & 0 & z_{j2} & 0 \\ 1 & 0 & z_{d1} & 0 \\ 1 & 0 & z_{d2} & 0 \end{bmatrix}. \quad (5.14)$$

The state space representation of the rotor model will serve as a basis for the stability analysis of the rotor-bearing system. Yet, the gas bearing and damper forces were treated as independent variables; the inherent displacement dependency of the gas bearing force represented by the gas bearing's dynamic stiffness and the damper forces defined by the applied feedback control law will finally yield a closed loop system which is subject of a more detailed analysis in the following.

Closed Loop System

The gas bearings and the active magnetic dampers can be seen as a feedback controllers taking the rotor displacement vector ϵ as an input and providing the force vector f as an output.

The state vector of the feedback system merged from the individual systems of the gas bearings and the magnetic dampers can then be defined as

$$\xi_{jd} = [\xi_{j1} \quad \xi_{j2} \quad \xi_d] \quad (5.15)$$

which incorporates the state vectors of the two gas bearings ξ_{j1} and ξ_{j2} and the state vector of the damping controller ξ_d . The system equations are given by

$$\dot{\xi}_{jd} = A_{jd} \cdot \xi_{jd} + B_{jd} \cdot \epsilon \quad (5.16)$$

$$f = C_{jd} \cdot \xi_{jd} + D_{jd} \cdot \epsilon, \quad (5.17)$$

where the merged system matrices are

$$\begin{aligned}
 A_{jd} &= \begin{bmatrix} A_j & 0 & 0 \\ 0 & A_j & 0 \\ 0 & 0 & A_d \end{bmatrix}, B_{jd} = \begin{bmatrix} B_j & 0 & 0 \\ 0 & B_j & 0 \\ 0 & 0 & B_d \end{bmatrix} \\
 C_{jd} &= \begin{bmatrix} C_j & 0 & 0 \\ 0 & C_j & 0 \\ 0 & 0 & C_d \end{bmatrix}, D_{jd} = \begin{bmatrix} D_j & 0 & 0 \\ 0 & D_j & 0 \\ 0 & 0 & D_d \end{bmatrix}. \quad (5.18)
 \end{aligned}$$

The system matrices A_j , B_j , C_j and D_j refer to the dynamic system description of a single gas bearing as derived in Section 3.6.3. The matrices A_d , B_d , C_d and D_d describe the damper dynamic behavior which will be given later by the damper control law.

Closing the loop by connecting the displacement output ϵ of the rotor system to the input of the bearing and damper feedback system and connecting the resulting force vector f back to the rotor system force input yields

$$\begin{bmatrix} \dot{\xi}_r \\ \dot{\xi}_{jd} \end{bmatrix} = A_{cl} \cdot \begin{bmatrix} \xi_r \\ \xi_{jd} \end{bmatrix} + B_{cl} \cdot \begin{bmatrix} f_\delta \\ T_\delta \end{bmatrix}, \quad (5.19)$$

where the closed loop system matrices are

$$A_{cl} = \begin{bmatrix} A_r + B_r D_{jd} C_r & B_r C_{jd} \\ B_{jd} C_r & A_{jd} \end{bmatrix} \quad \text{and} \quad B_{cl} = \begin{bmatrix} B_r \delta \\ 0 \end{bmatrix}. \quad (5.20)$$

As is known from the theory of LTI systems, the poles of the closed loop system are given by the eigenvalues of the system matrix

$$p_{cl} = \text{eig}(A_{cl}). \quad (5.21)$$

For stability, it will be required that all poles are located in the left half of the complex plane (LHP).

5.1.2 Rotor Gas-Bearing System

First, the system composed of the rigid rotor and two gas bearings without active magnetic damping is studied. For the analysis, the rotor of the finally constructed prototype machine is considered, which parameters are given in Table 5.1. Using a state space representation of the calculated transfer function model of the Rayleigh step journal

Quantity	Symbol	Value
Bearing location 1	z_{j1}	- 13.2 mm
Bearing location 2	z_{j2}	20.8 mm
Damper location 1	z_{j2}	-2.2 mm
Damper location 2	z_{j2}	9.8 mm
Inertia z Axis	I_{z0}	$0.11 \cdot 10^{-6} \text{ kgm}^2$
Inertia x Axis	I_{x0}	$3.26 \cdot 10^{-6} \text{ kgm}^2$

Table 5.1: Parameters of prototype rotor used for rotor dynamic analysis.

bearing $c_j(s)$ from Section 3.8, the poles of system matrix A_{cl} can be calculated. Sweeping the rotational speed from 20 krpm to 500 krpm, the closed loop poles of the rotor bearing system with the nominal gas bearing design are calculated for each speed. The resulting root loci are depicted in Figure 5.2a). Four relevant poles exist for the closed loop system, namely combinations of forward and backward whirling in conical and translational motion. A clear separation between the conical and the translational mode cannot be made, as they occur partly combined.

A further mode which is sometimes encountered with gas bearing systems is the so-called air-hammer mode. It occurs due to the delay of pressure build-up within the fluid film and is mostly related to externally pressurized gas bearings. With self-acting gas bearings, this effect is usually not observed and hence the according poles are located far in the LHP.

The four relevant poles move as the rotational speed is increased, mainly due to the speed dependent dynamic properties of the gas bearing (see Figure 3.15). While the forward whirl modes proceed into the LHP, the backward whirl modes approach the imaginary axis and eventually become unstable.

Assuming given fabrication tolerances of the bearings minimum film height $h_2 = 8 \pm 2 \mu\text{m}$ and the step height $h_1 - h_2 = 5 \pm 2 \mu\text{m}$, the case of $h_2 = 10 \mu\text{m}$ and $h_1 - h_2 = 7 \mu\text{m}$ represents a worst case concerning stability. Figure 5.2b) shows the root loci for the tolerance afflicted gas bearing design. It can be seen that the poles have shifted further towards the RHP and the system will become unstable at already lower speeds. According to the calculation, instability onset is expected at

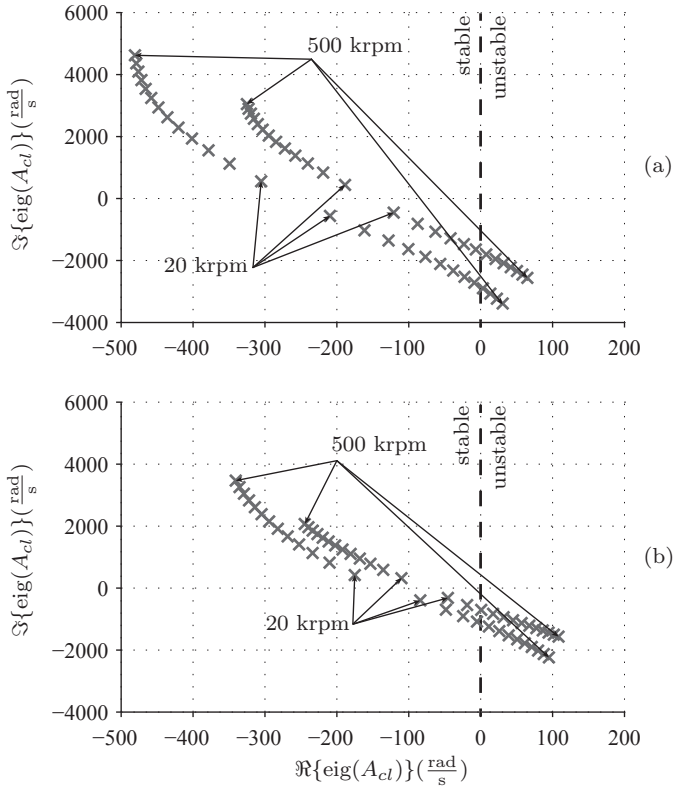


Figure 5.2: Speed dependent root locus plot of the relevant closed loop poles of the rotor gas bearing system with the nominal gas-bearing design (a) and a gas bearing design afflicted with tolerances of $\pm 2\mu\text{m}$ (b).

around 100 krpm for the tolerance afflicted design instead of 220 krpm for the nominal design.

The example shows the high susceptibility of a gas bearing system to fabrication tolerances. In a real system where tolerances and misalignment stack, performance can be expected to be further degraded.

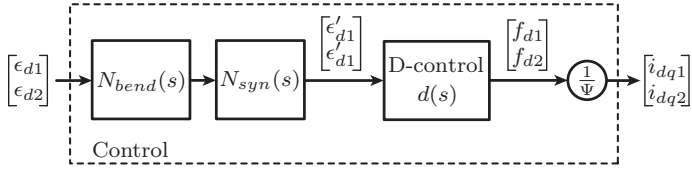


Figure 5.3: Block diagram of the feedback control incorporating a D-controller $d(s)$ and notch filters for synchronous response suppression $N_{syn}(s)$ and bending mode response suppression $N_{bend}(s)$.

5.2 D-Controller

A block diagram of the controller is shown in Figure 5.3. It takes the displacements at the damper locations $[\epsilon_{d1} \ \epsilon_{d2}]^T$ as an input and provides the dq reference currents for the two dampers $[i_{dq1} \ i_{dq2}]^T$ as an output. Besides the actual controller $d(s)$ containing the control law for stabilization of the rotor supported by the gas bearings, the controller block diagram contains also two notch filters. The notch filter $N_{sys}(s)$ is used to suppress the synchronous signal component of the displacement measurement resulting from residual unbalance and possible rotor surface non-uniformity. $N_{bend}(s)$ is needed to suppress a controller response at the frequency of the first bending mode. The notch filter blocks are discussed in Section 5.3 and Section 5.4. For the analysis of the $d(s)$, the notch filter blocks are assumed transparent, i.e. $[\epsilon'_{d1} \ \epsilon'_{d2}]^T = [\epsilon_{d1} \ \epsilon_{d2}]^T$. Furthermore, current control is assumed ideal, such that the controller's reference forces can be assumed the actual damper forces.

In the previous section, it was seen that the bearing's behavior varies considerably depending on the actual film dimensions which are affected by production deviations. In a gas bearing system, the bearings properties may therefore be only roughly known. Thus, a stabilizing feedback controller must be designed able to cope with the uncertainty of the gas bearing's dynamics.

A possible stabilizing controller is the D-controller which provides forces proportional to translational velocity of the rotor and therewith dissipates energy of the whirling motion. Ideally, the two damper forces

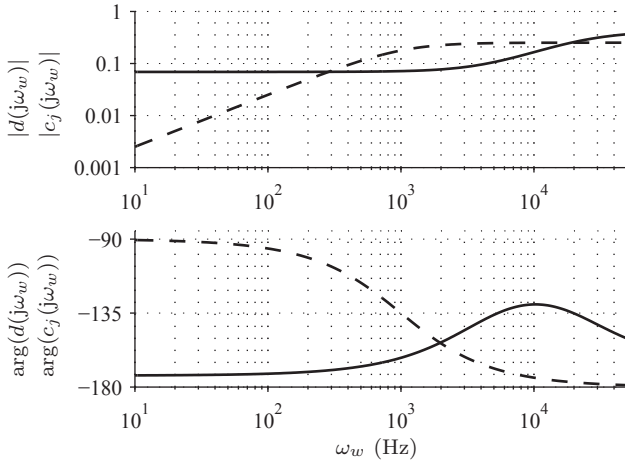


Figure 5.4: D-controller frequency responses (dashed line) with $K_d = 20 \frac{\text{Ns}}{\text{m}}$, $p_1 = 6.3 \cdot 10^3 \frac{\text{rad}}{\text{s}}$, and nominal design gas bearing frequency response at 500 krpm for comparison (solid line).

are

$$\begin{bmatrix} f_{d1} \\ f_{d2} \end{bmatrix} = d(s) \cdot \begin{bmatrix} \epsilon_{d1} \\ \epsilon_{d2} \end{bmatrix}, \quad (5.22)$$

where the controller transfer function is $d(s) = K_d \cdot s$ with K_d being the damping factor. For an implementation, it will be required to add a low pass characteristic by means of additional poles p_k . Accordingly, the controller takes the form

$$d(s) = K_d \cdot \frac{s}{\prod_k \left(\frac{s}{p_k} + 1 \right)} \quad (5.23)$$

For the bearing rotor system analyzed in Section 5.1.2, a stabilizing D-controller with a single additional pole can be designed. The resulting transfer function with $K_d = 20 \frac{\text{Ns}}{\text{m}}$ and $p_1 = 6.3 \cdot 10^3 \frac{\text{rad}}{\text{s}}$ is shown in the bode diagram in Figure 5.4. For comparison of the order of magnitudes, the frequency response $c_j(s)$ of the nominal design gas bearing at 500 krpm is also shown.

A root locus plot of the resulting closed loop system with the tolerance afflicted bearing design as a worst case for stabilization is shown in Figure 5.5. Comparing to the root locus plot of the non-stabilized

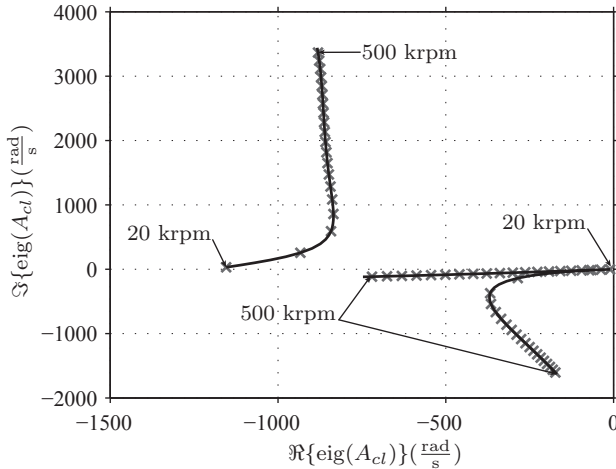


Figure 5.5: Speed dependent root locus plot for the stabilized system.

system of Figure 5.2b), all unstable poles have been shifted into the LHP.

For low speeds, the damper is strong compared to the restoring force of the gas bearing, hence poles exist close to the origin, i.e. with the low stiffness of the gas bearing, a displaced rotor will converge only slowly to the bearing's center as motion is heavily damped by the magnetic damper. For higher speeds, the gas bearing gains strength and the poles move further into the LHP. Three of the originally four relevant modes have moved moderately into the LHP, the fourth mode is now far in the LHP and is therefore not depicted.

Stabilization of the bearing with the worst case dimensional deviations requires higher damping than the nominal bearing design. Hence for all bearing variations within the given tolerance, stability will be better. With the nominal design, approximately half of the gain K_d would be sufficient for stabilization. Therefore, with a controller designed for the worst case deviations, the poles are located even further in the LHP.

5.3 Synchronous Whirling

Because of the existence of residual rotor imbalance, rotational speed synchronous whirling motion is visible on the displacement measurement signal. A further contribution of a synchronous component results from rotor surface non-uniformity. In order to avoid high and unnecessary damper currents resulting from synchronous components on the measurement signal, a notch filter $N_{syn}(s)$ suppressing the synchronous frequency component is employed.

The notch filter essentially contains a zero at the frequency of the rotational speed and therewith makes the controller blind at the synchronous frequency. Thus, no control action is taken at this frequency. In order to employ such a filter, no unstable pole must exist in the vicinity of the canceled frequency; otherwise, stability of the closed loop system is no more given.

A Campbell diagram of the closed loop system with the nominal bearing design is shown in Figure 5.6. It plots the imaginary parts of the relevant poles of the closed loop system against the rotational speed. A crossing with the identity would indicate a condition, where stability could be compromised. However, as the poles are always below the identity, no such condition exists. The notch filter suppressing the rotational frequency component of the feedback control will therefore pose no problem to the closed loop stability of the bearing rotor system.

An implementation of the synchronous notch filter $N_{syn}(s)$ is given in Figure 5.7. It uses the signals $\cos \gamma$ and $\sin \gamma$, where under rotation $\gamma = \Omega t$. Thus, the filter frequency is automatically adapted as the rotational speed varies. The signals $\cos \gamma$ and $\sin \gamma$ are already available and do not need to be extra generated, see Section 4.3.5.

For a constant rotational speed Ω , the transfer function of $N_{syn}(s)$ can be written as

$$N_{syn}(s) = \frac{s^2 + \Omega^2}{s^2 + K_n \cdot s + \Omega^2}, \quad (5.24)$$

where with the factor K_n , the convergence speed can be set, respectively the width of the stop band. If in a given application the rotational speed change is slow, K_n can be chosen small, yielding a very selective frequency cancellation. If fast convergence is needed, K_n can be chosen large.

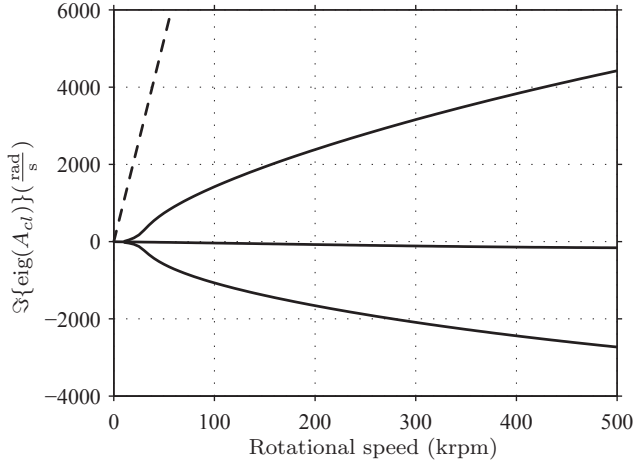


Figure 5.6: Campbell diagram of closed loop system with the nominal bearing design. The dashed line indicates the rotational synchronous frequency (identity).

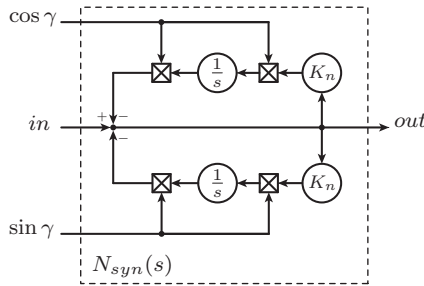


Figure 5.7: Implementation of synchronous notch filter $N_{syn}(s)$ based on the signals $\cos \gamma$ and $\sin \gamma$ with $\gamma = \Omega t$.

5.4 Rotor Bending Mode

In order to not excite the rotor's first bending mode due to high controller feedback gains and an unavoidable controller phase lag at the bending mode's frequency, a further notch filter $N_{bend}(s)$ is introduced.

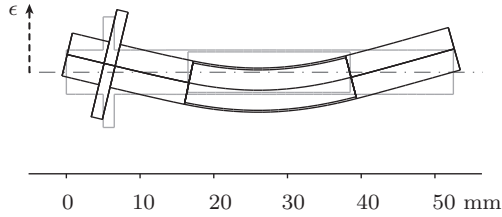


Figure 5.8: First bending mode of the prototype steel rotor calculated at $f_{bend} = 6.2$ kHz

The filter suppresses the controller's response at this frequency. Because of the small ratio of the inertia in the principle axis to the transverse axis I_{z0}/I_{x0} resulting in small gyroscopic forces and the relatively low bearing stiffness compared to the rotor bending stiffness, the resonant frequencies are widely speed independent. Thus, the notch filter can be designed for a constant resonant frequency in the entire operating speed range.

The bending mode can be calculated based on a one-dimensional numerical model of the Euler-Bernoulli beam according [1]. For the bending mode calculation, a free rotor is assumed, neglecting gas bearing support. For the prototype rotor with a steel sleeve, a frequency of $f_{bend} = 6.2$ kHz results. A drawing of the bending mode's shape is given in Figure 5.8.

The transfer function of the bending mode notch filter has the same form as the transfer function given for $N_{syn}(s)$ in the previous section. It can be given as

$$N_{bend}(s) = \frac{s^2 + \omega_{bend}^2}{s^2 + K_n \cdot s + \omega_{bend}^2}, \quad (5.25)$$

where again K_n is used to determine the convergence speed, respectively width of the stop band. $\omega_{bend} = 2\pi f_{bend}$ denotes the bending mode's resonant frequency. As ω_{bend} is a constant, the filter can be implemented as an ordinary second order filter.

Chapter 6

Hardware Prototype and Experimental Results

In order to verify the feasibility of the gas-magnetic hybrid bearing approach for future industrial applications, a prototype permanent magnet machine employing the hybrid bearing system is constructed. The electromagnetic design of the machine is detailed and the machine's loss models are summarized. Furthermore, the prototype implementation of the gas bearings, AMD windings and damper electronics are detailed.

The sensitivity and resolution of the implemented eddy current based displacement self-sensing method are evaluated and actuator cross talk, which is a limiting factor for feedback control, is analyzed. Experimental results are given for non-stabilized and stabilized operation; stable operation is demonstrated by means of active magnetic damping to a speed of up to 210 krpm. By means of a rundown-experiment, the system losses are identified and using a spectral analysis of the recorded displacement signals, the dynamics of the gas bearings are located.

6.1 System Integration

A drawing of the machine prototype with the hybrid gas-magnetic bearing is shown in Figure 6.1. The gas bearings are arranged close to the machine's active region in order to keep the rotor short. The bearing bushings are supported on O-rings in order to enable self-aligning of the bushings. The damper windings are integrated into the active region

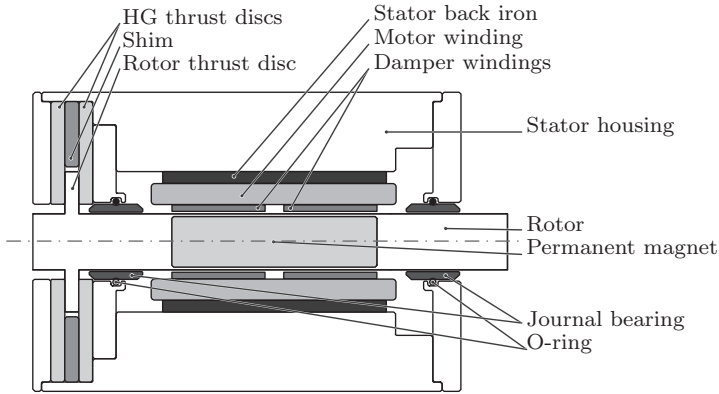


Figure 6.1: Section view of prototype machine with the hybrid gas-magnetic bearing concept.

of the machine as already discussed in Section 4.1. A solid steel stator housing provides the structural strength. Axial rotor support is given by a thrust bearing implemented as a disc on the rotor which is kept in place between two herringbone grooved (HG) thrust discs.

6.1.1 Electrical Machine

The design of the electrical machine follows closely the prior work [74,1], where a highly efficient permanent magnet machine design is proposed for ultra-high rotational speeds. The electric machine is designed as a slotless type machine as already presupposed in Section 4.1 for the integrated realization of the heteropolar AMD winding.

The key attributes of the high speed electrical machine design can be traced back to the minimization of losses at high rotational speeds. They are summarized as follows:

- ▶ The slotless design avoids slot harmonic induced losses which otherwise with a slotted design would become dominant at high rotational speeds.
- ▶ The air-gap winding is exposed to the alternating permanent magnet field of the permanent magnet rotor, which induces eddy currents in the winding conductors (proximity losses). Thus, litz-wire

is used to minimize the permanent magnet field induced eddy current losses in the winding.

- Fine laminated amorphous iron is used for the stator back iron in order to obtain low losses at high rotational speeds.

A robust rotor construction is required to cope with rotor dynamics and the high centrifugal stresses at high rotational speeds. Thus, the brittle permanent magnet is encased into a high strength metallic sleeve such as steel or titanium by using an interference fit [1].

In the present machine, the rotor is constructed from stainless steel 1.4301, which has superior sliding properties needed for the gas bearing during start and stop. However, as the first bending mode is calculated at 6.2 kHz, a maximum corresponding rotational speed of 372 krpm will be allowable. In order to reach higher speeds, a titanium version of the rotor will be needed with according coatings in order to improve its sliding properties. For a titanium rotor construction of the same dimensions, the bending mode is calculated at 8.6 kHz, corresponding to a critical rotational speed of 516 krpm.

Machine Torque

The prototype electrical machine is designed for proof of the hybrid gas-magnetic bearing concept. Therefore, the prototype will run idle without the load of a typical application such as a turbo-compressor. The machine needs only to provide torque to cover the machine losses and the bearing friction losses. A thermal analysis of the machine design is therefore not considered. For easiest possible handling and assembly, the dimensions of the rotor are chosen as large as centrifugal stresses and rotor dynamics within safe limits allow, resulting in a machine size which would in an application deliver an estimated power of 200 W to 500 W at 500 krpm depending on the cooling conditions and the realized winding copper filling factor. The data of the constructed machine is collected in Table 6.1.

Two possible air-gap winding types are considered for the machine prototype, namely the skewed type and the straight type winding. It is found for the skewed type three phase winding with one pole pair, that besides a driving torque T_z in the principal axis also a transverse torque T_{xy} is generated in the perpendicular plane which results from the skewed arrangement of the conductors [87]. While T_z is the intended machine torque, the transverse torque T_{xy} is parasitic and needs to be

Quantity	Symbol	Value
Permanent magnet radius	R_1	2.75 mm
Rotor retaining sleeve radius	R_2	3 mm
Damper winding inner radius	R_3	3.25 mm
Motor winding inner radius	R_4	3.7 mm
Stator back iron inner radius	R_5	6 mm
Stator back iron outer radius	R_6	7.5 mm
Active length	l_{pm}	22 mm
Stator resistance		0.2 Ω
Stator inductance		4 μH
Permanent magnet flux linkage		0.2 mVs

Table 6.1: Prototype machine data.

compensated by the bearing system. The ratio of transverse torque to driving torque T_{xy}/T_z is analyzed and measured in [87]. The resulting torque ratio depending on the machine dimensions is plotted in Figure 6.2. For the present machine, a ratio of $T_{xy}/T_z \approx 0.5$ can be expected when using a skewed winding. In order to minimize any possible excitations forces which might interfere with the bearing system, the straight type winding, which does not produce a transverse torque, is chosen for the prototype machine.

Analytical expressions for the magnetic field distribution resulting from the permanent magnet on the rotor are derived in [74]. The magnetic field distribution originating from the permanent magnet on the rotor is shown in Figure 6.3. The stator back iron outer radius R_6 is chosen not to saturate the material. The maximum occurring flux density in the stator back iron is 1.05 T, which is below the saturation flux density of 1.2 T for the amorphous iron material Metglas 2605SA1.

According [74], the machine torque is

$$T_e = \sqrt{2}\pi k_w k_{cu} J K_B l_{pm} R_5^3 \left(\frac{4}{3} - \frac{R_4}{R_5} - \frac{R_4^3}{3R_5^3} \right), \quad (6.1)$$

where k_w is the fundamental wave winding factor, k_{cu} is the copper filling factor, J is the rms current density in the conductors and l_{pm} is the machines active length. The factor K_B can be given as

$$K_B \approx \frac{B_{rem} R_1^2}{2R_5^2}, \quad (6.2)$$

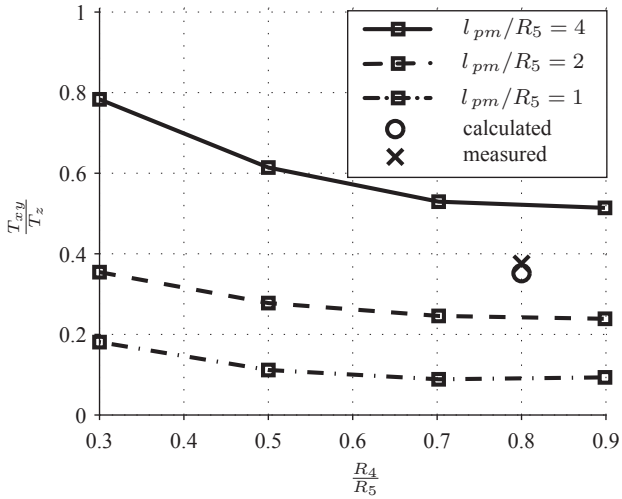


Figure 6.2: Ratio of transverse torque T_{xy} to to drive torque T_z of the three phase one pole pair skewed motor winding depending on the machine dimensions.

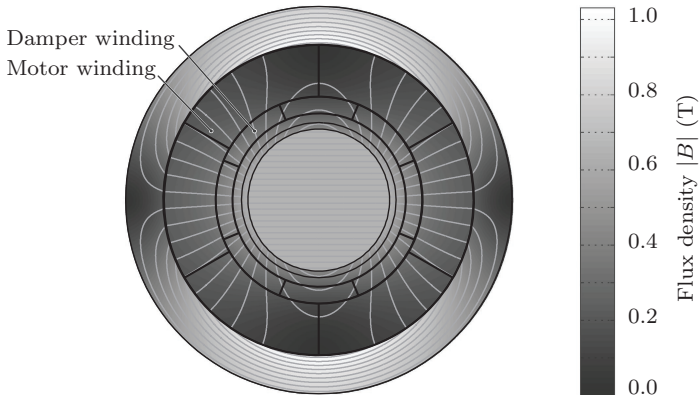


Figure 6.3: Magnetic flux density and field lines of the prototype permanent magnet machine.

when assuming the relative permeability of the stator back iron $\mu_{r,fe} \approx \infty$ and the relative permeability of the permanent magnet $\mu_{r,pm} \approx 1$.

Machine Losses

The loss models for the present machine type are detailed in [74]. The machine losses are composed of winding conduction losses, winding proximity losses, iron losses and air friction losses.

Copper Losses. The winding losses are composed of copper conduction losses $P_{cu,s}$ due to the stator resistance and the drive current I as well as proximity losses $P_{cu,p}$ originating from the alternating magnetic field of the rotating permanent magnet rotor causing eddy currents in the winding conductors. According [74], the copper losses can be calculated as

$$P_{cu} = P_{cu,s} + P_{cu,p} = F_{cu}I^2 + \frac{G_{cu}H^2}{\sigma_{cu}}, \quad (6.3)$$

where H is the magnetic field strength in the winding, σ_{cu} is the copper electrical conductivity and the coefficients F_{cu} and G_{cu} are functions of the conductor material, conductor geometry and the rotational frequency Ω . F_{cu} and G_{cu} can be obtained following [88].

Iron Losses. The iron losses are governed by the magnetic field distribution in the stator back iron. From [74] it is known that the field distribution in the back iron of the present machine concept is a pure sinusoidal function of the circumferential coordinate. Hence the time varying field seen by the stator back iron is also purely sinusoidal. Therefore, the Steinmetz equation known for empirical loss modeling of magnetic materials can be applied without further modifications. The iron losses can then be calculated by

$$P_{fe} = \int_{V_{fe}} c_{fe} f^{\alpha_{fe}} \cdot \hat{B}^{\beta_{fe}} dV, \quad (6.4)$$

where $f = \left(\frac{\Omega}{2\pi}\right)$ is the frequency of the rotational speed, \hat{B} is the peak flux density in time and c_{fe} , α_{fe} and β_{fe} are the Steinmetz coefficients which depend on the employed iron material. For the present machine, Metglas 2605SA1 amorphous iron is used with the Steinmetz coefficients given in Table 6.2.

Quantity	Symbol	Value
Steinmetz coefficient	c_{fe}	0.94 W/m ²
Steinmetz coefficient	α_{fe}	1.53 (f in Hertz)
Steinmetz coefficient	β_{fe}	1.72 (B in Tesla)

Table 6.2: Steinmetz coefficients for Metglas 2605SA1.

Air Friction Losses. The air friction losses of the rotor under rotation can be calculated based on empirical equations [89]. The air friction losses of a cylinder with radius R_2 and length l rotating at a speed Ω are

$$P_{air} = c_f \pi \rho \Omega^3 R_2^2 l \quad (6.5)$$

where ρ is the density of surrounding air and c_f is a friction coefficient depending on the cylinder radius, air-gap and the fluid flow regime which can range from laminar flow to fully turbulent flow.

6.1.2 Magnetic Damper Winding

The AMD winding is implemented according Section 4.3 as a two phase winding with two pole pairs to produce the damper forces and with the required additional tappings for eddy current position self-sensing and angular rotor position detection. The winding is realized as a double layer flexible printed circuit (FPC), which is rolled three times to be installed into the machine. The FPC winding is made from a 25 μm thick polyimide substrate with 35 μm thick copper on each side. Together with the coverlays, a total thickness of 150 μm is obtained. A picture of the winding prototype is shown in Figure 6.4. The winding specifications are given in Table 6.3

A rhombic type winding is used for the FPC implementation. A single winding turn consist of a copper trace on the top layer as well as of a trace on the bottom layer, hence two via connections are needed for each turn. The via bore and pad diameters are constrained to 100 μm and 300 μm respectively by the manufacturing process. In order to minimize the DC winding resistance, the copper trace width should be chosen maximal and hence equal to the via pad diameter. However with such wide traces, high proximity effect losses induced by the permanent magnet field at high speed would be the consequence. As a compromise, the width of the copper traces is chosen 170 μm resulting in a decreased

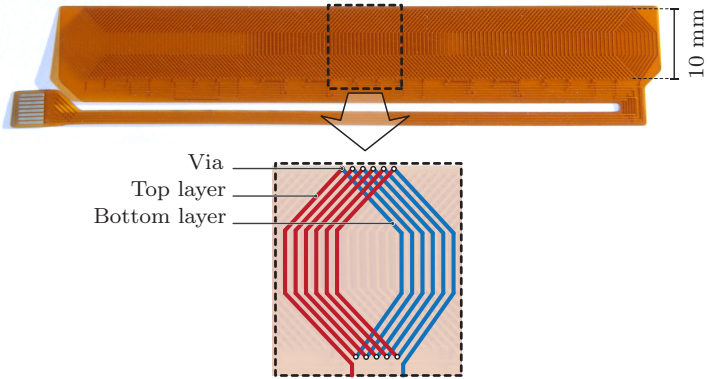


Figure 6.4: AMD winding implemented as a double layer flexible printed circuit.

Table 6.3: Damper winding specifications

Quantity	Symbol	Value
Inner radius	R_3	3.25 mm
Outer radius	R_4	3.7 mm
Damper active length	l_d	10 mm
Number of turns (per coil)	N_d	18
Damper flux linkage	Ψ	0.3 N/A
Inductance phase A (10 kHz)	L_a	$4 \times 2.6 \mu\text{H}$
Inductance phase B (10 kHz)	L_b	$11.6 \mu\text{H}$
Resistance phase A		$4 \times 3.5 \Omega$
Resistance phase B		9.0Ω

copper filling factor. Higher copper filling factors without an increase of proximity effect losses could only be achieved when allowing smaller via-pad diameters.

Three electrical connections are needed for both coil pairs of phase A. Phase B requires two connections. Hence for the eight connections in total, a standard 8-way, 0.5 mm pitch flexible flat cable (FFC) connector is used to connect the winding to the power amplifier and measurement circuit.

6.2 Gas Bearings

6.2.1 Journal Bearings

Among the fixed geometry gas bearings which are favored for reasons of production, the herringbone grooved journal bearing and the Rayleigh step journal bearing can be considered for the prototype machine.

With herringbone grooved journal bearings, the herringbone pattern needs to be structured on the rotor to obtain the superior stability [64]. Stability with the pattern on the bushing is worse and furthermore producing the herringbone pattern on the inside surface of the bushing bore seems difficult. Structuring the rotor surface is achieved easier. Typically, the structures are bought on the rotor by precision milling, grinding, or etching [90]. Unfortunately, structuring the rotor with the herringbone micro pattern represents a further step in rotor fabrication. For the prototype, it was preferred to avoid additional production steps after precision grinding of the rotor to micrometer tolerances because of the additional risk it represents.

Fabrication of a Rayleigh step structure can be relatively easy achieved by wire electro discharge machining (EDM) the bearing bushing as the structures occur in axial direction only. Only a few preceding fabrication steps are needed for the bushing before wire EDM, which is the last and the only high precision fabrication step. Thus, a Rayleigh step bearing is chosen for the prototype machine.

The fabricated bearing bushing with the Rayleigh step structure is depicted in Figure 6.5a). The Rayleigh step parameters are based on the optimization given in Section 3.8. The dimensions of the prototype bearing design are listed in Table 6.4. The critical dimensions of the pattern, h_1 and h_2 , were tolerated to deviate $\pm 2 \mu\text{m}$ from their nominal values.

6.2.2 Thrust Bearing

The thrust bearing is implemented as an unstructured disc on the rotor and two herringbone grooved discs on the stator. The herringbone groove pattern is generated by a photo-lithographic procedure using electrochemical etching. In a first step, the unstructured and surface-grounded stator discs are coated with a photoresist. The photoresist is then exposed by means of a 405 nm laser, in a laser direct imaging technique (LDI). After developing the photoresist, the regions of the

Quantity	Symbol	Value
Journal bearing radius	R_j	3 mm
Journal bearing length	l_j	3 mm
Rayleigh step parameter (nom.)	h_1	13 μm
Rayleigh step parameter (nom.)	h_2	8 μm
Rayleigh step parameter (nom.)	h_3	300 μm
Number of steps	N_{step}	8

Table 6.4: Rayleigh step bearing parameters.

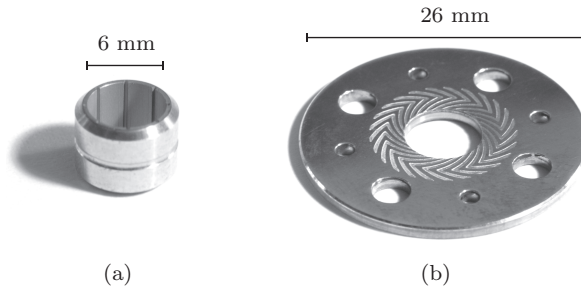


Figure 6.5: Prototypes of the Rayleigh step journal bearing (a) and herringbone grooved thrust disc(b).

pattern to be grooved appear as blank metal. The material at the blank locations is then removed to the desired depth by anodic dissolution in a saturated sodium chloride solution. The structured disc with 15 μm deep herringbone grooves is depicted in Figure 6.5b). The design parameters of the axial bearing are given in Table 6.5.

Parameter	Value
Pattern inner diameter	8 mm
Pattern outer diameter	15 mm
Nominal clearance	15 μm
Groove depth	15 μm
Number of grooves	25

Table 6.5: Herringbone grooved thrust bearing parameters.

6.3 Damper Electronics

The damper electronics containing the eddy current displacement signal processing and angular rotor position detection circuits as well as the damper power amplifiers and a digital signal processor (DSP) for control are implemented on a $80 \times 100 \text{ mm}^2$ 4-layer printed circuit board (PCB). The parallel type eddy current based displacement self-sensing topology is implemented because of its superior performance regarding cross talk of the damper current to the position measurement as discussed in Section 4.3.3. The damper power amplifiers are supplied by a $\pm 8 \text{ V}$ dual supply while the displacement signal processing and the angular position detection circuits are running from a 5 V single supply.

The damper power amplifiers are constructed with Texas instruments OPA548 linear operational amplifiers. A Texas Instruments TMS320F2808 DSP with a 32 bit fixpoint architecture is used to implement the control. The control loop containing signal acquisition with the DSP's internal 12 bit analog-to-digital converter (ADC), the actual control with the displacement derivative, the notch filtering according Chapter 5 and the transformation from the qd reference currents into the phase reference currents is executed at a rate of 83 kHz . The low-pass filter of the displacement signal demodulation stage which defines the measurement bandwidth is implemented as a second order lowpass filter with a cutoff frequency of 35 kHz .

A digital to analog converter interface is connected to the DSP via a serial peripheral interface (SPI) in order to monitor system variables during initial operation and verification measurements. A photograph of the prototype machine with installed dampers and electronics is shown in Figure 6.6.

6.4 Experimental Results

6.4.1 Displacement measurement

Sensitivity

The displacement measurement was calibrated in the assembled system with the installed gas bearings and magnetic damper windings. A Keyence LK-H022 triangulation laser sensor was used as a reference measurement. The rotor was displaced manually and the displacement

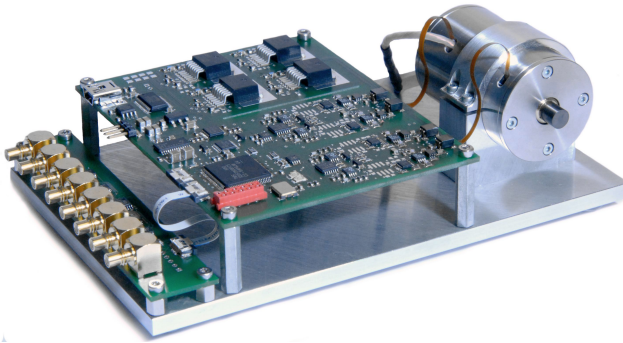


Figure 6.6: Prototype permanent magnet machine with installed gas bearings, AMDs and electronics.

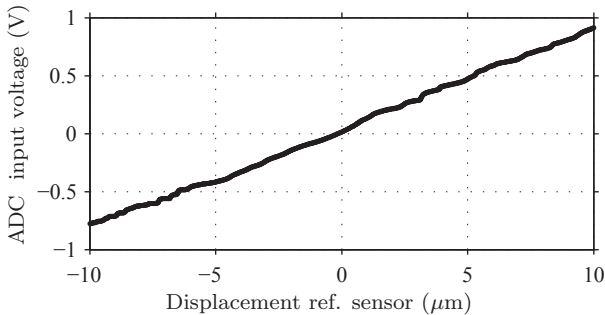


Figure 6.7: Calibration of the eddy current displacement signal captured at the input of the DSPs integrated ADC with a commercial laser triangulation sensor displacement measurement.

signal from the eddy current measurement was recorded against the displacement captured by the laser reference sensor. Figure 6.7 shows the captured displacement signal at the input of the DSPs integrated ADC plotted against the laser reference sensor measurement. For the plot, the signals are made mean free. The measurement shows a sensitivity of $84 \text{ mV}/\mu\text{m}$.

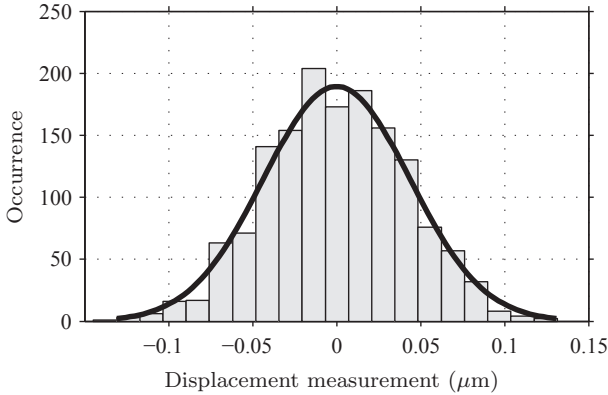


Figure 6.8: Histogram with fitted normal distribution for the rotor displacement measurement with a stationary rotor based on a total of 1500 samples recorded by means of the DSPs internal 12 bit ADC at a sample rate of 83 kHz.

Resolution

Absolute resolution of the eddy current displacement measurement is not needed as only the displacement's derivative will be used for feedback control. Hence drifting of the measurement needs not to be accounted for and is therefore not quantified. The relative resolution is therefore defined by the measurement noise. For the noise measurement, the four displacement signals of the two dampers in both x and y directions are captured by means of the DSPs internal 12 bit ADC at a sample rate of 83 kHz. The rotor is kept stationary. Measurement standard deviations ranging from $\sigma = 44$ nm to $\sigma = 125$ nm were achieved for the four displacement measurements. The deviation of $\sigma = 44$ nm is mainly given by the ADC resolution and corresponds to a digital value of approximately 3.5. Figure 6.8 shows the histogram of 1500 samples for the signal with the lowest noise, i.e. with the standard deviation of $\sigma = 44$ nm. The according Welch estimate of the power spectral density (PSD) is given in Figure 6.9. The noise is mostly evenly distributed over the full captured frequency range with a slight increase towards higher frequencies.

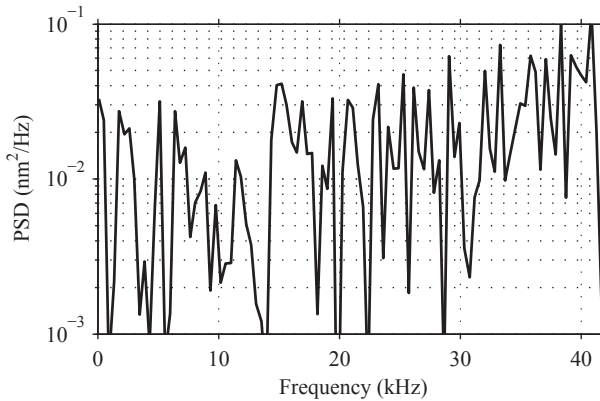


Figure 6.9: Estimate of the power spectral density (Welch’s method) of the rotor displacement measurement signal.

Actuator Current Cross-Talk

In order to quantify the cross-talk of the damper current to the displacement measurement, a damper current is injected into the windings. The amplitude of current is chosen 350 mA rms, which constitutes approximately the maximum continuous current in the winding for thermal reasons. The frequency of the damper current is then swept from zero to 10 kHz and the standard deviation displacement measurement is evaluated for each frequency. For the measurement, a solid steel rod is used in order to exclude actual rotor displacements which with a permanent magnet rotor would be raised by Lorentz forces. The measurement results vary four the total of four implemented measurement channels. In the best case, almost no coupling is observed and the standard deviation of the measurement signal increases to $\sigma = 53$ nm, as depicted in Figure 6.10. In the worst case, a deviation of $\sigma = 150$ nm is obtained. When repeating the same measurement procedure for a current in phase *B*, the increase of noise of the displacement signal in respect to the undisturbed measurement is not measurable.

6.4.2 Stabilization of the Gas Bearings

The machine is operated with a Celeroton CC-75-400 pulse amplitude modulated inverter. When starting the machine, the rotor first slides

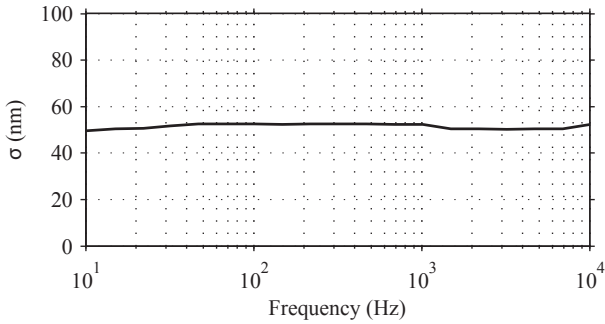


Figure 6.10: Measurement of cross talk from the damper current of in phase A to the displacement measurement in dependency of the damper current frequency.

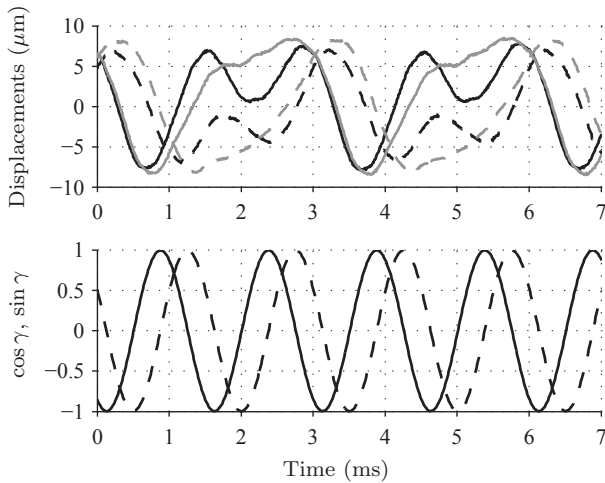


Figure 6.11: Displacement signals measured with the DSP at 40 krpm with inactive damper (top), $\epsilon_{d1,x}$ (solid black), $\epsilon_{d1,y}$ (dashed black), $\epsilon_{d2,x}$ (solid gray), $\epsilon_{d2,y}$ (dashed gray). The gas bearings operate in a whirl condition with a frequency of half of the rotational speed. As a reference, the rotor's angular position in terms of $\cos \gamma$ (solid line) and $\sin \gamma$ (dashed line) is shown (bottom).

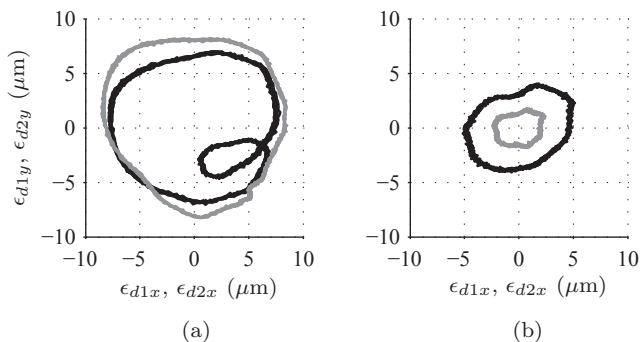


Figure 6.12: Orbit plots of displacements (ϵ_{d1} black, ϵ_{d2} gray) measured by the DSP with inactive damper at 40 krpm (a) and with active magnetic damping at 40 krpm (b).

in the bearing bushings. Lift-off occurs between 5 krpm and 15 krpm. Around 20 krpm the rotor has fully lifted off and is carried stably by the fluid film without the need of active magnetic damping. First unstable behavior is observed already at 30 krpm and it develops to a fully unstable whirl with half of the rotational frequency at 40 krpm. The displacements captured by the DSP along with the cosine and sine of the rotor angle as a reference are shown in Figure 6.11. The corresponding orbit plot is shown in Figure 6.12a).

According to the calculations, the bearings instability onset speed is expected around 100 krpm when assuming worst case production deviations of $\pm 2 \mu\text{m}$. The discrepancy is assumed to be caused by misalignment and/or unbalance which together with the bearings non-linearity, which has not been accounted for in the calculations, may result in destabilization.

By activating the magnetic damper, the gas bearings can be stabilized. Figure 6.12b) shows the orbits measured at 40 krpm with the AMDs being activated. The rotor displacements are now given by the rotor imbalance, as the rotor rotates around its center line of gravity.

A maximum speed of 210 krpm is reached with the current gas bearing design. Figure 6.13 shows the measured displacements together with the damper currents and the angular rotor position signals. Increased noise is visible on the displacement measurement which is caused pri-

marily by the damper currents $i_{a,1}$ respectively $i_{a,2}$.

At 210 krpm, the AMD phase currents range between 170 mA to 180 mA (rms) which leads to calculated winding copper losses of 1.5 W for both AMD windings.

Damping provided for stabilization of the gas bearings was approximately three times higher than what the calculations had predicted. The parameters of the transfer function $d(s)$ had to be set to $K_d = 60$ Ns/m with $p_1 = 12.6 \cdot 10^3$ rad/s to obtain stable operation.

A limiting factor preventing operation at higher speeds is seen in the high controller gain required for stabilization. With the very small but existing cross-talk of the damper current to the displacement measurement, a maximum achievable controller gain is imposed. With higher gains, the existence of cross-talk would render the electrical system unstable. In order to reach higher rotational speeds with the present magnetic damper design, a gas bearing with better stability requiring less magnetic damping would be needed.

6.4.3 Deceleration Test

A deceleration test is performed in order to determine the losses of the prototype machine. In the experiment, the rotor is spun up to the maximum stably operating speed of 200 krpm, where the machine inverter is stopped and its outputs are set to a high impedance state. Hence no currents are injected into the phases and no torque is produced by the machine's motor winding. The only torque acting on the rotor is then the braking torque resulting from the sum of the losses which decelerate the rotor. The braking torque can be determined by means of the recorded speed Ω over the time t as

$$T_{br} = -I_{z0} \frac{d\Omega}{dt}, \quad (6.6)$$

where I_{z0} is the inertia of the rotor about its principal axis of rotation. The according losses are

$$P_{br} = T_{br} \cdot \Omega \quad (6.7)$$

For the measurement, the speed is extracted from the angular rotor position signals which are recorded over time. The results of the run-down test are given in Figure 6.14. At low speeds, a friction torque is observed which results from the gas bearing's dry friction before lift-off at around 20 krpm. The friction torque has its minimum around lift-off

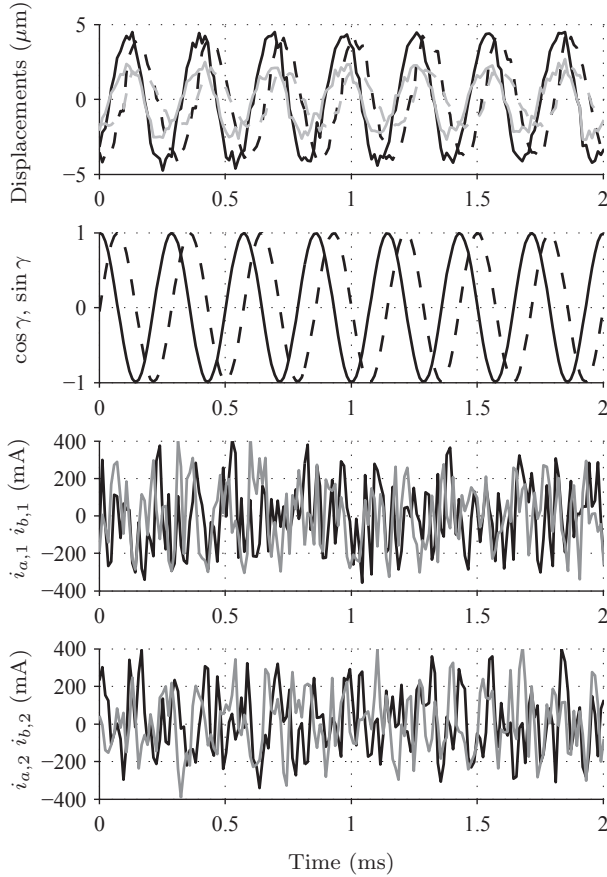


Figure 6.13: Measurement of the rotor displacements $\epsilon_{d1,x}$ (solid black), $\epsilon_{d1,y}$ (dashed black), $\epsilon_{d2,x}$ (solid gray), $\epsilon_{d2,y}$ (dashed gray) at 210 krpm along with the rotor position signals $\cos \gamma$ (solid line) and $\sin \gamma$ (dashed line) and the damper winding currents $i_{a,1}$ (black line), $i_{b,1}$ (gray line) and $i_{a,3}$ (black line), $i_{b,3}$ (gray line).

and increases again towards higher speeds. A total of 5.5 W of losses is obtained at 200 krpm. The calculated contributions from the machine's iron losses, copper proximity losses and air friction losses yield

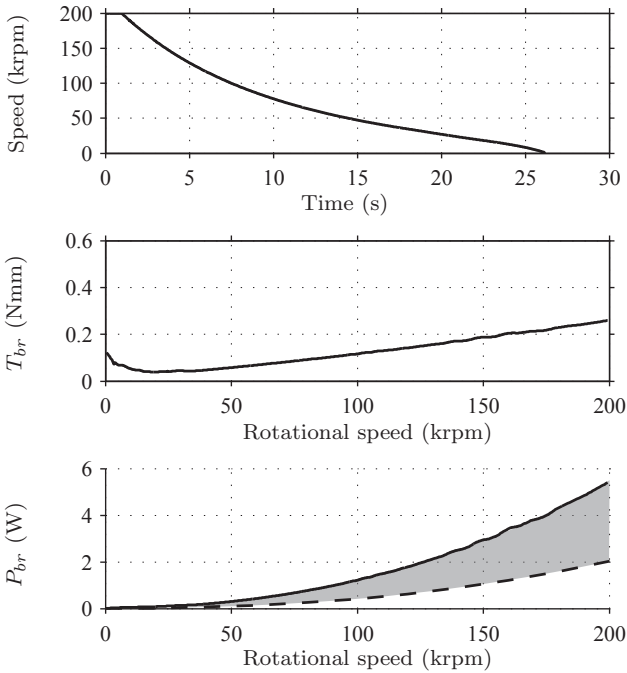


Figure 6.14: Rundown test of the prototype machine from 200 krpm. Speed recorded over time (top), speed dependent braking torque T_{br} (middle) and resulting losses P_{br} (solid line, bottom) with the calculated no load machine losses (dashed line, bottom). The shaded gray area represents the gas bearing losses.

a total of 2.0 W. Hence the difference can be attributed to the journal bearings and the thrust bearing. The losses of the journal bearings are calculated as twice 0.8 W, leaving 1.9 W for the thrust bearing.

Figure 6.15 shows a spectrogram of the displacement $\epsilon_{d1,x}$ recorded during rundown. The fundamental frequency resulting from rotor imbalance represents the dominant displacement, visible as the straight black line. Harmonics of the fundamental frequency are also present which may originate from rotor surface out-of-roundness. At around 20 krpm, an onset of half speed whirling is visible which however disappears again towards higher speeds.

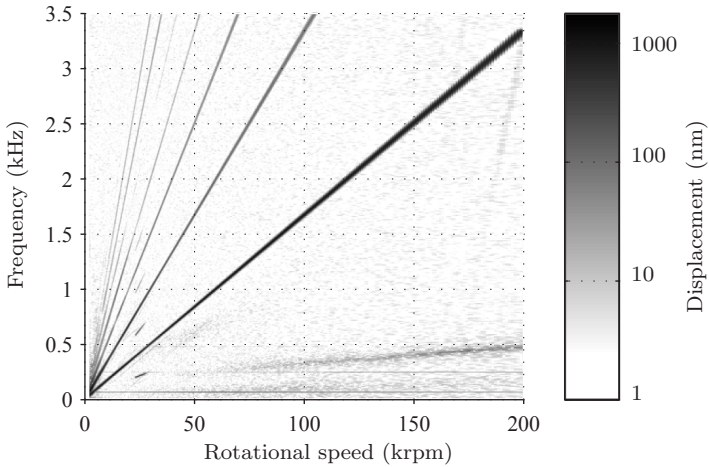


Figure 6.15: Spectrogram of the displacement $\epsilon_{d1,x}$ recorded during rundown.

Comparing with the Campbell diagram of Figure 5.6 one may identify the bearing dynamics at frequencies below 500 Hz. Towards higher speeds, there is a slight increase of displacement visible in the frequency range of the bearing dynamics. Thus, a higher amount of damping would be required in order to suppress these vibrations, especially when proceeding towards higher rotational speeds.

Chapter 7

Conclusion

7.1 Summary

Industrial application of ultra-high-speed electrical drive system has been limited mainly due to the absence of a reliable bearing technology with long lifetime at rotational speeds ranging from a 200 krpm up to 1 Mrpm. Potential applications are turbo-compressors for heat pumps, fuel cells, generators for portable gas or air turbines and cryogenic systems which due to the high rotational speed can be realized with high power density, compact size and low weight.

Possible bearing candidates have been identified as active magnetic bearings (AMBs) and gas bearings due to their contact-less working principle avoiding friction and wear. Gas bearings can be realized of compact size, high load capacity and stiffness, but suffer from poor dynamic stability and stringent manufacturing tolerances at high rotational speeds. In contrast, AMBs have no inherent stability limitation as stability is raised by the active feedback control. However the main disadvantage is its major installation size and an increased system complexity coming with actuators, sensors, power amplifiers, control and the need of an emergency touchdown bearing system.

The objective of this thesis has therefore been the evaluation, analysis, conceptual development and experimental testing of a hybrid gas-magnetic bearing system aiming to combine the advantages of the individual bearing technologies while eliminating or minimizing their limitations and drawbacks. The hybrid gas-magnetic bearing concept intends

to employ a gas bearing as the main load carrying element, which is stabilized by means of a small sized active magnetic damper (AMD) at high rotational speeds.

Thus, in a first step, the general properties of gas bearings have been reviewed and with a focus on ultra-high-speed operation, the bearing minimum film clearance has been identified as the most critical design parameter. It has been shown, that for dynamic stability at high speeds, the bearing's clearance will need to be chosen stringently small, which however is conflicting with fabrication and assembly tolerances and the bearing's ability to cope with centrifugal and thermal rotor growth. Furthermore, due to the small bearing clearance, viscous friction losses will become considerable. By allowing a more generous bearing clearance, the fabrication and structural issues as well as the high friction losses can be relaxed. In this case, it has been shown, that dynamic stability can be achieved by providing damping by an external source, e.g. by means of an AMD.

For use at high rotational speeds, a slotless AMD is identified as the preferred type of actuator. In order to obtain a small installation size and reduced system complexity, a self-sensing damper concept is approached. Based on electrical winding models, back-EMF based self-sensing damper strategies have been studied for both homopolar and heteropolar damper implementations. While the back-EMF based damper concepts are shown to have their limitations in terms of achievable gain and bandwidth due to modeling uncertainty, a new eddy current based self-sensing heteropolar AMD concept has been proposed, allowing for a highly compact integration into a permanent magnet machine with minimal additional design constraints. For test signal injection and extraction at a frequency of more than 10 MHz, novel auxiliary circuit topologies have been presented enabling a high resolution eddy current based self-sensing displacement measurement.

Based on a rigid rotor model, the possibility of stabilization by means of a simple D-controller has been shown. A prototype implementation of a permanent magnet machine employing the proposed hybrid gas-magnetic bearing concept has been presented and stable operation up to a speed of 210 krpm has been demonstrated. The experimental results verify the feasibility of the hybrid bearing approach and demonstrate the capability of the proposed self-sensing AMD concept to facilitate operation of gas bearings at elevated rotational speeds.

7.2 Outlook

In order to achieve higher speeds with the presented prototype machine, improvements regarding the gas bearing performance will be needed. Probably in a more practical approach, the optimum between fabrication effort and bearing performance needs to be identified, given the new possibility of active magnetic stabilization. Also, more advanced control schemes than the employed D-controller need to be investigated, which may yield superior performance. While stable operation of a hybrid gas-magnetic bearing has been shown in a prototype demonstrator system without the load of a typical application, a next steps should be the implementation of the hybrid bearing in an industrial application such as a turbocompressor for heat pumps or fuel cells.

A next research vector could point in the area of high speed self-sensing AMB systems, applying the proposed concept of eddy current based displacement self-sensing. Naturally, the AMB winding will have to be designed considerably larger than for the presented AMD design as the full load must be provided by the AMB. Still, by avoiding the need of dedicated sensors, more compact realizations can be expected than with a standard, sensor based approach.

Bibliography

- [1] C. Zwyssig, “An ultra-high-speed electrical drive system,” Ph.D. dissertation, ETH Zurich, 2008.
- [2] D. Krahenbuhl, “Bidirectional interfacing of compressed-air and electric power employing ultra-high-speed drives and turbomachinery,” Ph.D. dissertation, ETH Zurich, 2010.
- [3] A. Borisavljevic, “Limits, modeling and design of high-speed permanent magnet machines,” Ph.D. dissertation, Technical University Delft, Netherlands, 2011. **PDF**
- [4] P.-D. Pfister and Y. Perriard, “Very-high-speed slotless permanent-magnet motors: Analytical modeling, optimization, design, and torque measurement methods,” *IEEE Transactions on Industrial Electronics*, vol. 57, no. 1, pp. 296–303, Jan. 2010. **PDF**
- [5] M. Kimman, “Design of a micro milling setup with an active magnetic bearing spindle,” Ph.D. dissertation, Technical University Delft, 2010. **PDF**
- [6] T. Baumgartner, “A magnetically-levitated 500000 rpm electrical drive system,” Ph.D. dissertation, ETH Zürich, 2013.
- [7] B. Blunier and A. Miraoui, “Proton exchange membrane fuel cell air management in automotive applications,” *ASME Journal of Fuel Cell Science and Technology*, vol. 7, 2010. **PDF**
- [8] D. Zhao, D. Krahenbuhl, B. Blunier, C. Zwyssig, M. Dou, and A. Miraoui, “Design and control of an ultra high speed turbo compressor for the air management of fuel cell systems,” in *IEEE*

Transportation Electrification Conference and Expo (ITEC), 2012.

PDF

- [9] J. Schiffmann and D. Favrat, “Design, experimental investigation and multi-objective optimization of a small-scale radial compressor for heat pump applications,” *Energy*, vol. 35, no. 1, pp. 436 – 450, 2010. **PDF**
- [10] —, “Experimental investigation of a direct driven radial compressor for domestic heat pumps,” *International Journal of Refrigeration*, vol. 32, no. 8, pp. 1918 – 1928, 2009. **PDF**
- [11] D. Antonijevic and R. Heckt, “Heat pump supplemental heating system for motor vehicles,” *Proceedings of the Institution of Mechanical Engineers, Part D: Journal of Automobile Engineering*, vol. 208, 2008. **PDF**
- [12] H. Zhebin, L. Jing, Y. Dazhang, and H. Xiuzhi, “Research of the co2 heat pump system for automotive air conditioning,” in *International Conference on Energy and Environment Technology*, vol. 1, 2009, pp. 275–278. **PDF**
- [13] D. Krahenbuhl, C. Zwysig, H. Weser, and J. W. Kolar, “A miniature 500000 r/min electrically driven turbocompressor,” *IEEE Transactions on Industry Applications*, vol. 46, no. 6, pp. 2459–2466, 2010. **PDF**
- [14] L. Zhao, C. Ham, L. Zheng, T. Wu, K. Sundaram, J. Kapat, and L. Chow, “A highly efficient 200000 rpm permanent magnet motor system,” *IEEE Transactions on Magnetics*, vol. 43, no. 6, pp. 2528–2530, 2007. **PDF**
- [15] J. Oyama, T. Higuchi, T. Abe, K. Shigematsu, and R. Moriguchi, “The development of small size ultra-high speed drive system,” in *Proceedings of the IEEE Power Conversion Conference (PCC 2007)*, 2007, pp. 1571–1576. **PDF**
- [16] Celeroton AG. Zurich, Switzerland. <http://www.celeroton.com>.
- [17] Calnetix Technologies LCC. Cerritos CA, USA. <http://www.calnetix.com>.
- [18] F. Betschon, “Design principles of integrated magnetic bearings,” Ph.D. dissertation, ETH Zurich, 2000. **PDF**

-
- [19] P. Imoberdorf, “Ultrakompakter Antrieb mit radial und axial kombiniertem Magnetlager,” Ph.D. dissertation, ETH Zurich, 2011. **PDF**
- [20] S. Silber, J. Sloupensky, P. Dirnberger, M. Moravec, M. Reisinger, and W. Amrhein, “High speed drive for textile rotor spinning applications,” *IEEE Transactions on Industrial Electronics*, vol. PP, no. 99, 2013. **PDF**
- [21] G. Schweitzer and E. Maslen, *Magnetic bearings - theory, design, and application to rotating machinery*. Springer, 2009. **PDF**
- [22] H. Mitterhofer and W. Amrhein, “Design aspects and test results of a high speed bearingless drive,” in *IEEE Ninth International Conference on Power Electronics and Drive Systems (PEDS 2011)*, 2011, pp. 705–710. **PDF**
- [23] M. Salehi, H. Heshmat, J. F. Walton, and M. Tomaszewski, “Operation of a mesoscopic gas turbine simulator at speeds in excess of 700,000 rpm on foil bearings,” *ASME Journal of Engineering for Gas Turbines and Power*, vol. 129, no. 1, pp. 170–176, 2007. **PDF**
- [24] D. Kim, M. S. Hossain, S.-J. Son, C.-J. Choi, and D. Krähenbühl, “Five millimeter air foil bearing operating at 350,000 rpm in a micro electric motor drive,” in *Proceedings of the ASME/STLE International Joint Tribology Conference (IJTC2011)*, 2011, pp. 163–166. **PDF**
- [25] S. Tanaka, M. Esashi, K. Isomura, K. Hikichi, Y. Endo, and S. Togo, “Hydroinertia gas bearing system to achieve 470 m/s tip speed of 10 mm-diameter impellers,” *ASME Journal of Tribology*, vol. 129, pp. 655–659, 2007. **PDF**
- [26] S. Togo, “Comparative studies of the performance of high-speed gas bearings for micro-turbo machines,” Tohoku-Gakuin University, Japan, Tech. Rep., 2006. **PDF**
- [27] T. Ise, S. Onoe, T. Asami, I. Kawashima, and T. Maeda, “Split-type herringbone-grooved hydrodynamic journal gas bearings for small ultra-high-speed rotary machines,” *JSME Journal of Power and Energy Systems*, vol. 5, pp. 406 – 413, 2011. **PDF**

- [28] T. Waumans, J. Peirs, F. Al-Bender, and D. Reynaerts, "Aerodynamic journal bearing with a flexible, damped support operating at 7.2 million dn," *Journal of Micromechanics and Microengineering*, vol. 21, 2011. **PDF**
- [29] J. Peirs, C. Zwysig, T. Waumans, F. Al-Bender, and D. Reynaerts, "600 000 rpm electrical motor/generator supported by air bearings," in *Proceedings of the 12th International Workshop on Micro and Nanotechnology for Power Generation and Energy Conversion Applications (PowerMEMS2012)*, Dec. 2012, pp. 165–168. **PDF**
- [30] K. Hikichi, S. Goto, S. Togo, S. Tanaka, and K. Isomura, "Hydroinertia gas bearings for micro spinners," *Journal of Micromechanics and Microengineering*, vol. 15, 2005. **PDF**
- [31] J. Beams, "High rotational speeds," *Journal of Applied Physics*, vol. 8, pp. 795 – 806, 1937. **PDF**
- [32] C. J. Teo, L. X. Liu, H. Q. Li, L. C. Ho, S. A. Jacobson, F. F. Ehrich, A. H. Epstein, and Z. S. Spakovszky, "High-speed operation of a gas-bearing supported mems-air turbine," *ASME Journal of Tribology*, vol. 131, 2009. **PDF**
- [33] Westwind Air Bearings. Poole, UK. <http://www.westwind-airbearings.com>.
- [34] M. J. Neale, "Selection of bearings," in *Proceedings of the Institution of Mechanical Engineers*, vol. 182, no. 1, September 1967, pp. 547–556. **PDF**
- [35] M. M. Khonsari and E. R. Booser, *Applied Tribology: Bearing Design and Lubrication, Second Edition*. John Wiley & Sons, Ltd., 2008. **PDF**
- [36] H. Signer, E. N. Bamberger, and E. V. Zaretsky, "Long life, high speed, thrust-load ball bearings," Glenn Research Center, Tech. Rep., 1975. **PDF**
- [37] E. Bamberger, *Life Adjustment Factors fo Ball and Roller Bearings - An Engineering Design Guide*. ASME, New York, 1971.
- [38] W. Changsen, *Analysis of Rolling Element Bearings*. Mechanical Engineering Publications Limited, 1991.

-
- [39] H. Bleuler, “A survey of magnetic levitation and magnetic bearing types,” *JSME International Journal of Vibration*, no. 3, pp. 335–342, September 1992. [PDF](#)
- [40] T. Baumgartner, A. Looser, C. Zwysig, and J. W. Kolar, “Novel high-speed, Lorentz-type, slotless self-bearing motor,” in *Proceedings of the IEEE Energy Conversion Congress and Exposition (ECCE 2010)*, 2010, pp. 3971–3977. [PDF](#)
- [41] D. Steinert, T. Nussbaumer, and J. W. Kolar, “Concept of a 150 krpm bearingless slotless disc drive with combined windings,” in *Proceedings of the IEEE International Electric Machines and Drives Conference (IEMDC 2013), Chicago, USA*, May 2013. [PDF](#)
- [42] H. Marsh, “The stability of aerodynamic gas bearings,” *Mechanical Engineering Science*, vol. 2, Monograph, June 1965.
- [43] Fuller, “A review of research in the field of gas-lubricated bearings,” Franklin Inst. Research Labs, Philadelphia, PA, Tech. Rep., 1970. [PDF](#)
- [44] A. Chiba, T. Fukao, O. Ichikawa, M. Oshima, M. Takemoto, and D. G. Dorrell, *Magnetic bearings and bearingless drives*. Newnes, 2005. [PDF](#)
- [45] B. Hamrock, S. Schmid, and B. Jacobson, *Fundamentals of Fluid Film Lubrication*, ser. Mechanical Engineering. Marcel Dekker, 2004. [PDF](#)
- [46] H. Elrod and A. Burgdorfer, “Refinements on the theory of the infinitely-long, self-acting, gas-lubricated journal bearing,” Franklin Inst. Research Labs, Philadelphia, PA, Tech. Rep., 1960. [PDF](#)
- [47] B. Hamrock, “Rayleigh step journal bearing part 1 – compressible fluid,” *ASME Journal of Tribology*, vol. 90, pp. 271 – 280, 1968. [PDF](#)
- [48] J. Ausman, “Theory and design of self-acting gas-lubricated journal bearings including misalignemnt effects,” *International Symposium on Gas Lubricated Bearings*, pp. 161–192, 1959. [PDF](#)

- [49] B. Hamrock and D. Flemming, "Optimization of self-acting herringbone journal bearings for maximum radial load capacity," Franklin Inst. Research Labs, Philadelphia, PA, Tech. Rep., 1971. [PDF](#)
- [50] D. Flemming and B. Hamrock, "Optimization of self-acting herringbone journal bearings for maximum stability," *6th International Gas Bearing Symposium*, March 1974. [PDF](#)
- [51] T. Waumans, J. Peirs, D. Reynaerts, and F. Al-Bender, "On the dynamic of high-speed gas bearings: stability study and experimental validation," in *Proceedings of the 3rd Conference on Sustainable Construction and Design*, February 2011, pp. 342–351. [PDF](#)
- [52] W. Beitz and K.-H. Küttner, *Handbook of Mechanical Engineering*. Springer, 1994.
- [53] R. B. Hetnarski and M. R. Eslami, *Thermal Stresses – Advanced Theory and Applications*. Springer, 2009.
- [54] M. T. C. Faria and L. S. Andrés, "On the numerical modeling of high-speed hydrodynamic gas bearings," *ASME Journal of Tribology*, vol. 122, no. 1, pp. 124–130, 2000. [PDF](#)
- [55] R. van der Stegen, "Numerical modeling of self-acting gas lubricated bearings with experimental verification," Ph.D. dissertation, The University of Twente, Netherlands, 1997. [PDF](#)
- [56] T. Kobayashi, "Numerical analysis of herringbone-grooved gas-lubricated journal bearings using a multigrid technique," *ASME Journal of Tribology*, vol. 121, no. 1, pp. 148–156, January 1999. [PDF](#)
- [57] P. Yang, K.-Q. Zhu, and X.-L. Wang, "On the non-linear stability of self-acting gas journal bearings," *Tribology International*, vol. 42, no. 1, pp. 71 – 76, 2009. [PDF](#)
- [58] G. Shen, Z. Xiao, W. Zhang, and T. Zheng, "Nonlinear behavior analysis of a rotor supported on fluid-film bearings," *ASME Journal of Vibration and Acoustics*, vol. 128, no. 1, pp. 35–40, February 2006. [PDF](#)

-
- [59] H. G. J. Elrod, H., J. T. McCabe, and T. Y. Chu, "Determination of gas bearing stability by response to a step-jump," Franklin Inst. Research Labs, Philadelphia, PA, Tech. Rep., 1966. **PDF**
- [60] B. Miller and I. Green, "Constitutive equations and the correspondence principle for the dynamics of gas lubricated triboelements," *ASME Journal of Tribology*, vol. 120, pp. 345–352, April 1998. **PDF**
- [61] —, "On the stability of gas lubricated triboelements using the step jump method," *ASME Journal of Tribology*, vol. 119, pp. 193–199, 1997. **PDF**
- [62] C. H. T. Pan, "Spectral analysis of gas bearing systems for stability studies," Mechanical Technology Inc. Latham, NY, Tech. Rep., 1964. **PDF**
- [63] V. N. Constantinescu, "On hydrodynamic instability of gas lubricated journal bearings," *ASME Journal of Basic Engineering*, vol. 87, pp. 579–588, 1965.
- [64] J. Vohr and C. Chow, "Characteristics of bearings of herringbone-grooved gas-lubricated journal bearings," *ASME Journal of Basic Engineering*, vol. 87, pp. 568–578, 1965.
- [65] M. A. Hassini and M. Arghir, "A simplified nonlinear transient analysis method for gas bearings," *ASME Journal of Tribology*, vol. 134, 2012. **PDF**
- [66] J. Schiffman and Z. Spakovszky, "Foil bearing design guidelines for improved stability," *ASME Journal of Tribology*, vol. 113, 2012. **PDF**
- [67] L. Ljung, *System Identification: Theory for the User*. Upper Saddle River, NJ, USA: Prentice-Hall PTR, 1999. **PDF**
- [68] A. Varga, "Balancing free square-root algorithm for computing singular perturbation approximations," in *Proceedings of the 30th IEEE Conference on Decision and Control*, vol. 2, 1991, pp. 1062–1065. **PDF**
- [69] J. Qiu, J. Tani, and T. Kwon, "Control of self-excited vibration of a rotor system with active gas bearings," *ASME Journal of Vibration and Acoustics*, vol. 125, pp. 328–334, 2003. **PDF**

- [70] A. El-Shafei and A. S. Dimitri, “Controlling journal bearing instability using active magnetic bearings,” *ASME Journal of Engineering for Gas Turbines and Power*, vol. 132, 2010. [PDF](#)
- [71] M. N. Sahinkaya and C. R. Burrows, “Stabilisation of high-speed flexible rotors supported by oil-film bearings,” in *Sixth International Conference on Rotor Dynamics*, 2002. [PDF](#)
- [72] —, “Control of stability and the synchronous vibration of a flexible rotor supported on oil-film bearings,” *ASME Journal of Dynamic Systems, Measurement and Control*, vol. 107, pp. 139–144, 1985. [PDF](#)
- [73] H. Heshmat, H. M. Chen, and J. F. Walton, “On the performance of hybrid foil-magnetic bearings,” *ASME Journal of Engineering for Gas Turbines and Power*, vol. 122, pp. 73 – 82, 2000.
- [74] J. Luomi, C. Zwysig, A. Looser, and J. W. Kolar, “Efficiency optimization of a 100-w 500 000-r/min permanent-magnet machine including air-friction losses,” *IEEE Transactions on Industry Applications*, vol. 45, no. 4, pp. 1368–1377, 2009. [PDF](#)
- [75] K. Atallah, Z. Q. Zhu, and D. Howe, “Armature reaction field and winding inductances of slotless permanent-magnet brushless machines,” *IEEE Transactions on Magnetics*, vol. 34, no. 5, pp. 3737–3744, 1998. [PDF](#)
- [76] Z. Ren and L. Stephens, “Force characteristics and gain determination for a slotless self-bearing motor,” *IEEE Transactions on Magnetics*, vol. 42, no. 7, pp. 1849–1860, 2006. [PDF](#)
- [77] T. Baumgartner, R. Burkart, and J. W. Kolar, “Analysis and design of an ultra-high-speed slotless self-bearing permanent-magnet motor,” in *Proceedings of the 38th Annual Conference on IEEE Industrial Electronics Society (IECON 2012)*, 2012, pp. 4477–4483. [PDF](#)
- [78] J. Boehm, R. Gerber, and N. R. C. Kiley, “Sensors for magnetic bearings,” *IEEE Transactions on Magnetics*, vol. 29, no. 6, pp. 2962–2964, 1993. [PDF](#)
- [79] R. Larsonneur and P. Buehler, “New radial sensor for active magnetic bearings,” in *Proceedings of the 9th International Symposium on Magnetic Bearings*, 2004. [PDF](#)

- [80] A. Muesing, C. Zingerli, and J. W. Kolar, “PEEC-based numerical optimization of compact radial position sensors for active magnetic bearings,” in *Proceedings of the 5th International Conference on Integrated Power Electronics Systems (CIPS 2008)*, 2008. **PDF**
- [81] G. Genta, *Dynamics of rotating systems*. Springer Science, 2005. **PDF**
- [82] C. Paulitsch, P. Gardonio, and S. J. Elliott, “Active vibration damping using self-sensing, electrodynamic actuators,” *Smart Materials and Structures*, vol. 15, pp. 499 – 508, 2006. **PDF**
- [83] N. Amati, X. D. Lépine, and A. Tonoli, “Modeling of electrodynamic bearings,” *ASME Journal of Vibration and Acoustics*, vol. 1130, 2008. **PDF**
- [84] A. Schammas, R. Herzog, P. Buehler, and H. Bleuler, “New results for self-sensing active magnetic bearings using modulation approach,” *IEEE Transactions on Control Systems Technology*, vol. 13, no. 4, pp. 509 – 516, July 2005. **PDF**
- [85] T. Kuwajima, T. Nobe, K. Ebara, A. Chiba, and T. Fukao, “An estimation of the rotor displacements of bearingless motors based on a high frequency equivalent circuits,” in *Proceedings of the 4th IEEE International Conference on Power Electronics and Drive Systems*, 2001, pp. 725–731. **PDF**
- [86] M. Nabavi and S. Nihtianov, “Design strategies for eddy-current displacement sensor systems: Review and recommendations,” *IEEE Sensors Journal*, vol. 12, no. 12, pp. 3346–3355, 2012. **PDF**
- [87] A. Looser, T. Baumgartner, J. W. Kolar, and C. Zwyssig, “Analysis and measurement of three-dimensional torque and forces for slotless permanent-magnet motors,” *IEEE Transactions on Industry Applications*, vol. 48, no. 4, pp. 1258–1266, 2012. **PDF**
- [88] J. A. Ferreira, *Electromagnetic modeling of power electronic converters*. Norwell, USA: Kluwer Academic Publishers, 1989.
- [89] M. Mack, “Luftreibungsverluste bei elektrischen Maschinen kleiner Baugröße,” Ph.D. dissertation, Universität Stuttgart, Stuttgart, Germany, 1967.

- [90] N. Grassam and J. Powell, *Gas lubricated bearings*. Butterworths, 1964.

Curriculum Vitæ

Name	Andreas Looser
Birth	29 th March 1981
Place of birth	Wattwil, SG (Switzerland)
Citizen of	Switzerland
Education	1989 – 1994 Primarschule, Waltalingen ZH 1994 – 2001 Kantonschule Rychenberg, Wintherthur ZH Matura Typus B
University	2001 – 2007 ETH Zürich M.Sc. in Electrical Engineering
Doctorate	2008 – present Doctorate at the Power Electronics Systems Laboratory (PES), ETH Zurich